



UPPSALA
UNIVERSITET

*Digital Comprehensive Summaries of Uppsala Dissertations
from the Faculty of Science and Technology 2208*

Chemical vapor deposition of hard coatings

Development of W(C,N) coatings for cemented carbide and TiN deposition on a CoCrFeNi substrate

KATALIN BÖÖR



ACTA
UNIVERSITATIS
UPSALIENSIS
UPPSALA
2022

ISSN 1651-6214
ISBN 978-91-513-1640-6
URN urn:nbn:se:uu:diva-487198

Dissertation presented at Uppsala University to be publicly examined in Polhemsalen, Ångströmlaboratoriet, Lägerhyddsvägen 1, Uppsala, Friday, 16 December 2022 at 09:15 for the degree of Doctor of Philosophy. The examination will be conducted in English. Faculty examiner: Professor Markku Leskelä (Department of Chemistry, University of Helsinki, Finland).

Abstract

Böör, K. 2022. Chemical vapor deposition of hard coatings. Development of W(C,N) coatings for cemented carbide and TiN deposition on a CoCrFeNi substrate. *Digital Comprehensive Summaries of Uppsala Dissertations from the Faculty of Science and Technology* 2208. 93 pp. Uppsala: Acta Universitatis Upsaliensis. ISBN 978-91-513-1640-6.

There is a constant need for cutting tool material development to be able to machine new materials and improve the metal cutting efficiency. Inserts of indexable cutting tools usually consist of WC-Co cemented carbide (cc) with μm thick layers of ceramic coatings. Chemical vapor deposition (CVD) is a commonly used method for the synthesis of such coatings and this technique was also used in this thesis.

The first part of the thesis focuses on a CoCrFeNi substrate, a multi-component alloy previously suggested as an alternative binder phase instead of Co in cc. Titanium nitride (TiN) is typically the first CVD coating layer on cc and therefore the chemical stability of CoCrFeNi in CVD of TiN using TiCl_4 , N_2 and H_2 precursors at 850–950 °C was studied. CoCrFeNi was stable in the CVD processes although small amounts of Cr were detected in the grain boundaries and on the top surface of the TiN coating deposited at 950 °C. Thermodynamic calculations were used to explain the experimental observations.

In the second part of the thesis W(C,N) coatings were developed by CVD. The motivations behind the CVD of W(C,N) coatings were an expected compressive stress due to a favorable match between the thermal behavior of the coating and that of the cc substrate, and a high coating toughness due to the expected strong metallic character of the coating.

A CVD process window was determined for the deposition of columnar hexagonal W(C,N) coatings at a low total pressure as a function of the WF_6 , CH_3CN and H_2 precursor partial pressures and the deposition temperature. Electron microscopy, diffraction techniques, spectroscopic methods and ion beam analyses were used to characterize the coatings. Correlations between the microstructure, texture and process parameters were found.

The mechanical and tribological performances of the W(C,N) coatings were also investigated. The coatings had a high nanohardness of about 40 GPa and showed indications of a high toughness. The abrasive wear mechanism was primarily micro cutting or plowing. The coatings had good adhesion to the cc substrate.

Katalin Böör, Department of Chemistry - Ångström, Inorganic Chemistry, Box 538, Uppsala University, SE-751 21 Uppsala, Sweden.

© Katalin Böör 2022

ISSN 1651-6214

ISBN 978-91-513-1640-6

URN urn:nbn:se:uu:diva-487198 (<http://urn.kb.se/resolve?urn=urn:nbn:se:uu:diva-487198>)

List of papers

This thesis is based on the following papers, which are referred to in the text by their Roman numerals.

- I Böör, K., Qiu, R., Forslund, A., Bäcke, O., Larsson, H., Lindahl, E., Halvarsson, M., Boman, M., von Fieandt, L., Chemical vapor deposition of TiN on a CoCrFeNi multi-principal element alloy substrate, *Surface & Coatings Technology* 393 (2020), 125778
- II Böör, K., Lindahl, E., von Fieandt, L., Boman, M., On the growth kinetics, texture, microstructure and mechanical properties of tungsten carbonitride deposited by chemical vapor deposition, *Journal of Vacuum Science & Technology A*, 40 (2022), 053101
- III Böör, K., Bäcke, O., von Fieandt, L., Boman, M., Halvarsson, M., Microstructural investigation of chemical vapor deposited W(C,N) coatings by electron microscopy, *In manuscript*
- IV Böör, K., von Fieandt, L., Boman, M., Fallqvist, M., Tribological and mechanical properties of chemical vapor deposited W(C,N) coatings on cemented carbide substrates, *In manuscript*

Reprints were made with permission from the publishers. The papers published in Elsevier journals were reproduced following the policy for authors to use and share their works for scholarly purposes. Paper II was reproduced with written permission of AVS: Science & Technology of Materials, Interfaces, and Processing.

My contributions to the papers

- I I planned the characterization of the samples and carried the substrate synthesis, the XRD and SEM characterization. I wrote the major part of the manuscript.
- II I planned the study and carried out all the syntheses and characterization except for the ERDA measurements. I wrote the manuscript with input from the supervisors.
- III I planned the study, synthesized the coatings, I participated in part of the TEM sessions and carried out all other characterization. I performed the data analysis and wrote the manuscript with input from the co-authors and supervisors.
- IV I planned the study together with the co-authors, synthesized the coatings and carried out all the mechanical and tribological tests, the tribological tests under guidance of the co-authors. I performed all the SEM and XRD characterization and the data analysis. I wrote the manuscript with input from the co-authors and supervisors.

Other publications

The author has contributed to the following publications that are not included in this thesis:

- I G. Hulkko, J., Böör, K., Qiu, R., Bäcke, O., Boman, M., Halvarsson, M., Lindahl, E., Kinetics of the low-pressure chemical vapor deposited tungsten nitride process using tungsten hexafluoride and ammonia precursors, *Journal of Vacuum Science & Technology A*, 39 (2021), 063403
- II G. Hulkko, J., Fallqvist, M., Böör, K., von Fieandt, L., Larsson, T., Boman, M., Tribological and mechanical characteristics of LPCVD-TiWN, *Submitted*

Contents

1	Introduction	13
2	Synthesis method and materials	15
2.1	Chemical vapor deposition	15
2.1.1	Key aspects of chemical vapor deposition	15
2.1.2	Reactors used in this thesis	16
2.1.3	Reaction kinetics in chemical vapor deposition	17
2.2	Materials	18
2.2.1	CoCrFeNi and the CVD process for TiN deposition	18
2.2.2	Optimization of the mechanical properties — from Ti-based to W-based ceramic coatings	20
2.2.3	Mechanical properties of W-based ceramic coatings	22
2.2.4	W(C,N) — a material similar to the cemented carbide substrate	23
2.2.5	Deposition of W(C,N) coatings	23
3	Characterization methods	25
3.1	X-ray diffraction	25
3.2	Scanning electron microscopy	27
3.3	Electron backscatter diffraction	28
3.4	Transmission electron microscopy	28
3.5	Ion beam analysis techniques	29
3.6	X-ray photoelectron spectroscopy	30
3.7	Nanoindentation	31
3.8	Scratch tests	33
3.9	Abrasive wear tests	33
3.10	Calculation of phase diagrams	34
4	Scope of the thesis	35
5	Results and Discussion	36
5.1	TiN deposition on a CoCrFeNi substrate	36
5.2	CVD of W(C,N): The process window	39
5.3	Kinetics of W(C,N) deposition and the current understanding of the reaction mechanism	46
5.4	The growth, microstructure and texture of W(C,N)	48
5.4.1	Columnar growth with a ridge-like top surface	48

5.4.2	Microstructure and texture variations related to the process parameters	50
5.4.3	Microstructure and texture — a comparison with other ceramic coatings	57
5.5	Elemental composition and spectroscopy of W(C,N)	58
5.6	Mechanical and tribological properties of W(C,N)	62
5.6.1	Hardness, elastic modulus and residual stress	63
5.6.2	Toughness	64
5.6.3	Abrasive wear resistance	67
5.6.4	Adhesion	70
5.6.5	Conclusions from the mechanical and tribological investigations	70
6	Summary, conclusions and outlook	73
7	Populärvetenskaplig sammanfattning	76
8	Acknowledgements	80

List of abbreviations

ADF	annular dark field
AE	acoustic emission
BF	bright field
ccp	cubic close packed
CTE	coefficient of thermal expansion
CVD	chemical vapor deposition
DC	direct current
DF	dark field
DOS	density of states
EBSD	electron backscatter diffraction
EDS	energy-dispersive X-ray spectroscopy
ERDA	elastic recoil detection analysis
FIB	focused ion beam
FFT	fast Fourier transform
GI-XRD	grazing incidence X-ray diffraction
HAADF	high-angle annular dark field
HAXPES	hard X-ray photoelectron spectroscopy
HR STEM	high resolution scanning transmission electron microscopy
hsp	hexagonal simple packed
IPF	inverse pole figure
PVD	physical vapor deposition
RBS	Rutherford backscattering spectrometry
SAED	selected area electron diffraction
SCCM	standard cubic centimeter
SEM	scanning electron microscopy
STEM	scanning transmission electron microscopy
TC	texture coefficient
TEM	transmission electron microscopy
TM	transition metal
TMC	transition metal carbide
TM(C,N)	transition metal carbonitride
TMN	transition metal nitride
ToF	time-of-flight
VEC	valence electron concentration
XPS	X-ray photoelectron spectroscopy
XRD	X-ray diffraction

1. Introduction

Cutting tools need to withstand demanding conditions that arise during the metal cutting process, such as high temperatures and high pressures, which result in complex wear situations. The most commonly used cutting tool material is cemented tungsten carbide (called as cemented carbide in the following), which consists of tungsten carbide (WC), a hard ceramic material and a cobalt (Co) binder phase for toughness enhancement. Cemented carbide is usually coated with several layers of ceramic materials with thicknesses in the μm range each. The coating layers have different functionalities, which are determined by their chemical composition, crystalline phase, microstructure, texture and stress state. These properties are tailored by the synthesis parameters. The coatings for cutting tools are synthesized by physical vapor deposition (PVD) and chemical vapor deposition (CVD), which enable material synthesis at much lower temperatures (from room temperature in PVD and typically over $700\text{ }^{\circ}\text{C}$ in CVD) than the melting point of the refractory ceramics (typically $2000\text{--}3000\text{ }^{\circ}\text{C}$). PVD methods include cathodic arc evaporation and magnetron sputtering, where the solid target material is transferred into the vapor phase to form a solid coating on the substrate, i.e. the material to be coated [1]. In CVD, thin films are deposited from volatile precursors that react on the surface of the substrate, with the help of activation, for example thermal activation. The deposition from the gas phase enables an even coating of complex tool geometries. Usually several CVD layers are used, the first layer, typically titanium nitride (TiN) needs to be adherent to the substrate and hinder diffusion between other coating layers and the substrate [1, 2]. The following layers have different functions, for example titanium carbonitride (Ti(C,N)) is harder than TiN, which is desirable against abrasive wear [3], Al_2O_3 is a protective layer against oxidation and it also has a good high temperature hardness [1, 2]. There are several other material layers that are used commercially or being developed. The PVD or CVD method is selected according to the material requirement of the specific application. PVD coatings are often used in intermittent cutting, where their compressive stresses are an advantage against cyclic loading [1]. CVD coated cemented carbides are typically used as indexable inserts for continuous cutting, such as turning. The choice of the deposition method is also dependent on the attainable elemental and phase composition or texture [1, 4].

There is a constant need for the development of new cutting tool materials with the purpose of increasing tool lifetime, making cutting operations more efficient and enabling the machining of new materials. The material development of the cemented carbide and the different coating layers need to be

parallel, since these form a material system together. This thesis focuses on the development of CVD coatings and a substrate that could be compatible with CVD coatings.

In recent years, a new group of materials, multicomponent alloys have been developed, which have multiple principal elements leading to combinations of material properties that differ from conventional alloys having one or two principal elements [5–7]. CoCrFeNi is the base alloy of the Cantor-alloy family and it has been tested as an alternative for Co in cemented carbide [8]. The commercially used CVD process for TiN deposition using TiCl_4 , N_2 and H_2 precursors is carried out at temperatures over 850°C and the reactivity of CoCrFeNi under such conditions needs to be considered for a successful use when the tool with a CoCrFeNi binder phase is coated. The investigation of CoCrFeNi in a CVD process for TiN deposition is the scope of Paper I in this thesis.

Papers II–IV focus on the development of a new coating for cutting tools, tungsten carbonitride ($\text{W}(\text{C},\text{N})$). Tungsten carbide is the main component of cemented carbide, but tungsten-based materials are not yet used as protective coatings for cemented carbide for cutting tools. The aim was to deposit a W-based coating that is similar to the substrate, but exhibits material properties, such as microstructure, texture and hardness that can be tailored by gas phase deposition. The similarity of $\text{W}(\text{C},\text{N})$ with tungsten carbide in the substrate can enable a good coating adhesion and a similar thermal expansion coefficient between $\text{W}(\text{C},\text{N})$ and cemented carbide can eliminate residual tensile stresses, which are a problem in for instance $\text{Ti}(\text{C},\text{N})$ or Al_2O_3 coatings. The thermal cracks that are formed as the tensile stresses are released have been identified as a main source of comb cracks, a failure mechanism of CVD coated milling inserts [9]. $\text{Zr}(\text{C},\text{N})$, for example, is being developed with a similar purpose [1, 9]. The mentioned examples accentuate the importance of the substrate-coating being treated as a whole system together. Furthermore, tungsten-based coatings are also expected to exhibit a better toughness than titanium-based coatings due to their stronger metallic character [10]. Papers II and III describe the development of CVD processes for $\text{W}(\text{C},\text{N})$ deposition using WF_6 , CH_3CN and H_2 precursors, the current understanding of the coating growth and the microstructure of the $\text{W}(\text{C},\text{N})$ coatings. The aim of Paper IV is the mechanical and tribological characterization of the newly developed coatings as a step towards their application.

2. Synthesis method and materials

2.1 Chemical vapor deposition

2.1.1 Key aspects of chemical vapor deposition

Chemical vapor deposition (CVD) is a material synthesis method whereby volatile compounds, precursors, are transported in the gas phase to react and form non-volatile solid materials on the surface of another material, the substrate. The method enables the synthesis of thin films on the 100 nm to several μm thickness scale. These thin films can be used as protective coatings against corrosion, oxidation, mechanical impact, wear, friction, etc. on substrates without sacrificing the properties of the underlying bulk material. In case of cutting tools, hard but brittle ceramic coatings (e.g. TiN , Al_2O_3) are used to protect the cemented carbide (e.g. WC with Co) substrate against wear while preserving the toughness provided by Co in the substrate. CVD can be utilized in other applications such as microelectronics, where material synthesis on a small length scale is required.

The deposition from the gas phase and the mixing of the elements on an atomic scale enables the synthesis of materials at a considerably lower temperature than solid-state synthesis methods, which are limited by solid-state diffusion rates. This is particularly useful for refractory ceramic materials. The synthesis at temperatures where the solid-state diffusion rates are negligible enables metastable microstructures (such as columnar grains) and, together with the atomic-scale mixing, metastable phases. Materials with a preferred crystallographic orientation can be grown due to the directional material growth, a thermodynamic driving force to grow the energetically favorable facets and kinetic effects, since a thermodynamic equilibrium is not reached.

The precursors need to be volatile to be transported to the reaction zone. They also need to be stable enough to only decompose in the reaction zone, where the chemical reactions in the gas phase and on the substrate surface occur upon activation. The system reaches a steady-state by a continuous transport of the precursors to the main reactor chamber while the unreacted precursors, the carrier gas and the reaction by-products are transported away from the reactor. Various types of process activation include thermal, laser-assisted, plasma-enhanced activation or a combination of these. Thermal activation can be achieved by direct heating of the substrate (in cold wall reactors) or by heating of both the gas phase and the substrate (in hot wall reactors) [11]. The reaction rate is also influenced by the partial pressure of the reactants and the total pressure, pressures under atmospheric pressure are achieved by the use of pumps.

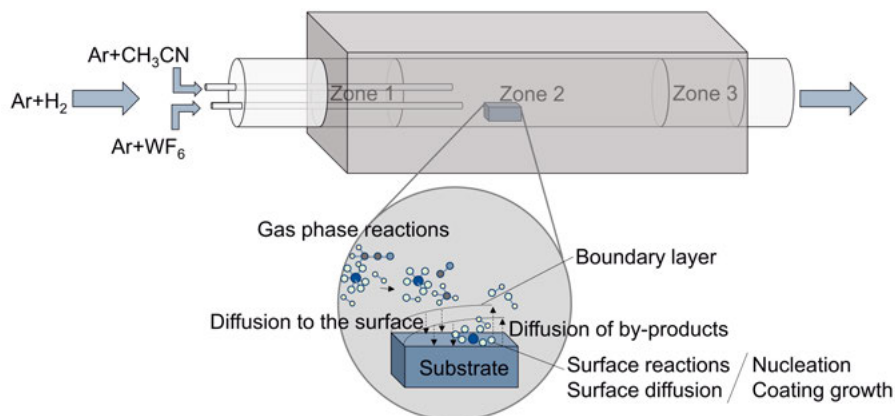


Figure 2.1. A sketch of the CVD reactor used for the deposition of the W(C,N) coatings and the steps of a CVD process.

2.1.2 Reactors used in this thesis

The CVD processes in this thesis were carried out using hot wall reactors. For the deposition of TiN coatings in Paper I a commercial Bernex reactor was used. The W(C,N) coatings in Papers II–IV were deposited using an in-house built tube furnace reactor, specifically designed for WF_6 , TiCl_4 , C_2H_4 , CH_3CN , NH_3 and H_2 precursors. The latter is described in detail in [12] and here only some features that are important for the deposition processes in this thesis are presented. The CVD reactor is a three-zone furnace reactor, where the first zone serves as a precursor pre-heating zone, the second as the deposition zone and the third as a heated zone to counteract the condensation of volatile reaction products and unreacted precursors (see the sketch in Fig. 2.1). A ferritic iron-chromium-aluminum alloy from Kanthal, which is corrosion resistant to most of the precursors, was used in the reactor tube. To further hinder reactions between the reactor tube and the precursors, the reactor was lined inside with a graphite tube. The W- and C/N-source precursors, mixed with Ar carrier gas entered the central deposition zone in separate Inconel 600 pipes, H_2 , also mixed with Ar carrier gas, entered the main tube at the entrance before the pre-heated zone. MKS GM50A mass flow controllers were used to regulate the gas flows, except for the CH_3CN flow, which was regulated by an MKS 1152C mass flow controller. The low pressure was maintained by a Ni-plated S20N type root dry pump from Ebara Technologies. The pressure was controlled with a throttle valve with the help of a 1 Torr full-range MKS 627B temperature stabilized capacitance manometer.

2.1.3 Reaction kinetics in chemical vapor deposition

The choice of the precursors is the first step in the development of CVD processes. In this thesis, transition metal (TM) halides were selected as the source of the metallic elements in the coatings. The advantage of the TiCl_4 and WF_6 precursors is their high volatility. H_2 gas is used for the reduction of these precursors and for halogen atom removal from the precursors. N_2 and CH_4 are commonly used as sources of nitrogen and carbon, but less stable molecules such as NH_3 and CH_3CN enable lower deposition temperatures. N_2 was used for the TiN depositions and CH_3CN for the deposition of $\text{W}(\text{C},\text{N})$ coatings. The reaction mechanism of most CVD processes is complex and not known in all details. However, an investigation of the reaction kinetics can aid the understanding of the chemical reactions during the deposition process.

CVD is a dynamic process where the gas phase over the substrate usually reaches steady state but seldom thermodynamic equilibrium. The steps of the CVD process are shown in Fig. 2.1. When gases flow in a CVD reactor, the flow rate at the surfaces, such as the substrate surface and the reactor walls is close to zero and the concentrations of the vapor species also have a gradient from the central part of the furnace. Between the surface and the central part of the furnace is thus a boundary layer with a gradient in the gas velocity and the concentrations of the vapor species [11, 13]. The precursors need to diffuse through this boundary layer to reach the surface. Because of this layer two kinetic regimes are typically observed in chemical vapor deposition: the reaction kinetics controlled regime and the mass transport controlled regime. When the process is controlled by surface kinetics, the deposition rate is dependent on the reaction steps at the substrate surface. The deposition process can also be controlled by the kinetics of a homogeneous gas phase reaction [13]. A deposition controlled by reaction kinetics at the surface or in the gas phase is usually preferred, since it yields coatings with good conformality. The reaction becomes mass transport controlled if the concentration of one or some of the precursors significantly drops close to the surface. This is the case if the precursor is consumed fast in the surface reaction, for example if the deposition temperature or the partial pressure of other precursors is high. In this case, the diffusion of the limiting precursor through the boundary layer determines the rate of the deposition instead of reactions at the surface.

The two typical kinetic regimes can be studied using an Arrhenius plot ($\ln r$ — $1/T$ plot) which is based on the Arrhenius-equation:

$$\ln r = \ln A - \frac{E_a}{k_B} \cdot \frac{1}{T} \quad (2.1)$$

where r is the growth rate, A is the pre-exponential factor, E_a is the activation energy (in J), k_B is the Boltzmann-constant (in $\text{J} \cdot \text{K}^{-1}$), and T is the temperature (in K). If the Arrhenius-plot is linear, the process mechanism and type of rate control does not change in the investigated temperature range. A change from kinetics control to diffusion control can thus be seen from a changed slope in

the Arrhenius plot [13]. The slope of the regressed line in a linear range gives the activation energy. It is typically 100-300 kJ/mol for a surface kinetics controlled reaction [13]. The reaction rate is further dependent on the precursor partial pressures, following the equation (written for a reaction involving three reactants):

$$r = k \cdot p_A^a \cdot p_B^b \cdot p_C^c, \quad (2.2)$$

where k is the reaction constant, p_A , p_B , p_C are the partial pressures of the precursors and a , b , c are the reaction orders of the respective reactants. Taking the logarithm of the equation:

$$\log r = \log k + a \cdot \log(p_A) + b \cdot \log(p_B) + c \cdot \log(p_C) \quad (2.3)$$

is obtained. Thus, if the partial pressure of a reactant is changed and the total pressure, the temperature and the partial pressures of the other reactants are kept constant by using an inert gas as balance, the reaction order of the selected reactant can be determined. The logarithm of the growth rate as the function of the precursor partial pressure can be plotted and the reaction order can be determined from the slope of the regressed line. True reaction orders are obtained only if the deposition is controlled by reaction kinetics.

2.2 Materials

In this thesis titanium nitride and tungsten carbonitride coatings were deposited by CVD. This section describes the material systems that were developed and investigated. In line with the aim of Paper I, the expected stability of CoCrFeNi as substrate in a CVD process for TiN deposition from TiCl_4 , N_2 and H_2 precursors is discussed. W(C,N) coatings for Papers II–IV were deposited with the aim of synthesizing a new coating on cemented carbide for cutting tools. The material properties that motivated the development of W-based coatings, especially those with a relevance for cutting tools, are described. Considerations behind the choice of the synthesis method are also discussed.

2.2.1 CoCrFeNi and the CVD process for TiN deposition

Since 2004 a new group of materials, multi-principal element alloys (or multicomponent alloys, often called high entropy alloys) have gained interest [5–7]. These materials, compared to conventional alloys, have more principal elements and exhibit some of the properties of those components. In many cases, these alloys form a single phase with fcc or bcc lattice that is either thermodynamically stable or metastable (stable at high temperatures and the high temperature phases are stabilized due to the quick cooling after the synthesis) [14].

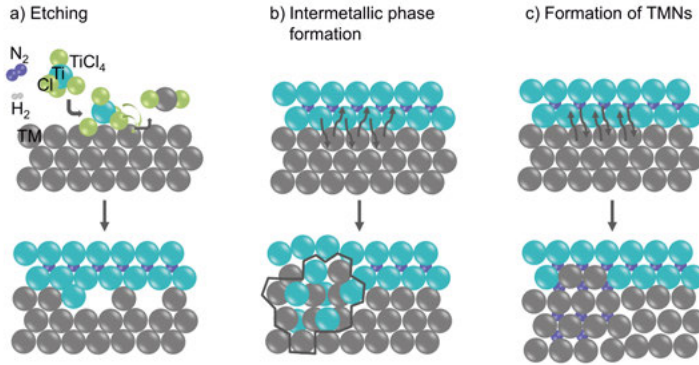


Figure 2.2. Possible reactions between the precursors or the coating and the substrate when TiN is deposited from $TiCl_4$, N_2 and H_2 onto a transition metal substrate in a CVD process

In the development of new materials, an investigation of their compatibility with conventional coating processes is important. CoCrFeNi has been used for example as an alternative binder phase for cemented carbide [8]. A potential application in cutting tools motivates a detailed analysis of the stability of this alloy in the CVD of TiN from $TiCl_4$, H_2 and N_2 at deposition temperatures over $850\text{ }^{\circ}\text{C}$. This means that the substrate needs to withstand a process involving corrosive chemicals at elevated temperatures. During the deposition of TiN onto a TM substrate several reactions can occur between the precursors and the substrate. A Cl ligand transfer from the $TiCl_x$ species to the TM atoms can yield volatile transition metal chlorides and substrate etching occurs (Fig. 2.2.a). HCl, formed in the gas phase from H_2 and $TiCl_4$ can also result in a similar etching reaction. Such etching occurred when $TiCl_4$ was deposited onto an Fe substrate [15]. In a material system where multiple metals are present, such as Ti from the gas phase and metallic substrate components in this case, intermetallic phases can be formed (Fig. 2.2.b). A Ni_3Ti intermetallic phase was formed when TiN was deposited on a Ni substrate [15]. The formation of such a phase was, however, not favored thermodynamically and it was therefore attributed to the deposition kinetics on the Ni surface [15]. When the substrate has a nitride forming element, it may also form a nitride or a ternary nitride together with Ti, if thermodynamically favorable (Fig. 2.2.c). The reaction temperatures (typically over $850\text{ }^{\circ}\text{C}$) can enable a diffusion of the TM into the coating or nitrogen into the substrate. The possible reactions of the CoCrFeNi substrate in TiN CVD summarized in Fig. 2.2 were investigated in Paper I and are discussed in this thesis.

2.2.2 Optimization of the mechanical properties — from Ti-based to W-based ceramic coatings

The material properties of transition metal carbides, nitrides and carbonitrides can be tailored by the choice of the TM and the p-element, and by compositional variations of ternary, quaternary, etc. TMCs, TMNs, TM(C,N)s. These materials have a mixture of metallic, covalent and ionic bonding character [16]. TMCs, TMNs and TM(C,N)s commonly crystallize in a cubic NaCl type structure with a wide homogeneity range and therefore most experimental and related theoretical investigations are carried out for this crystal structure. The transition metal nd orbitals are split to e_g and t_{2g} orbitals. The metallic bonds are formed among the overlapping t_{2g} orbitals of the TMs. The covalent bonds are a result of the overlaps between the p-element $2p$ and TM e_g orbitals (the latter hybridize with the TM ns and np orbitals); as these two types of orbitals are combined, bonding and anti-bonding orbitals are formed [10]. The ionic character is due to charge transfer between the different types of atoms. Depending on the total electron configuration, the extent of the different bonds varies. The character of the chemical bonds determines the mechanical properties of the materials, such as the hardness and brittleness. In general, the covalent character yields higher hardness (and brittleness), the metallic character higher ductility and toughness (and lower hardness) and the ionic character brittleness. The hardness of a material is a measure of its resistance to a permanent shape change under a compressive force and it is commonly measured by tests where the permanent deformation of the material surface as a result of a load is evaluated (definition adapted from [17]). Ductility and toughness are related properties that express the fracture resistance of the material, ductility is related to the strain to fracture and toughness to the absorbed energy to fracture [18]. Hard materials are usually brittle and extensive materials research is being conducted on strategies to synthesize hard and tough ceramic materials, including coatings [10].

The electronic structure of the discussed ceramic materials is often described with a density of states (DOS) diagram, which shows the filling of the mentioned orbitals or more exactly, the bands formed from the orbitals. A commonly used simplified parameter to describe the electronic structure is the valence electron concentration (VEC), which sometimes refers to the VEC of the TM, but commonly to that of the whole material, including the p-elements. By proper alloying of TMs in a material, the VEC can be tuned and the bands of the material are filled according to the DOS diagram. First the covalent bonding orbitals with a lower energy are filled and as the number of TM electrons increases, the t_{2g} orbitals start to get filled, the metallic character of the materials becomes stronger, leading to an increased ductility, while the material still exhibits a high hardness [19]. An increase over a certain VEC destabilizes the material as anti-bonding covalent orbitals start to get filled, which also explains why e.g. carbides of group 7 or higher transition

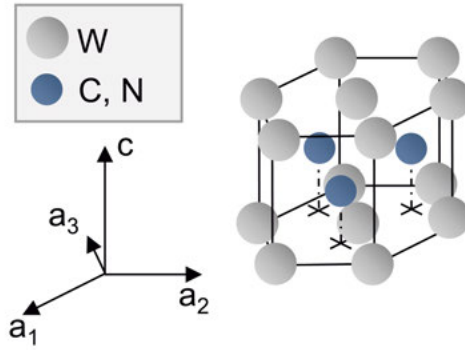


Figure 2.3. The δ -WC type structure for WC, WN or W(C,N) and the 4-index coordinate system.

metals are not stable [20]. The VEC and related properties can also be tuned by varying the N/C ratio and the concentration of TM or p-element vacancies [21]. The electron configuration also determines which crystal structure is the most stable one [21, 22] and for stoichiometric WC or WN the hexagonal δ -WC type structure (Fig. 2.3) is more stable than the cubic NaCl type structure. Other than the mechanical properties, the coefficient of thermal expansion (CTE) is also influenced by the composition. The CTE of titanium based materials for example gradually increases as the composition changes from TiC to TiN [23].

In this thesis Ti and W based ceramic coatings were synthesized, TiN has a VEC of 9 and W(C,N), based on the compositions reported in section 5.5, has a VEC of 10.3. Based on simply the VEC, W(C,N), the new CVD coating synthesized in this thesis, was expected to exhibit a higher toughness but a lower hardness than TiN or Ti(C,N), both used commercially. The VEC is, however, not the only parameter that determines the mechanical properties of ceramic materials. The possibility for dislocation slip is also critical for the plastic deformation of the materials and thus the material hardness and toughness. The slip systems are determined by the crystal structure, and which slip system is activated, i.e. energetically favored, depends on the electronic structure of the material [10] and the temperature. The slip system of the NaCl structure consists of $\{100\}\langle 110\rangle$, $\{110\}\langle 110\rangle$ and $\{111\}\langle 110\rangle$ slips, 24 in total [24]. For WC with a δ -WC structure $\{1\bar{1}00\}$ was determined as the preferred slip plane with $\langle 11\bar{2}0\rangle$ and $\langle 0001\rangle$ as postulated slip directions in [25], $\{10\bar{1}0\}\langle 11\bar{2}3\rangle$ was also determined as a slip system in [26], but basal and pyramidal slips may also be possible. A thorough comparative study between the mechanical properties of the cubic γ -WC_{1-x} and the hexagonal δ -WC has not been carried out yet (phase names according to [27]). Therefore, a complete comparison between the δ -WC type structured W(C,N) and the cubic

Ti-based ceramic materials is not possible. Furthermore, extrinsic properties, such as the microstructure or residual stresses of the materials also affect the mechanical properties, since different types of defects can inhibit dislocation movement or the propagation of cracks.

2.2.3 Mechanical properties of W-based ceramic coatings

The mechanical properties of W(C,N) are expected to be between those of WN and WC. In general, following the above described principles (section 2.2.2), the carbide of a TM is harder than the nitride of the same TM. W-based coatings are expected to have a lower hardness than Ti-based coatings based on the VEC, but no studies discuss the effect of a different crystal structure. The microhardness of TiC (28 GPa) is higher than that of WC (25 GPa) according to a summarizing table in [28]. The hardness values of the materials vary in a wide range depending on their microstructure, synthesis method and the measurement method. As summarized by Csanádi et al. [29], reported hardness values for bulk WC vary widely, between 10 and 30 GPa, in the same publication a basal nanohardness of 43 GPa and a prismatic nanohardness of 28 GPa were reported. The Ar⁺ milling used to prepare a flat surface in [29] may have introduced defects close to the surface, which could be the cause for the significantly higher hardness values than typically reported. When using mechanical polishing instead, the nanohardness of the {0001}-plane was 30 and that of the prismatic {10 $\bar{1}$ 0}-plane was 23 GPa in [30]. The reported elastic modulus of values of WC range between 623 and 722 GPa [31, 32]. The Poisson's ratio of WC is between 0.18 and 0.21 based on earlier calculations or experiments [31, 33]. The mechanical properties of tungsten nitrides (mostly cubic) and tungsten carbonitrides were primarily evaluated for PVD coatings, where the compressive stresses and microstructure influenced the hardness values. Typical hardness values of reactively sputter deposited tungsten nitride films ranged between 30 and 40 GPa [34–36]. The Young's modulus values ranged between 275 and 430 GPa. The direct current (DC) magnetron sputtered δ -WC structured W(C,N) thin films exhibited hardness values of 40–49 GPa, remaining over 40 GPa after annealing for 2 hours at 800°C in vacuum (10⁻⁴ Pa), which decreased the residual compressive stresses of the coatings to 1 GPa [37, 38]. For comparison, the hardness of CVD Ti(C,N) coatings is typically between 20–25 GPa, but hardness values close to 40 GPa were achieved for {111} textured Ti(C,N), together with a compressive residual stress [39]. To sum up, the hardness value of a bulk W(C,N) would be most probably close to 25 GPa, but as a coating it can exhibit higher hardness values depending on the microstructure and the state of the residual stress in the coating.

The determination of the fracture toughness is also dependent on the measurement method as described in [40], the authors determined microcantilever

bending tests to be the most reliable method for toughness measurement of WC grains, yielding a fracture toughness of $5.6 \pm 1.0 \text{ MPa} \cdot \text{m}^{1/2}$. An orientation-dependent fracture toughness was measured by micropillar or cube corner tests, respectively resulting in 2.5 ± 1.0 or $7.2 \pm 2.4 \text{ MPa} \cdot \text{m}^{1/2}$ for the basal and 5.0 ± 1.0 or $8.7 \pm 1.1 \text{ MPa} \cdot \text{m}^{1/2}$ for the prismatic toughness [40, 41]. These values are higher than what was determined for TiC by indentation methods in [42], i.e. $2\text{--}4 \text{ MPa} \cdot \text{m}^{1/2}$.

2.2.4 W(C,N) — a material similar to the cemented carbide substrate

As the main bulk component of cutting tools, most commonly WC with a stoichiometric composition and a corresponding δ -WC type structure is used together with a Co binder phase for an improved toughness. One of the aims when depositing W(C,N) coatings on cemented carbide was to obtain a coating material that is similar to the cemented carbide substrate, but has a different microstructure provided by the CVD process and does not contain Co. One expected advantage was a similar coefficient of thermal expansion (CTE) between the coating and the substrate. CVD is carried out at elevated temperatures and a higher CTE of conventional coatings such as Ti(C,N), Al_2O_3 compared to the substrate is detrimental [43–45]. Often a tensile stress is introduced in the coatings, which can result in thermal cracks as a critical stress level is reached [43, 44]. Zr(C,N) is an alternative to Ti(C,N) with a lower CTE [1, 46]. W(C,N) is likely to have a similar CTE to that of WC, and thus compressive residual stresses can be introduced into W(C,N) coatings depending on the Co content of the substrate and on how the N changes the CTE of WC — for Ti(C,N) it increases the CTE compared to TiC [23, 47, 48]. Another expected advantage of a W(C,N) coating on cemented carbide was a strong adhesion to the substrate due to the chemical similarity. In this thesis WC with 12 wt. % Co was used, which contained 1.5 wt. % TaC/NbC. An issue with cemented carbide in CVD processes is that the binder phase can react with the gas phase species. With W and C, for example, a low carbon containing η -phase can be formed at the substrate-coating interface. η -phase formation is not unique for CVD, it is also obtained if the cemented carbide is produced outside of the carbon window.

2.2.5 Deposition of W(C,N) coatings

There are several room temperature and high temperature phases in the binary W-C and W-N phase diagrams [49, 50] and accordingly a variety of phases are obtained in PVD and CVD processes based on the obtained stoichiometry and kinetic effects. The W-C-N phase diagram has not been investigated yet, but solid solutions of isostructural phases from the binary phase diagrams are

expected to exist. In this thesis the crystalline phases are denoted based on [27]. The aim was to deposit W(C,N) coatings crystallized with hexagonal δ -WC type structure, a structure with a narrow homogeneity range in both binary phase diagrams [49, 50].

It is common that cubic γ -WC_{1-x}-type tungsten carbide, nitride or carbonitride or a W₂C-type tungsten carbide or multiple phases are obtained in PVD, CVD or atomic layer deposition [51–63]. To achieve the hexagonal δ -WC type phase coatings in PVD, substrate heating and bias have been applied [34, 37, 38]. In CVD, WF₆ or WCl₆ are commonly used as W precursors [58, 64, 65]. The decomposition and reduction of these precursors is generally rapid at temperatures where saturated hydrocarbon and nitrogen precursors decompose, i.e. approximately over 750 °C [66]. A way to overcome this discrepancy of precursor stability is to choose a less stable C or N precursor than saturated hydrocarbons, such as (CH₃)₃N or CH₃CN [66–68]. Only W and C and no N was reported in the coatings when using the latter precursors [67, 68]. Tägtström et al. also proposed low process pressure (100 mTorr) and very high linear flow velocity (7 m/s) of the gas phase to avoid a rapid depletion of WF₆ at the front of the tube furnace reactor to achieve a more even film thickness throughout the reactor and a δ -WC type phase [64].

3. Characterization methods

3.1 X-ray diffraction

X-ray diffraction (XRD) is a versatile method for the characterization of crystalline materials. A schematic drawing of the XRD measurements including a coated substrate is shown in 3.1. Parallel crystallographic planes with a $\{hkl\}$ Miller index can be detected based on constructive interference of coherent X-rays diffracted by the electrons of the atoms in the material. The constructive interference occurs at a characteristic Bragg angle (2θ) when the Bragg condition according to equation 3.1 is fulfilled, where λ is the wavelength of the X-ray radiation and d_{hkl} is the distance of the crystallographic planes with a $\{hkl\}$ Miller-index. The intensity of the resulting peak in the X-ray diffractogram is dependent on the structure factor, which is determined by the type of atoms and their positions in the unit cell. The structure factor is described in more detail elsewhere [69].

$$\lambda = 2d_{hkl}\sin\theta \quad (3.1)$$

The Bragg angles and the corresponding peak intensities of crystalline materials with a random crystal orientation can be retrieved from databases; in this thesis the Pearson's Crystal Data database [70] was used. References are made to the original publications from which the peak positions and intensities were calculated in the database. In different diffractometers the X-ray source, the detector and/or the sample stage can be positioned according to the angles shown in Fig. 3.1. In the symmetric mode, where the incident beam is $\omega=\theta$, only planes parallel to the sample surface are measured (see grain A in Fig. 3.1 as an example). If the sample is textured, i.e. a certain set of planes is overrepresented parallel to the surface, these planes will have a relatively higher intensity in the diffractograms. The dominant texture of the sample can be determined by calculating the texture coefficients (TCs) of the planes according to equation 3.2, where $I(hkl)$ is the peak intensity, n is the number of hkl reflections used, $I_0(hkl)$ is the reference peak intensity. For a randomly distributed material, all texture coefficients are equal to 1.

$$TC(hkl) = \frac{\frac{I(hkl)}{I_0(hkl)}}{\frac{1}{n} \sum_{x=1}^n \frac{I(h_x k_x l_x)}{I_0(h_x k_x l_x)}} \quad (3.2)$$

The incoming and the diffracted beam is attenuated by the material and only a small volume of the material is sampled. When measuring thin films, the penetration depth of the X-ray beam might be larger than the sample thickness.

At different incident angles different volumes of the coating will be sampled. Therefore, the measured intensity of each peak needs to be corrected according to the incident angle for a fair comparison with the $I_0(hkl)$ values of bulk materials [71]. If the substrate peaks overlap with the coating peaks, their intensities — considering the absorption by the coating — need to be corrected for as well.

The texture coefficient gives an information about the dominant orientation of the grains in the coating, but it does not give information on how widely the orientation is distributed. The distribution of a certain grain orientation can be measured by recording rocking curves. In these measurements the 2θ angle is kept constant and the ω angle is varied. As illustrated in Fig. 3.1, grains A and B, which are similarly oriented, will fulfill the Bragg condition at different ω angles. In this thesis the grains of the coatings had a wide orientation distribution and therefore, the rocking curves needed to be corrected for the different interaction volumes at different ω angles, similar to the texture coefficients. Due to a wide scanning angle, even the substrate with randomly oriented grains showed a non-constant intensity and therefore the rocking curves were also corrected based on the rocking curve of the substrate.

The in-plane rotation of the sample (ϕ) and the ψ angle can also be varied and pole figures can be recorded. This measurement has a relevance when the substrate is single crystalline and the coating may have an epitaxial relation to the substrate. This was not the case for the substrates used in this thesis and such XRD measurements were not carried out. Pole figures are, however, shown based on the electron backscatter diffraction measurements (see section 3.3).

For thin coatings, which would give low intensities in a symmetric scan, the sampling volume can be increased by using a low ω angle. This method is called grazing incidence X-ray diffraction (GI-XRD). The texture of the coatings cannot be easily deduced from GI-XRD measurements.

The measurement of the cell parameters at different ψ angles can be utilized to calculate residual stresses in the coatings. The $\sin^2\psi$ method is based on equation 3.3. In the equation ε_ψ is the strain at a ψ angle, which is calculated from the strained and unstrained cell parameter, the latter estimated from the stress measurements as described in [71], ν is the Poisson's ratio, which was assumed to be 0.2, E is the elastic modulus and σ_\parallel is the biaxial residual stress.

$$\varepsilon_\psi = \frac{1 + \nu}{E} \sigma_\parallel \sin^2\psi - \frac{2\nu}{E} \sigma_\parallel \quad (3.3)$$

The equation is based on the generalized Hooke's law, and is obtained by the transformation of the strain measured in the laboratory coordinate system to the sample coordinate system (for the derivation see [71]). The residual stress can be obtained from the slope of the measured cell parameter– $\sin^2\psi$ plot. For the calculation of the residual stresses in the W(C,N) coatings, a Poisson's ratio of $\nu=0.2$ and the elastic modulus values determined by nanoindentation

were used. Since the method assumes an anisotropy of the material parameters and a constant stress in the whole coating, it is rather used for an estimation than an accurate determination of the residual stresses.

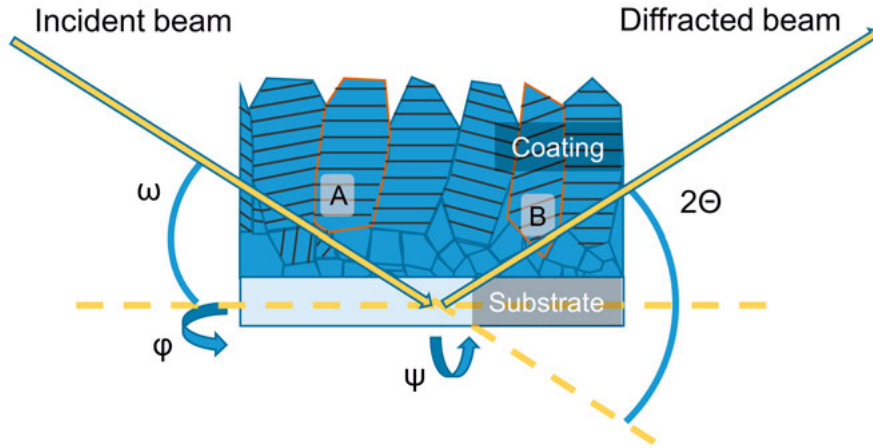


Figure 3.1. Schematic drawing of an XRD setup and a typical columnar CVD coating on a substrate. ω is the incident angle, which can be modified by tilting of the sample or moving of the X-ray source, 2θ is the detector angle, ψ is the tilt angle and ϕ is the in-plane rotation angle. Grains A and B are two similarly oriented grains and their indicated planes fulfill the Bragg condition at different ω angles.

3.2 Scanning electron microscopy

Scanning electron microscopy (SEM) utilizes the interaction of accelerated electrons (1–40 kV acceleration voltage [72]) with the material. It is used for imaging elemental variations or the topography and microstructure of samples by the detection of elastically backscattered electrons or secondary electrons emitted from the material as a result of inelastic scattering. Characteristic X-rays are also emitted as a result of the inelastic scattering and excitation of the atoms in the material. These characteristic X-rays can be used for compositional analysis of the material, for example through energy-dispersive X-ray spectroscopy (EDS). In this thesis SEM was used for the characterization of the coating top morphologies, cross-sections and the analysis of the scratch tracks and micro abrasion craters in the tribological tests (see sections 3.8 and 3.9 for the description of the tribological tests). Zeiss 1530/1550 and Merlin microscopes with a Schottky field electron gun, in-lens, secondary electron detectors and a 80 mm² silicon drift EDS detector were used.

3.3 Electron backscatter diffraction

Electron backscatter diffraction (EBSD) is carried out in the SEM. A flat material surface is tilted at an angle of typically 70° from the horizontal direction. The incident electrons are diffusely scattered in the specimen [73]. Some of the diffusely scattered electrons travel at a Bragg angle (θ) to a certain crystal plane (on either side of the plane) and will be diffracted by the plane. Since electrons travel at different angles, two cones of backscattered electrons are formed, with an opening angle of $90^\circ - \theta$ on the two sides of the planes. A section of the cones is captured as parallel straight Kikuchi lines, enclosing a band on a phosphor screen [74]. The center of the band is a projection of the scattering plane. If the crystal structure of the specimen is known, the crystal orientation of the mapped grains can be calculated from the orientation of the Kikuchi lines. This is normally carried out by a software and the orientation of each measurement point is stored. The stored data is used to represent the orientation of the sampled volumes by for example inverse pole figure maps (IPF maps) or pole figures. EBSD was used in this thesis to analyze the grain morphology, the grain size and the orientation of the grains of the W(C,N) coatings. The EBSD data was recorded in the Zeiss Merlin microscope, which was equipped with a Nordlys Max detector. The EBSD data were evaluated in the Oxford Instruments NanoAnalysis Aztec Crystal 1.1 and 2.0 software.

3.4 Transmission electron microscopy

Transmission electron microscopy (TEM), similarly to scanning electron microscopy, uses accelerated electrons for imaging, crystallographic characterization or elemental analysis of materials. A higher voltage, typically 100–300 kV is used to accelerate the electrons, which are transmitted through a thin specimen with a thickness up to approximately 100 nm. The contrast in TEM images stems from the deflection of part of the electron beam by the specimen [72]. Mass-density contrast (Z-contrast) is a result of the interaction between the electrons and the nuclei of the sample atoms. Electron diffraction by crystalline samples results in diffraction contrast. As a result of electron diffraction, diffraction spots are formed on the back-focal plane [72]. The central spot corresponds to the direct beam and is selected for bright field (BF) imaging. The other spots can be chosen by tilting the beam for dark field (DF) imaging. Diffraction contrast in the BF image can be used to analyze crystallographic defects in the sample, but the Z-contrast is also present in the BF images.

For crystallographic characterization of the sample, selected area electron diffraction (SAED) can be carried out on a smaller area of the sample by using a beam aperture and focusing the back-focal plane with the diffraction spots on the camera.

Scanning transmission electron microscopy (STEM) is another mode of imaging, where the electron beam is focused into a small probe and is scanned over the specimen, similarly to the SEM, except the beam is kept parallel to the optical axis [73]. The scattered electrons can be collected by BF, annular dark field (ADF) or high-angle annular dark field (HAADF) detectors, the image in the latter case may be free from diffraction contrast when a proper detector angle and camera length, i.e. the distance between the specimen and the plane of the diffraction spots are selected. The advantage of STEM over TEM is that the STEM image is not magnified and is thus free from aberrations from the objective lenses, instead the probe has aberrations stemming from the lenses forming it [73]. The probe is, however, aberration corrected in many modern microscopes. For the characterization of the samples in this thesis FEI Titan 80–300 and FEI Titan G2 TEM/STEM instruments were used.

3.5 Ion beam analysis techniques

Time-of-flight elastic recoil detection analysis (ToF-ERDA) and Rutherford backscattering spectrometry (RBS) are methods based on the interaction of ions with energies in the MeV range and the atoms of the characterized material, the target. These techniques are commonly used for the analysis of the chemical composition of materials. In ERDA, elastically recoiled target nuclei are detected. For the experiments in this thesis the energy and number of the recoiled atoms were measured by a gas ionization chamber placed after a time-of-flight analyzer. The combination of the detector and the ToF analyzer enables a coupled measurement of the energy and mass of the particles and thus the identification and depth profiling of the elements (the energy of the recoiled particles is, due to their interaction with the target electrons, also dependent on the depth they are displaced from). ERDA has been widely used for the concentration determination of ceramic materials containing both light and heavy elements [21, 75–77] and its main strength is that it can differentiate between light elements [78]. It was, however, shown for titanium, zirconium and hafnium borides that the accuracy of ERDA can be limited if elements to be detected in the material are heavier than the probing ion used for the analysis [79].

The ERDA measurements were carried out with $^{127}\text{I}^{8+}$ ions with an energy of 36 MeV. The incident angle was 67.5° from the surface normal and the detection angle of the recoil atoms was set to 45° . For the compositions in Paper II the atomic concentrations were integrated between $250\text{--}350 \times 10^{15}$ and 2000×10^{15} atoms/cm² into the samples from the surface, corresponding to an analysis depth of approximately 30–200 nm. A new set of measurements was later carried out where the atomic concentrations were integrated between 250×10^{15} atoms/cm² and 800×10^{15} atoms/cm², which are shown in this thesis. The raw data was analyzed using the Potku software [80].

RBS measurements are performed with light ions of lower energy than ERDA measurements and the ions are backscattered as a result of collisions with the target nuclei. Energy loss of the backscattered ions occurs due to the elastic collision with the sample atoms and additionally, due to interaction with the electronic system when the ion travels into the target prior to and out of the target after the collisions [78]. Therefore, the energy of the backscattered ions is dependent on the elements of the target and their depth in the material, enabling depth profiling of the material. RBS is most suitable for the determination of the concentration of heavy elements and therefore would, as a stand-alone technique due to signal overlap, not improve the concentration determination of the comparably thick W(C,N) coatings that were synthesized in this thesis as a complementary technique of ERDA. Instead, a relative RBS measurement was used, where the W(C,N) coatings were measured in parallel with a W standard. The ion beam was periodically switched between the coatings and the standard, which allows to determine the incident fluence of ^4He ions. In this way the relative amount of tungsten can be determined in W(C,N) by comparing the signal intensity to pure W, providing a light element/W atomic ratio. The relative light element concentrations were determined by ERDA measurements. The RBS measurements were carried out using ^4He ions with an energy of 2 MeV and the beam current was 15 nA. An angle of incidence of 5° with respect to the surface normal and a scattering angle of 170° were applied.

3.6 X-ray photoelectron spectroscopy

X-ray photoelectron spectroscopy (XPS) is used for chemical analysis of materials. As the material is irradiated by X-rays, photoemission of electrons occurs. The emitted photoelectrons will have a characteristic kinetic energy depending on the energy of the incoming photons and the binding energy of the electrons in the material. The binding energy is determined primarily by the energy levels of the atom that the electron is emitted from. The chemical environment of the atoms in a material results in a shift of the binding energies, the so-called chemical shift. The kinetic energy of the photoelectrons is measured and the chemical environment of the atoms can be determined from the calculated binding energies. The X-rays in a laboratory scale XPS instrument are generated from an X-ray tube and are monochromatized to a single characteristic X-ray line of the anode material, where they are emitted from. Most commonly Al $K\alpha_1$ (1.485 keV) or Mg $K\alpha_1$ (1.254 keV) radiation is used. These photon energies give an information depth of a few nm, which is similar to the thickness of the native surface oxide present on the surface of many materials. To study the material below the oxide it is common to apply Ar^+ etching prior to the acquisition. This etching, however, can result in material damage, and change the chemical environment of the atoms [76, 77, 81].

The laboratory scale XPS measurements in this thesis were carried out using a Phi Quantera II scanning XPS microprobe with Al $K\alpha_1$ radiation. The setup is regularly calibrated using reference samples of Ag, Au and Cu according to the ISO standard 15472 [82].

Another way of obtaining information from deeper in the material is by using X-ray photons with a higher energy (hard X-rays). Hard X-rays with a high intensity are accessible at synchrotron beamlines, where X-ray energies can be selected by monochromators. The hard X-ray photoelectron spectroscopy (HAXPES) measurements in this thesis were carried out at the GALAXIES beamline of the SOLEIL synchrotron, Saint-Aubin, France [83, 84]. Two X-ray energies, 2.3 keV and 8.0 keV, were used to vary the analysis depth. The binding energy scales of the HAXPES spectra were referenced versus the Fermi edge of the samples, the low spectral resolution at 8 keV hindered an accurate determination of the Fermi edge. The peaks of the valence band were used to adjust the binding energy scale to the 2.3 keV binding energy scale and in this way the strongest N 1s and W 4f core level peaks (but not the C 1s peak) also matched for the two photon energies. The analysis depths using 1.5 keV (XPS), 2.3 keV and 8 keV photon energies were estimated to be 6 nm, 9 nm and 27 nm by calculations based on [85].

3.7 Nanoindentation

Nanoindentation is used for the measurement of hardness, elastic modulus and fracture toughness of the materials. The sample is indented in a controlled way with a small tip made of a hard material. The load and the indentation depth are recorded during the measurement and an indentation curve is produced, see Fig. 3.2.a. The size of the remaining indented area depends on the plastic deformation of the material and is used together with the maximum indentation load to calculate the hardness. The size of the indented area is normally calculated from the indentation depth after the elastic recovery, utilizing the tip geometry [17]. For shallow indentation depths the tip geometry is calibrated by indentation of a standard material; SiO₂ was used for the calibrations in this thesis. The slope of the unloading curve is related to the elastic recovery of the material and is used to calculate the elastic modulus [17].

A Berkovich diamond tip was used for hardness and elastic modulus measurements in this thesis and the calculations were based on the Oliver & Pharr method [86].

Radial cracks will form in the material at the edges of the indent when high enough loads are used. The tip geometry can be optimized to lower the threshold for crack initiation [87]. A tip with a cube corner geometry is sharper than a Berkovich tip and thus introduces larger local stresses in the indented material. The fracture toughness of the coating can be calculated from the crack lengths using the following formulas [87, 88]:

$$K_{Ic1} = \alpha \left(\frac{E}{H} \right)^{\frac{1}{2}} \frac{P}{c^{\frac{3}{2}}}, \text{ or} \quad (3.4)$$

$$K_{Ic2} = \chi_v \left(\frac{a}{l} \right)^{\frac{1}{2}} \left(\frac{E}{H} \right)^{\frac{2}{3}} \frac{P}{c^{\frac{3}{2}}}. \quad (3.5)$$

The choice of the equation depends on the crack geometry, which is determined by the material. The typical crack geometries are shown in [89]. Equation 3.4 assumes half-penny morphology for the cracks and is sometimes used for calculation of fracture toughness of ceramic coatings [90]. Half-penny cracks, however, normally occur for brittle glasses [88]. Palmqvist cracks were instead shown to occur for indentation of WC [89] or other ceramic materials and equation 3.5 estimates the fracture toughness of such coatings more accurately. In the equations K_{Ic1} or K_{Ic2} [$\text{MPa} \cdot \text{m}^{1/2}$] is the fracture toughness, $\alpha=0.036$ and $\chi_v=0.057$ are calibrated constants for a cube corner indenter [87, 91], P [mN] is the maximum load, a , l and c [μm] are crack lengths according to Fig. 3.2.b. E [Pa] and H [GPa] are the elastic modulus and hardness of the coating, determined by nanoindentation with a Berkovich diamond tip in this thesis.

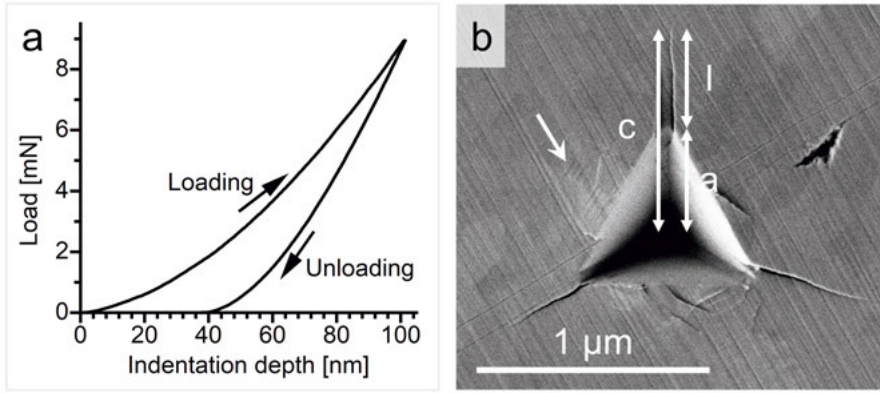


Figure 3.2. a) An example of a nanoindentation curve (material: W(C,N) coating on cemented carbide) b) an indent made with a cube corner tip, where radial cracking occurred (material: W(C,N) coating on cemented carbide, load: 50 mN, loading and unloading rate: 15 mN/min). In b) an arrow indicates slip traces, a , l and c are crack lengths used as variables in equations 3.4 and 3.5.

Not all materials will behave the same way. The deformation of the indented material can give qualitative information on its crack resistance even when no cracks are formed. An Ultra Nano Hardness Tester from CSM Instruments was used for the measurements in this thesis and the calculations were carried out in the CSM instruments indentations software V5.14.

3.8 Scratch tests

Scratch tests are primarily used to investigate the coating adhesion to the substrate, but also the crack resistance of the coating. Normally, a hard Rockwell C type tip is drawn over the sample surface at a controlled load. A critical load (L_c) is determined at the starting point of a certain material failure type and several critical loads can be determined depending on the number of different failure mechanisms.

Scratch tests are commonly carried out by gradually increasing the load within one scratch to determine the critical load. This method was used in this thesis, when a 50 μm radius Rockwell C diamond tip was used at a linearly increasing load between 1 N and 30 N over a 3 mm scratch length. The ratio between the tip radius and the coating thickness determines where the cracking occurs primarily [92]. At a low ratio, the stress is mostly concentrated to the coating, enabling the investigation of its cohesive strength. This kind of failure was expected for the tip with the 50 μm radius. When the tip radius is larger, the stress under the tip is more distributed, reaching the substrate-to-coating interface or the substrate. This case is suitable for the investigation of the coating adhesion. The type of failure is also strongly dependent on the ductility of the substrate and the coating as well [93]. In this thesis scratch tests with a 200 μm Rockwell C diamond tip were carried out for the investigation of the coating adhesion. The load was increased linearly between 1 N and 75 N over a scratch length of 3 mm in multi-pass scratch tests, with five scratches carried out in the same track. This is a simplified version of a method that was proposed to enable fatigue wear at loads lower than the critical load for a single-pass scratch test [94]. The advantage of a lower load is that the plastic-elastic deformation of the substrate and its effect on the adhesive failure (during elastic recovery) is minimized [94].

The scratch tests were carried out using an Anton Paar Revetest micro scratch tester. The critical loads were determined with the help of acoustic emission (AE) signal recorded during the scratch tests. The AE signal indicates cracking in the material and a higher AE level indicates a more severe cracking in the material. Thereby the AE signal aids the determination of the critical load for material failure. SEM imaging was used for qualitative analysis of the scratch tracks.

3.9 Abrasive wear tests

Abrasive wear occurs usually when a harder particle or asperity slides against a softer material. During metal cutting abrasive wear can be caused by for example hard inclusions in the workpiece material (e.g. tool steel or Inconel 718) or loosened particles from the cutting tool. The abrasive wear resistance is usually proportional to the material hardness [3], but it is also dependent of the wear mechanism. A mild and preferable material removal mechanism is

micro cutting. Micro plowing transfers material to the sides of the abrasive wear track. A more aggressive mechanism is micro chipping, which results in a less predictable material performance.

A Gatan 656 dimple grinder equipped with a stainless steel wheel of a 10 mm radius was used for the experiments in this thesis and the wheel was submerged in a slurry of 1 μm diamond particles on top of the samples. The diameter of the craters was determined from SEM imaging to calculate the wear rate κ using the following formula [95]:

$$\kappa = \frac{\pi b^4}{64R SL}, \quad (3.6)$$

where b is the crater diameter, R is the wheel radius, the numerator is an estimate of the wear volume valid if $b \ll R$. In the denominator S is the sliding distance and L is the load. The wear mechanism was analyzed with the help of SEM imaging and the fraction of the area where micro chipping occurred was determined by a point grid method, with grid points enclosing areas of a 10 μm^2 square.

3.10 Calculation of phase diagrams

Calculation of phase diagrams (CALPHAD) is a method for the calculation of the thermodynamically stable phases given the atomic concentrations of the components of the system under certain conditions such as temperature and pressure. The thermodynamic properties of the included phases are stored in databases, which are used to construct a characteristic state function, usually the Gibbs free energy of the phases. The thermodynamically stable phases and their concentrations are determined by the minimization of the total Gibbs free energy of the system. For the thermodynamic calculations in Paper I in this thesis the Thermo-Calc software was used [96].

4. Scope of the thesis

This thesis is based on two chemical vapor deposition research projects. The aim of the first project was to assess the substrate stability of a CoCrFeNi substrate in conventional CVD of TiN using TiCl_4 , N_2 and H_2 precursors and thermal activation, and to identify possible detrimental reactions involving the CoCrFeNi substrate. The results of these investigations have been published in Paper I.

The second research project (Papers II–IV) focused on the synthesis of a new CVD coating, tungsten carbonitride ($\text{W}(\text{C},\text{N})$), on cemented carbide. The investigations on $\text{W}(\text{C},\text{N})$ deposition, the material properties of the $\text{W}(\text{C},\text{N})$ coatings and the entire $\text{W}(\text{C},\text{N})$ coating–cemented carbide substrate system included the following:

- Definition of a process window for the deposition of hexagonal δ -WC type $\text{W}(\text{C},\text{N})$ coatings.
- A kinetic investigation to understand the role of the precursors — WF_6 , CH_3CN and H_2 — in the deposition processes.
- The growth of the coating, as well as the microstructure and texture of the coating, were investigated and related to each other using X-ray and electron diffraction and electron microscopy imaging.
- The compositions of the coatings and the chemical environments of the elements in the coatings were determined. Challenges associated with compositional and spectroscopic analyses of coatings containing light (C and N) and heavy elements (W) were discussed.
- Mechanical and tribological tests were carried out on the $\text{W}(\text{C},\text{N})$ coatings on cemented carbide. The investigations focused on the hardness, toughness, abrasive wear and adhesion of the coatings to determine the key material properties that could be interesting for cutting tools. The best performing coatings were identified.

5. Results and Discussion

5.1 TiN deposition on a CoCrFeNi substrate

The chemical vapor deposition of TiN onto a CoCrFeNi substrate was investigated by post-deposition characterization and the experimental results were predicted and interpreted by thermodynamic calculations. Three CVD processes were carried out at different temperatures as shown in Table 5.1. The possible reactions between the precursors or the TiN coating and the substrate are summarized in Fig. 2.2 in section 2.2.1. These reactions were evaluated in Paper I. Thermodynamic calculations were carried out to predict the possibility of substrate etching (Fig. 2.2.a). In the calculation input, the molar concentrations of the metallic elements were adjusted to their respective concentrations in the alloy and the concentration of Ti was set equal to the other metallic elements. The molar concentrations of Cl, H and N were set according to their experimental atomic ratios in the gas phase (Table 5.1). The calculations showed that it is most probably Cr that is etched if substrate-gas phase interactions occur. Cross-section images of the samples showed that no severe substrate etching occurred (Fig. 5.1.d–f). At the lowest deposition temperature voids were observed at the substrate-to-coating interface (Fig. 5.1.d). The substrate roughness was, however, similar after all the three depositions at different deposition temperatures. The voids that formed during the deposition at 850 °C rather formed on top of the substrate, at the bottom of the coating, probably due to a slow nucleation compared to the growth rate. This resulted in grains that did not fill the whole volume at the initial deposition stage.

Neither the cross-section images nor the X-ray diffractograms indicated the formation of any intermetallic phases (Figs. 2.2.b, 5.1, 5.2), showing that CoCrFeNi performed better than elemental Ni as a substrate for TiN CVD [15]. Thermodynamic calculations, where the N/H mole fraction was allowed to vary and the metallic elements were included with equal mole fractions, showed that Ni_3Ti is only stable at extremely low N activities.

Table 5.1. *TiN CVD synthesis parameters used in Paper I*

T [°C]	p(TiCl ₄) [Pa]	p(H ₂) [Pa]	p(N ₂) [Pa]	p _{total} [Pa]	Deposition time
850	$1.0 \cdot 10^3$	$19.5 \cdot 10^3$	$19.5 \cdot 10^3$	$40.0 \cdot 10^3$	6 h
900	$1.0 \cdot 10^3$	$19.5 \cdot 10^3$	$19.5 \cdot 10^3$	$40.0 \cdot 10^3$	5 h 30 min
950	$1.0 \cdot 10^3$	$19.5 \cdot 10^3$	$19.5 \cdot 10^3$	$40.0 \cdot 10^3$	5 h

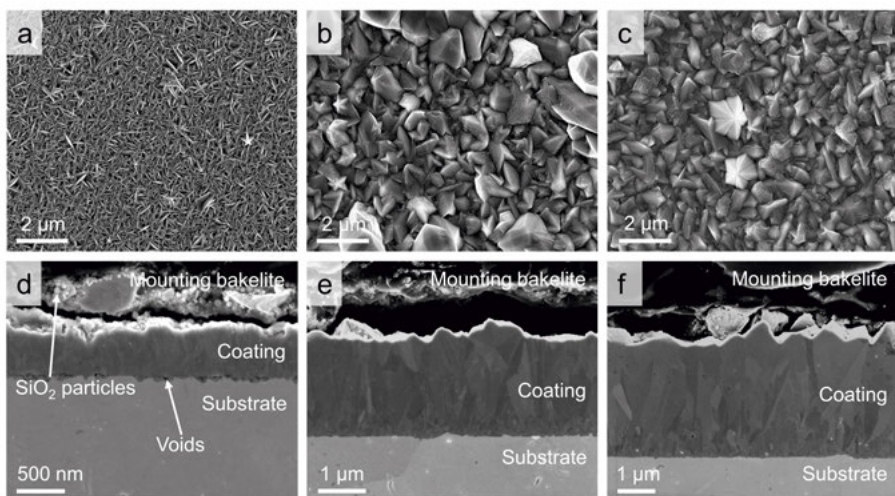


Figure 5.1. In-lens SEM images of a–c) the top surfaces and d–f) the cross sections of the TiN coatings deposited on CoCrFeNi substrates. The deposition temperature was 850 °C in a) and d), 900 °C in b) and e) and 950 °C in c) and f). Adapted from Paper I.

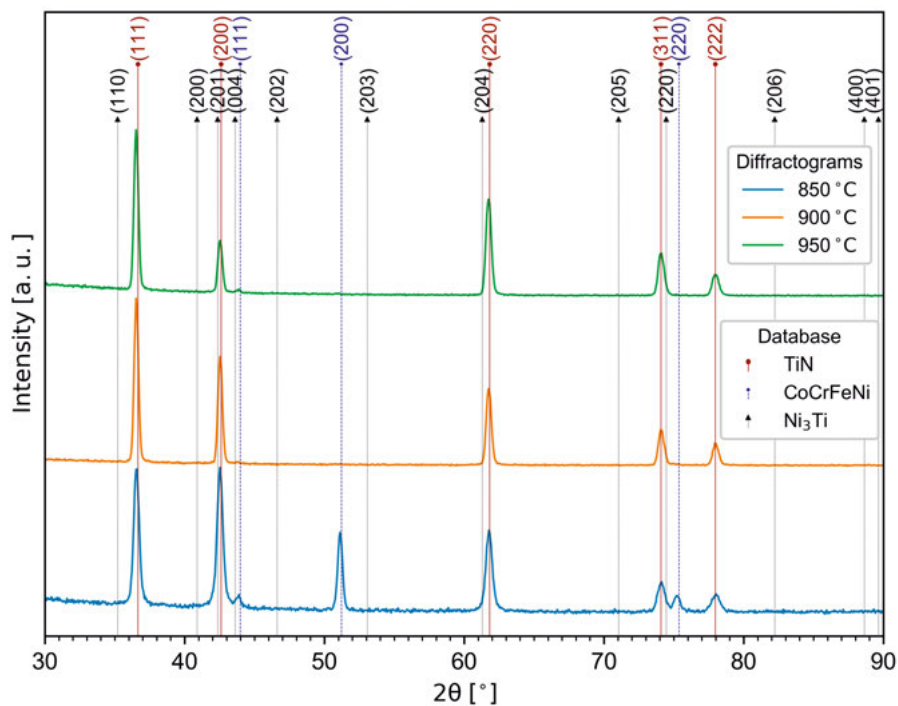


Figure 5.2. GI diffractograms of the TiN coatings deposited on a CoCrFeNi substrate. References: TiN: [97], CoCrFeNi: [98], Ni_3Ti : [99]. Adapted from Paper I.

The SEM top surface and STEM HAADF cross-section images also indicated that the coating growth was not disturbed by severe substrate etching or an intermetallic phase formation (Fig. 5.1, 5.3.a). The grain morphology was similar to morphologies obtained on pure Co, cemented carbide or graphite substrates [15, 100–102].

Thermodynamic calculations were carried out to investigate the condensed phases that can be formed besides TiN and CoCrFeNi. The metallic elements were included in equal amounts, the total pressure was kept constant at 10^5 Pa and the H/N molar ratio and the temperature were stepped. The calculations indicated that Cr can form chromium nitrides or ternary $\text{Cr}_{1-x}\text{Ti}_x\text{N}$ or $\text{Ti}_{1-x}\text{Cr}_x\text{N}$ ($x < 0.5$), depending on the temperature and the H/N molar ratio, by reacting with the coating or N_2 at the substrate surface. Chromium was detected in the grain boundaries of the coating deposited at 950°C , which was investigated by EDS in STEM (Fig. 5.3.b–f). This was an evidence of a probable Cr diffusion in the grain boundaries with a driving force of nitride formation with N_2 in the gas phase and the TiN coating. The growth of the coating was not disturbed by the grain boundary diffusion of Cr and the coating growth was columnar as was expected for TiN deposition under the applied conditions (Fig. 5.3).

The conclusion of the study is that CoCrFeNi can be coated with TiN using TiCl_4 , H_2 and N_2 precursors in thermally activated CVD and only Cr is slightly reactive in the process. Chromium, however, only appears in the coating grain boundaries. It would be interesting to investigate how the mechanical properties of the coating and the CVD of a next coating layer are influenced by Cr in the TiN grain boundaries and on the top surface.

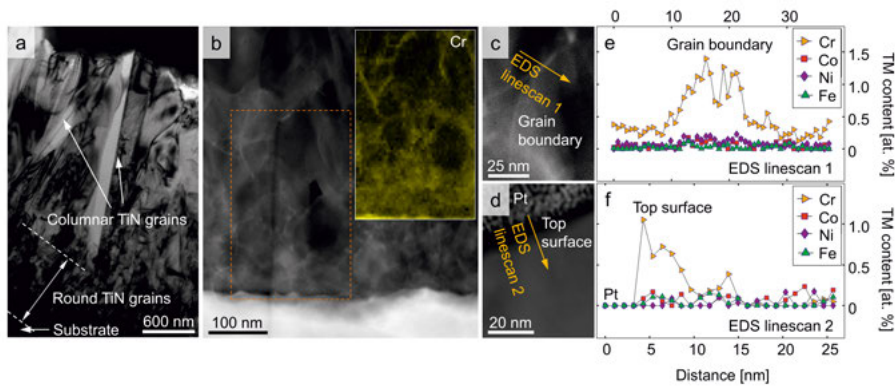


Figure 5.3. TEM characterization of the TiN coating deposited on a CoCrFeNi substrate at 950 °C. a) TEM BF image showing the grain morphology. b) HAADF STEM image with an inset showing the Cr distribution in the marked area, based on EDS data. a) and d) are HAADF STEM images e) and f) are the respective line profiles at a grain boundary and at the top surface, respectively. The concentrations in e) and f) are related to the total TM content. Adapted from Paper I.

5.2 CVD of W(C,N): The process window

To deposit W(C,N) coatings, first a process window needed to be determined as described in Paper II. The criterion for a process to fall inside the window was that a W(C,N) coating with a hexagonal δ -WC type structure and a columnar microstructure can be deposited in the process. The deposition temperature and the precursor partial pressures were varied, while the total pressure was kept constant at 133 Pa (1 Torr). Ar was used as a carrier gas and to balance the total flow rate at the gas inlet to 350 SCCM. After each process a H₂ flushing step was carried out for 5 minutes to reduce unwanted reaction products. The experimental parameters used for the process window determination are listed in Table 5.2 and the last column of the table indicates if the processes fell inside the process window.

Table 5.2. Experimental parameters for the deposition of W(C,N) coatings used in the investigation of the process window and reaction kinetics, described in sections 5.2 and 5.3

T [°C]	p(WF ₆) [Pa]	p(H ₂) [Pa]	p(CH ₃ CN) [Pa]	Deposition time	Coating thickness [μm]	Process window
Temperature series						
615	2.4	34	1.6	3 h 30 min	n/a	No
665	2.4	34	1.6	7 h 30 min	2.4	Yes
690	2.4	34	1.6	4 h	1.6	Yes
715	2.4	34	1.6	4 h	2.1	Yes
765	2.4	34	1.6	2 h	1.8	Yes
810	2.4	34	1.6	1 h 45 min	2.0	Yes
835	2.4	34	1.6	1 h 10 min	0.6	No
WF₆ series						
715	1.0	34	1.6	3 h	2.5	Yes
715	2.4	34	1.6	4 h	2.1	Yes
715	5.0	34	1.6	6 h	2.2	Yes
H₂ series						
715	2.4	17	1.6	8 h 30 min	2.0	Yes
715	2.4	34	1.6	4 h	2.1	Yes
715	2.4	57	1.6	1 h 40 min	1.4	No
CH₃CN series						
715	2.4	34	1.6	4 h	2.1	Yes
715	2.4	34	4.0	4 h	2.1	Yes
715	2.4	34	6.3	4 h	2.2	Yes*
W deposition without CH₃CN						
715	2.4	34	-	2 h	6	n/a

*Significantly different but columnar microstructure

Results from SEM and EBSD were used to determine if the coatings fell within the process window. The results are shown in Figs. 5.5–5.9 grouped according to the sample series. For the process window determination only the microstructures and crystalline phases were considered, the texture information collected from EBSD will be discussed in section 5.4. The X-ray diffractograms for the process window determination are presented in Fig. 5.4.

The temperature was screened between 615 °C and 835 °C, according to Table 5.2. The process window was found to be between 665 °C and 810 °C. For these deposition temperatures the coatings consisted of the δ -WC phase and a columnar microstructure was indicated by the ridge-like top surfaces of the grains and the EBSD cross-section images (Figs. 5.4 and 5.5.b,c,f,g). For the X-ray diffractograms presented with a logarithmic scale to investigate the phase purity the reader is referred to Paper II. Besides the here discussed δ -WC type phase, the X-ray diffractograms in Paper II show an η -phase enrichment between the deposition temperatures of 765 °C and 810 °C with a

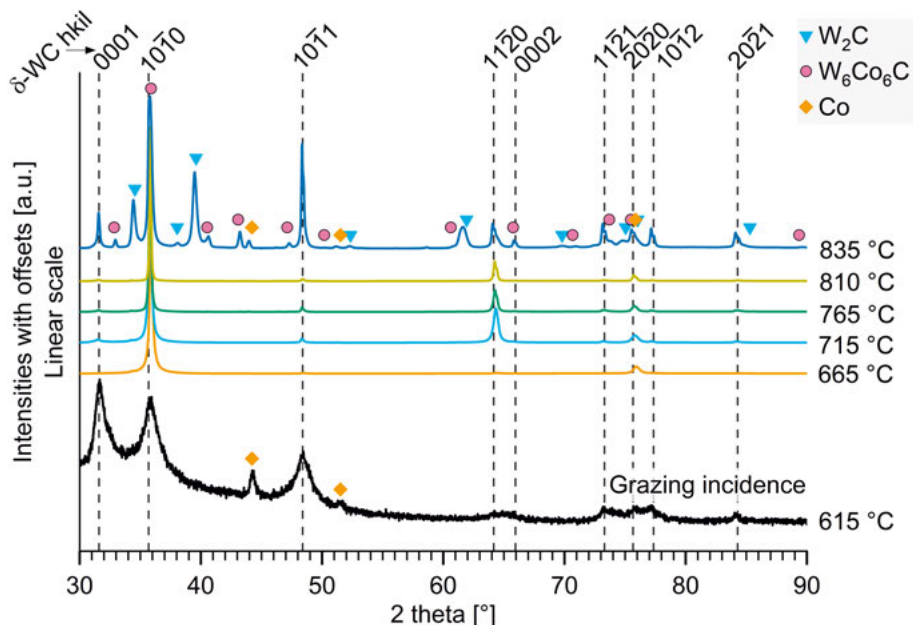


Figure 5.4. X-ray diffractograms of the samples in the temperature series. The intensities were normalized based on the heights of the peaks belonging to the $\{10\bar{1}0\}$ planes. References: W_2C : [103], W_6Co_6C : [104], Co: [105]. Adapted from Paper II.

very low intensity for the η -phase, indicating that it is only present at the substrate-to-coating interface.

The deposition temperature of 615 °C was outside the process window as an uneven coating with voids was formed as a result of a likely limited CH_3CN reactivity, see Fig. 5.5.a. GI-XRD was used for the phase analysis of this coating (Fig. 5.4), the coating consisted of the δ -WC type phase. The process carried out at 835 °C was also found to fall outside the process window, giving an upper temperature limit. A W-rich W_2C type phase was formed in addition to the δ -WC type phase (Fig. 5.4). The formation of the W-rich phase can probably be attributed to a relatively fast W incorporation rate at this temperature. At this temperature a binder phase (Co) enrichment occurred at the substrate-to-coating interface. The Co diffusion to the surface could be the result of the low pressure and high temperature during the reactor heating (Fig. 5.5.h). Furthermore, W_6Co_6C low-carbon η -phase formation occurred (Fig. 5.4), which could be explained with a fast W incorporation rate as well.

The influence of the precursor partial pressures on the resulting coatings was investigated at 715 °C. WF_6 and CH_3CN precursors were used in similar amounts (partial pressures of 1.0–5.0 Pa and 1.6–6.3 Pa, respectively) and H_2 was used at excess partial pressures (17–57 Pa). Three different partial pressures were used for each precursor, by varying one precursor at a time.

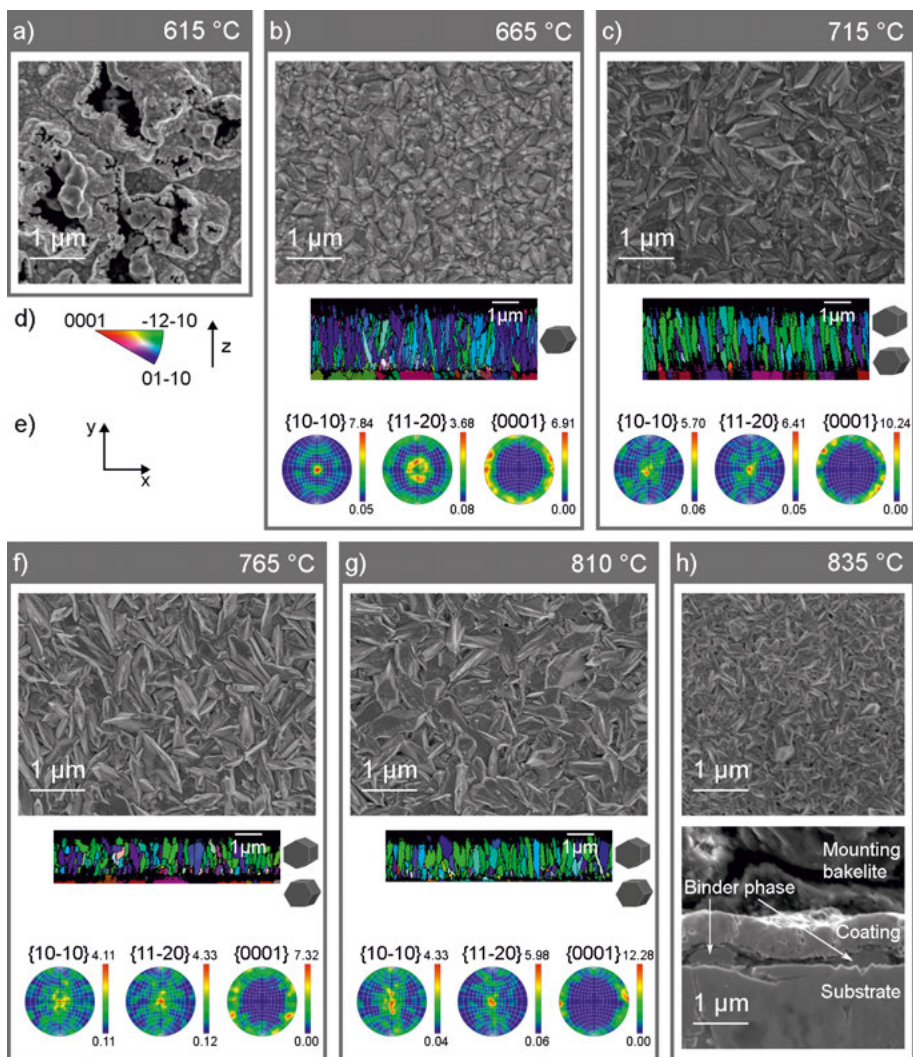


Figure 5.5. SEM and EBSD results for the samples in the temperature series. Coating top-view in-lens SEM images, EBSD cross-section maps with IPF coloring and EBSD pole figures for each sample where applicable. The hexagonal prisms besides the maps illustrate the preferred orientations. The color key and the z-direction for the IPF maps are indicated in d), the pole figure coordinates in e). In h) an SEM in-lens cross-section image is shown below the top-view image. Adapted from Paper II.

The resulting three sample series are each denoted with the name of the varied precursor (Table 5.2).

The processes with varied WF_6 partial pressures were all found to fall within the process window (Figs. 5.6, 5.7).

For H_2 an upper process limit was found at $p(\text{H}_2)=57$ Pa. Such a high H_2 partial pressure resulted in the formation of W-rich phases (WC_{1-x} and W_2C) and an under-dense microstructure (Figs. 5.6, 5.8.c). The latter is also supported by the polished cross-section of the sample (Fig. 5.8.c).

The investigated processes in the CH_3CN series were all found to result in coatings of a δ -WC type phase (Fig. 5.6). A high CH_3CN partial pressure, however, resulted in a changed microstructure (Fig. 5.9.c). The microstructure varied slightly as the process was repeated and the diffractograms and SEM images of two samples (A and B) from two processes are shown; the variations are discussed below in section 5.4. The major part of the coating could not be indexed in EBSD.

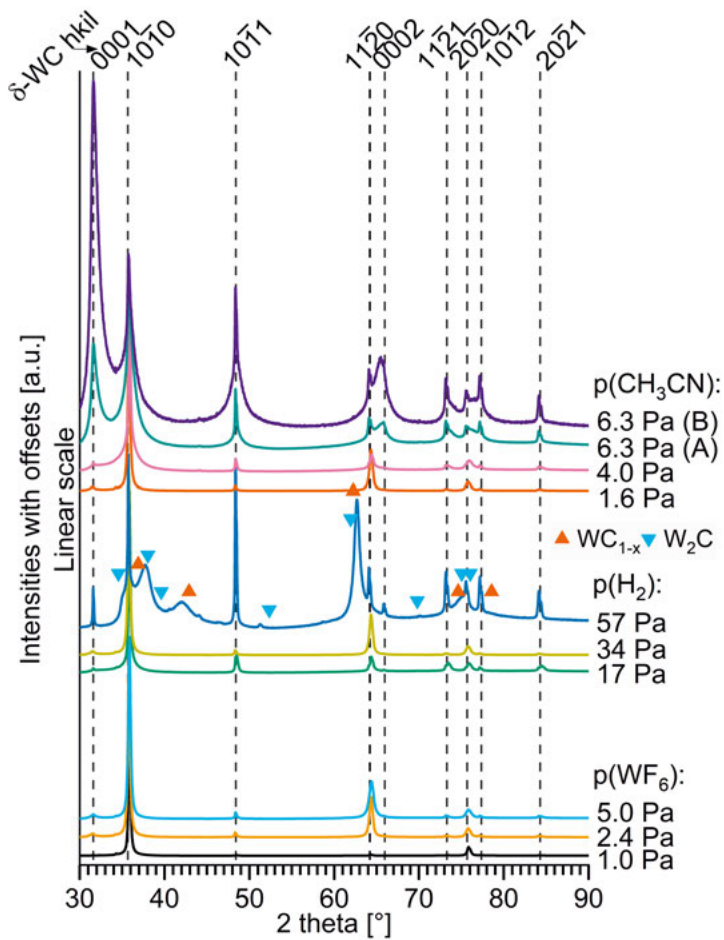


Figure 5.6. X-ray diffractograms of the samples in the different precursor series. The intensities were normalized based on the heights of the peaks belonging to the $\{10\bar{1}0\}$ planes. References: W_2C : [103], WC_{1-x} : [106]. Adapted from Paper II.

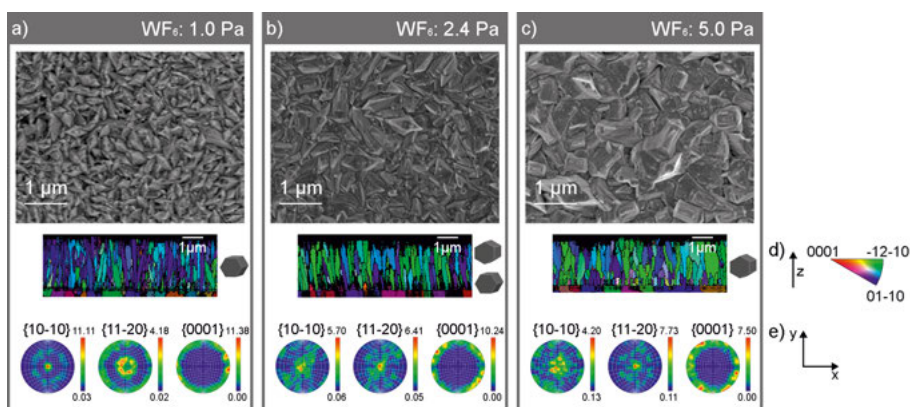


Figure 5.7. SEM and EBSD results for the samples in the WF_6 series. Coating top-view in-lens SEM images, EBSD cross-section maps with IPF coloring and EBSD pole figures for each sample. The hexagonal prisms besides the maps illustrate the preferred orientations. The color key and the z-direction for the IPF maps are indicated in d), the pole figure coordinates in e). Adapted from Paper II.

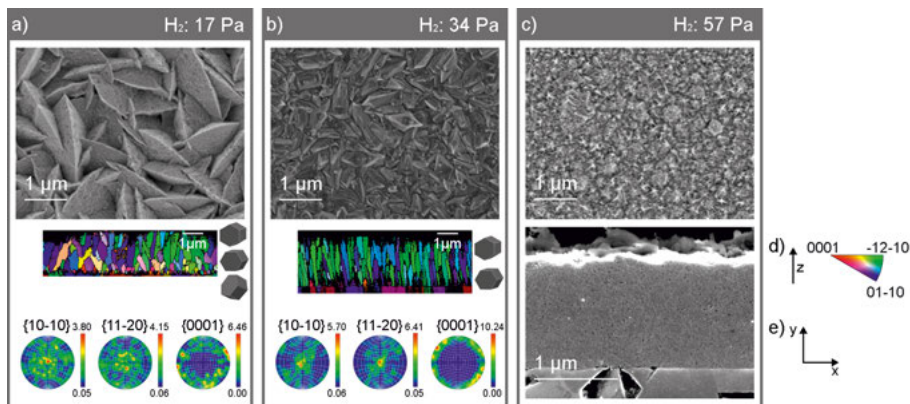


Figure 5.8. SEM and EBSD results for the samples in the H_2 series. Coating top-view in-lens SEM images, cross-section EBSD maps with IPF coloring and EBSD pole figures for each sample where applicable. The hexagonal prisms besides the maps illustrate the preferred orientations. The color key and the z-direction for the IPF maps are indicated in d), the pole figure coordinates in e). In h) an SEM in-lens cross-section image is shown below the top-view image. An image at a larger magnification of the cross-section is shown in the Supplementary material of Paper II. Adapted from Paper II.

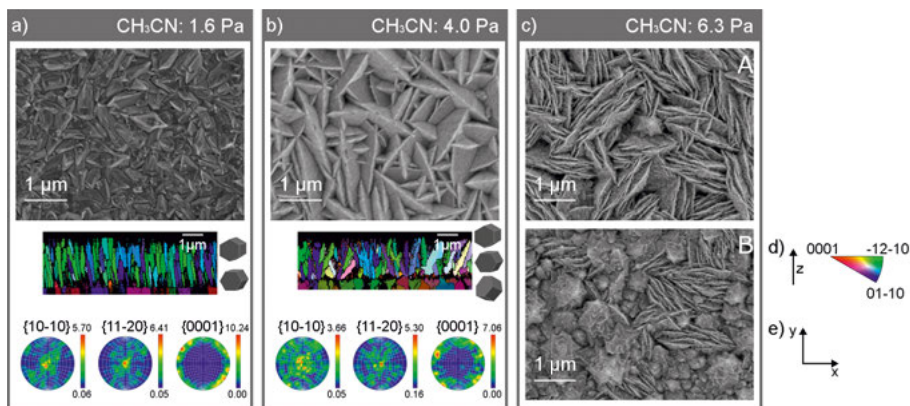


Figure 5.9. SEM and EBSD results for the samples in the CH₃CN series. Coating top-view in-lens SEM images, cross-section EBSD maps with IPF coloring and EBSD pole figures for each sample where applicable. The hexagonal prisms besides the maps illustrate the preferred orientations. c) Top-view images of two coatings (A and B) deposited at p(CH₃CN)=6.3 Pa in two separate processes. The color key and the z-direction for the IPF maps are indicated in d), the pole figure coordinates in e). Adapted from Paper II.

5.3 Kinetics of W(C,N) deposition and the current understanding of the reaction mechanism

The deposition kinetics of W(C,N) coatings was investigated in Paper II. The deposition rates were calculated from the coating thicknesses from SEM cross-section images, stated in Table 5.2. An Arrhenius-plot was prepared for the coatings deposited between 665 °C and 835 °C (Fig. 5.10.a). The plot was linear between 665 °C and 810 °C and an activation energy of 77 kJ/mol was calculated. The deposition rate dropped at 835 °C along with a change in phase composition and a reaction with the substrate shown in Fig. 5.5.h. For a deposition at 715 °C in the temperature series an additional sample 10 cm further down stream from the standard sample position in the reactor was analyzed. The deposition rate was found to be similar at the downstream position, indicating that the precursors were not depleted within that distance in the reactor. Furthermore, the coating thickness at the standard position was investigated at all four vertical sides of the substrate in addition to the top surface and an even deposition rate was observed. The latter observations on the coating conformality and the length of the deposition zone together with a linear Arrhenius curve indicated that the process was kinetics controlled within the process window (665–810 °C).

The log-log plots of the coatings are shown in Fig. 5.10.b–d, where all the depositions were included. WF₆ had a negative reaction order (-0.6) and H₂ had a reaction order of 1. These indicated that the reaction rate was strongly dependent on the incorporation rate of W into the coatings, where H₂ acted as

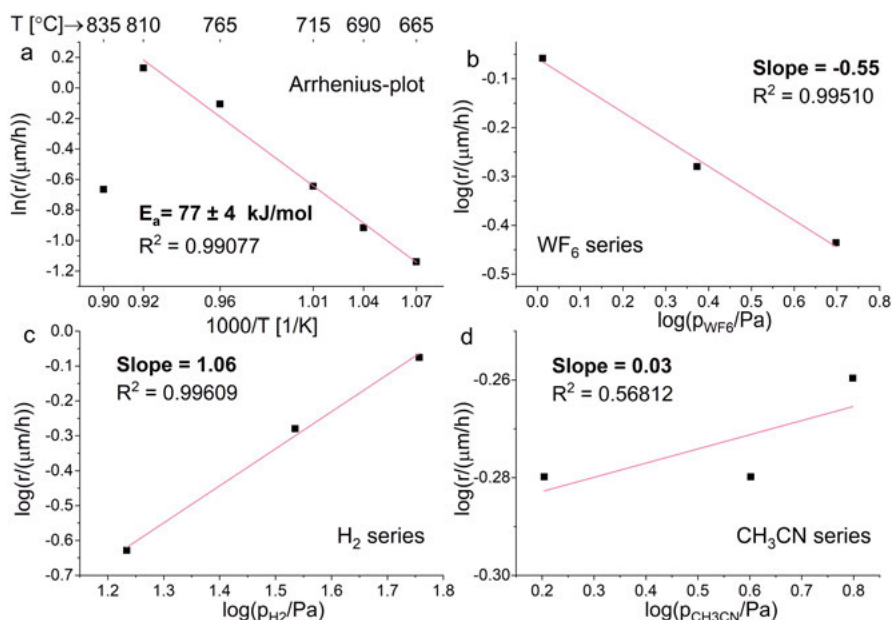


Figure 5.10. a) Arrhenius plot of the temperature series ranging from 665 °C to 835 °C. b–d) log–log plots of the reaction rate dependence on the partial pressures of WF_6 , H_2 and CH_3CN , respectively. Adapted from Paper II.

a reducing agent and probably as a scavenger of F species from the surface. A proposed explanation for the negative reaction order of WF_6 is that F species poisoned the surface and slowed down the deposition. A similar phenomenon was described in [107] for W deposition at a low H_2/WF_6 ratio. CH_3CN did not change the deposition rate within the investigated partial pressure range. It had, however, a strong influence on the coating microstructure as discussed below in section 5.4. CH_3CN , however, slowed down the deposition compared to the deposition of pure W without CH_3CN , using only WF_6 and H_2 precursors at similar deposition conditions, shown in Table 5.2 (W deposition without CH_3CN). The W deposition rate was 3 $\mu\text{m/h}$, when adding CH_3CN to the reaction gas mixture of WF_6 and H_2 , the reaction rate decreased to 0.5 $\mu\text{m/h}$. CH_3CN probably slowed down the deposition by occupying surface sites or its derivatives acting the same way.

The decomposition mechanism of CH_3CN is currently not known. HCN was previously determined as the main growth species for C and N incorporation in $\text{Ti}(\text{C},\text{N})$ CVD from TiCl_4 , CH_3CN , N_2 and H_2 , based on thermodynamic calculations combined with experimental kinetic investigations [39]. CH_4 was the most stable C-containing species [39]. If the methyl group of CH_3CN is converted to CH_4 in the gas phase as a result of a reaction with H_2 , it is unlikely that the stable CH_4 molecule is a C-source in the $\text{W}(\text{C},\text{N})$ depo-

sitions at temperatures lower than 835°C, which were applied in this thesis. Carbon incorporation from CH₄ was reported to only be possible at temperatures over 950 °C in the CVD of TiC [108], but the reaction kinetics might be different on a different surface during the W(C,N) deposition. Adsorption and decomposition studies of HCN and CH₃CN on a WC (0001)-like surface were carried out at elevated temperatures under ultra high vacuum conditions [109–111]. Based on these studies it is likely that CH₃CN or HCN, when reaching the surface, decompose to adsorbed C and N, and to some extent N atoms recombine to N₂ at higher deposition temperatures, in [111] N₂ formation was reported over 830 °C. It should further be noted that the type of surface is decisive on the mechanisms and activation energies of the competing desorption and irreversible decomposition processes, as was shown in comparisons between the W(100) and the WC (0001)-like surfaces [109, 110].

5.4 The growth, microstructure and texture of W(C,N)

5.4.1 Columnar growth with a ridge-like top surface

The growth and microstructure of the W(C,N) coatings is discussed in Papers II and III. The top morphology and microstructure of the coatings is shown in SEM images and EBSD IPF maps in Figs. 5.5 and 5.7–5.9. In general, the majority of the coatings grew with a columnar microstructure, which could be deduced from the EBSD cross-section maps. The grains that grew throughout the coating nucleated close to the substrate surface and did not have an epitaxial relation to the underlying WC grains in the substrate as shown by the coloring in the EBSD IPF maps. These maps and the pole figures indicated a primarily prismatic coating texture. SEM images showed that the top surface of the columnar grains was ridge-like. The coatings with a different microstructure from the typical columnar are discussed in more detail in Section 5.4.2.

Three coatings with prismatic texture and ridge-like top surface but different morphologies were investigated using STEM (Paper III). The coatings deposited at T=715 °C in the temperature series, at p(WF₆)=1.0 Pa in the WF₆ series and at p(H₂)=17 Pa in the H₂ series were characterized (Table 5.2). These samples are later denoted as S1–S3 in Section 5.5 (Table 5.3) and Section 5.6. The aim of the investigation was to explain how the growth, the ridge-like morphology and the prismatic texture are related.

Figures 5.5.c, 5.7.a and 5.8.a show the surface morphologies and cross-section EBSD maps of the coatings. The cross-section STEM BF images of these coatings are shown in Fig. 5.11.a–c. The diffraction contrast in Fig. 5.11.a–c revealed a defect line at the center of the grains as seen in Fig. 5.11.a–c and highlighted in Fig. 5.12. The defect lines extended from the base of the grains to the ridges. High resolution STEM (HR STEM) imaging at these central defect lines showed that the defect lines were stacking faults in the

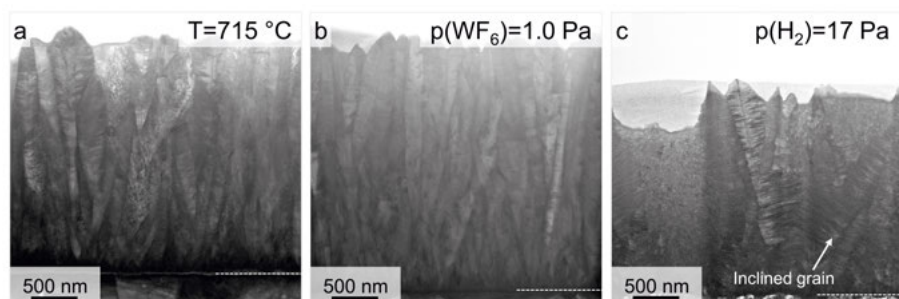
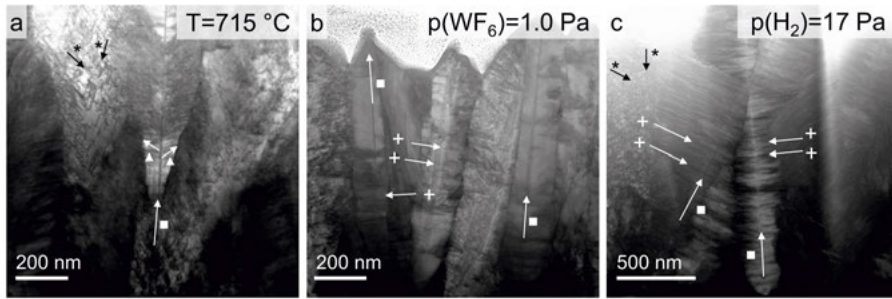


Figure 5.11. STEM BF images of the cross-sections of three selected coatings: the coating deposited at a) 715 °C in the temperature series, at b) $p(\text{WF}_6)=1.0$ Pa in the WF_6 series and at c) $p(\text{H}_2)=17$ Pa in the H_2 series. A horizontal dashed line indicates the substrate-to-coating interface for all samples. Adapted from Paper III.

stacking of the c-planes, see the crystallographic directions in Fig. 5.13.a. From the prismatic texture it was already known that the c-planes were parallel to the growth direction and the STEM investigation also revealed that the c-planes were parallel to the grain ridges. An EBSD map confirmed that the c-planes were parallel to the ridges (Fig. 5.14). The map was recorded on the polished top surface of a coating deposited at $p(\text{H}_2)=17$ Pa in the H_2 series, having grains with the highest aspect ratio and the ridges being parallel to the major diameter of the grains on the top surface (Fig. 5.8.a). The c-planes being parallel to the horizontal major diameter of the grains and the growth direction indicates that the grains grew slower in the $\langle 0001 \rangle$ direction than in the prismatic directions.

At the central stacking faults, the stacking of the close packed W planes in the hexagonal simple packed metallic lattice of the δ -WC type structure shifted from the ...AA... stacking, the planes that are not aligned with the A planes are denoted as B (Fig. 5.13.a–c). It was proposed that the growth could have initiated and progressed fastest at stacking faults and the grains developed by material addition on the two sides of these central part, resulting in ridges.

High resolution images of defects perpendicular to the grain growth direction are shown in Fig. 5.13.d,e. These defects were locally limited to a small volume and at the edges of the defects the atoms were aligned with the neighboring planes again. Apart from the mentioned defects, a high density of defects was detected along the $[0001]$ zone axis, the grains of the analyzed coating consisted of defect-free domains of an approximate 5 nm diameter only (Fig. 5.15). The stacking of the $\{10\bar{1}0\}$ planes changed from a ...XY... to a ...YY... stacking at these defects, these stacking faults formed the boundaries of the domains. These defects corresponded to the defect lines at an angle of 60° in Fig. 5.12.c. Further defects were observed in the form of curved lines at a 45° angle, which were probably dislocation lines (Fig. 5.12.a).



*Figure 5.12. STEM BF images of coating cross-sections revealing defects by diffraction contrast. The types of the defects are indicated with symbols, ■: defects parallel to the grain growth direction, +: defects perpendicular to the grain growth direction, *: defects at a 60° relative angle, ▲: defects at a 45° angle from the grain growth direction. The coatings are denoted with their deposition parameters and are the same coatings as in Fig. 5.11. Adapted from Paper III.*

5.4.2 Microstructure and texture variations related to the process parameters

The orientation and the size of the coating grains varied as a function of the process parameters. In general, a wider grain orientation distribution positively correlated with a larger grain size. The results on the grain size and texture are summarized in Fig. 5.16, where the process window is also indicated. In Fig. 5.16 only the highest texture coefficients are shown for each coating. Seven reflections were used: the ones belonging to the $\{0001\}$, $\{10\bar{1}0\}$, $\{10\bar{1}1\}$, $\{11\bar{2}0\}$, $\{11\bar{2}1\}$, $\{10\bar{1}2\}$ and the $\{2021\}$ planes and therefore the highest possible texture coefficient is 7. The intensities were taken from the Pearson's database based on [112]. All the texture coefficients are presented in Paper II. The grain sizes for the trends shown in Fig. 5.16 were deduced from the SEM top images (Figs. 5.5–5.9) and the EBSD data — from the minor diameters of the ellipses fitted to the grains; the values are found in Paper II.

Temperature

At the lowest possible deposition temperature within the process window, 665 °C, the coating had narrow grains (approximately 200 nm in diameter) and a strictly $\{10\bar{1}0\}$ texture. At a higher temperature, the grains were larger together with a mixed prismatic $\{10\bar{1}0\}$ and $\{11\bar{2}0\}$ texture with a preference for the $\{11\bar{2}0\}$ orientation (Figs. 5.5 and 5.16.a). In general, a larger surface mobility of the adspecies in relation to the overall growth rate is believed to result in larger grains. A larger grain size could be a result of a larger surface mobility of the adspecies due to a higher temperature, although the overall growth rate increased as well (Fig. 5.10.a).

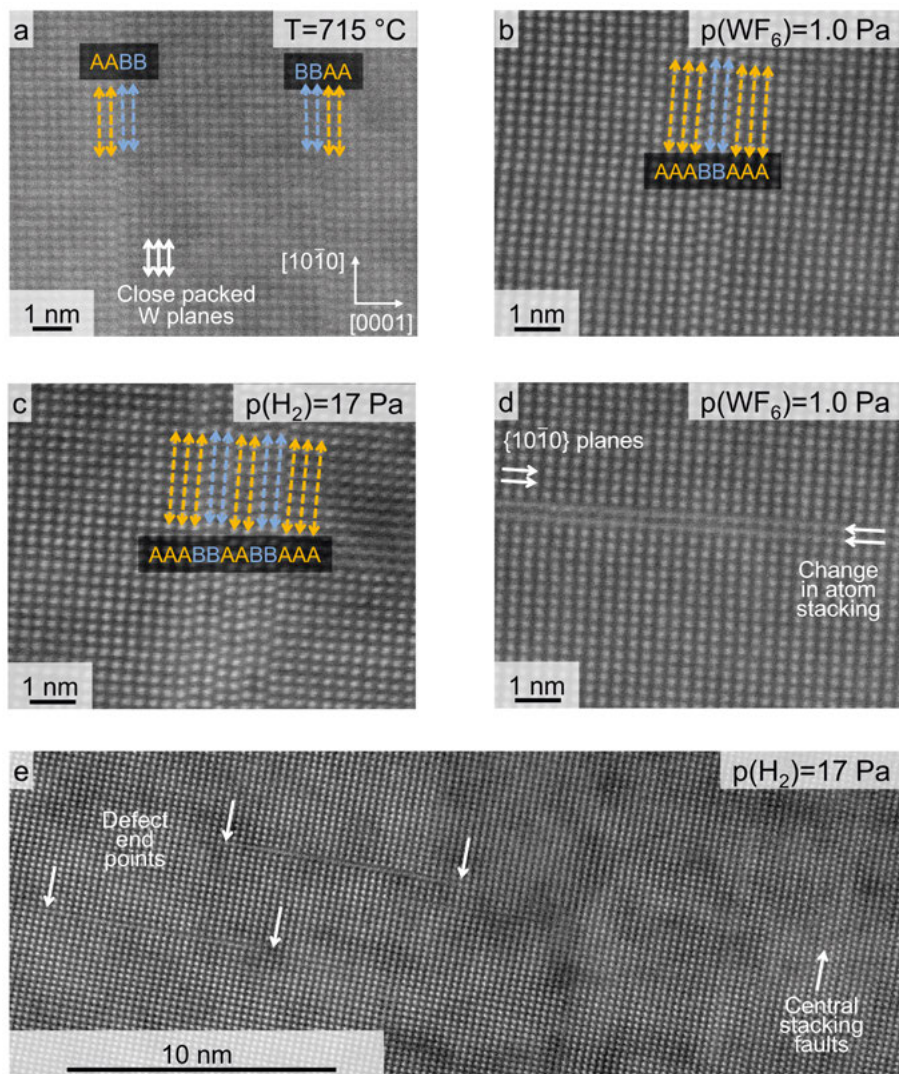


Figure 5.13. High resolution STEM HAADF images showing the typical defects in the coatings that are detectable along the $[\bar{1}2\bar{1}0]$ zone axis. In a–c) A and B denote the close packed planes of the hsp W lattice. a) also shows the crystallographic directions valid for all images, calculated from the fast Fourier transformed (FFT) image. d) and e) show defects perpendicular to the grain growth direction and arrows indicate the end points of the defects. The coatings are denoted with their deposition parameters and are the same coatings as in Fig. 5.11. Adapted from Paper III.



Figure 5.14. Top-view EBSD IPF map of the polished coating deposited at $p(\text{H}_2)=17$ Pa in the H_2 series, with indication of the grain orientations. Adapted from Paper III.

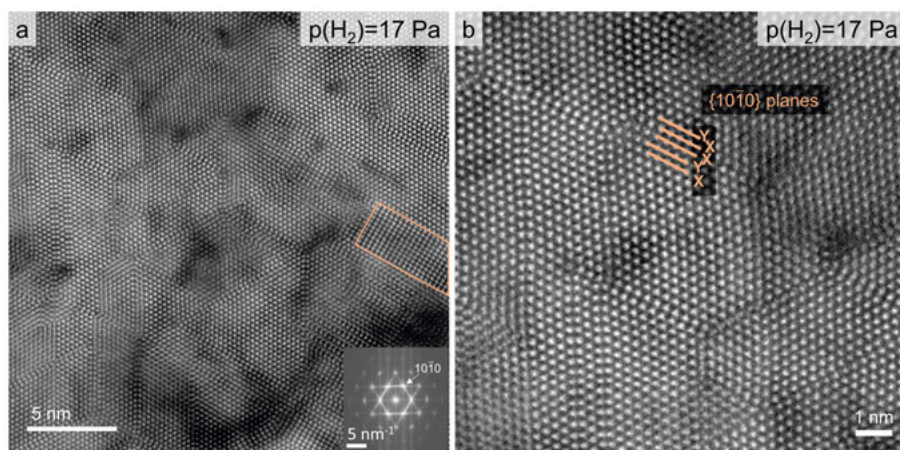


Figure 5.15. High resolution STEM HAADF images along the $[0001]$ zone axis of the coating deposited at $p(\text{H}_2)=17$ Pa in the H_2 series. A high density of stacking faults is shown in a) and the highlighted area shows an example where a different stacking of the planes stabilizes and results in a small coating volume with a different crystal structure. The inset of a) shows the FFT of the recorded image. b) highlights how the stacking of the $\{10\bar{1}0\}$ planes shifts. Adapted from Paper III.

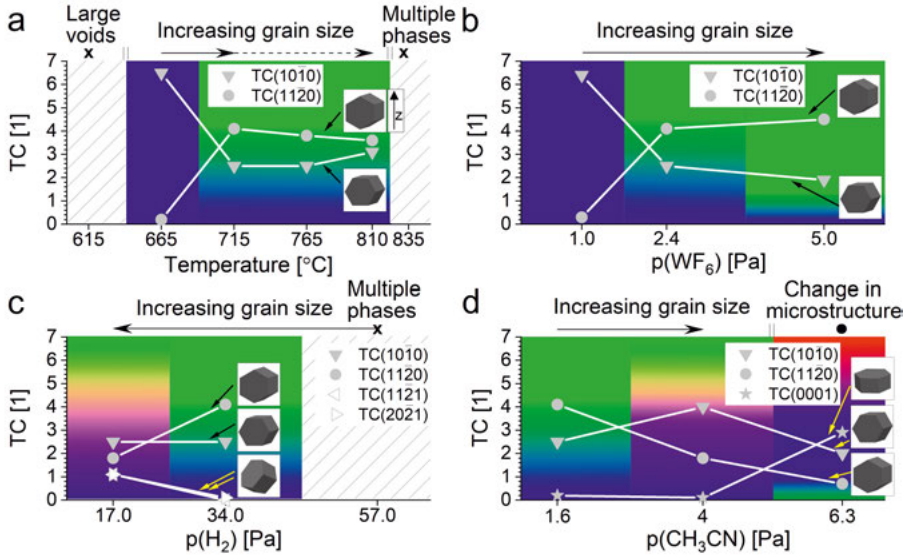


Figure 5.16. Summary of the W(C,N) coating texture as a function of the process parameters: a) deposition temperature, b) $p(\text{WF}_6)$, c) $p(\text{H}_2)$ and d) $p(\text{CH}_3\text{CN})$. In all subfigures the evolution of the most important texture coefficients are shown. The shaded areas qualitatively describe the texture evolution as deduced from the XRD and EBSD results and are related to the EBSD coloring (blue: $\{10\bar{1}0\}$, green $\{11\bar{2}0\}$, red: $\{0001\}$, purple and orange: pyramidal planes). The hexagonal prisms in the insets symbolize the orientations related to the growth direction (denoted as z in a)). In the upper part of each subfigure the grain size evolution is shown. An x at the top indicates a significant change in phase composition or microstructure, a limit of the process window. A • indicates a significant change in the coating microstructure within the process window. Adapted from Paper II.

WF₆ and H₂ partial pressures

The lowest $p(\text{WF}_6)$ also resulted in narrow grains and a strictly $\{10\bar{1}0\}$ texture (Fig. 5.16.b). An increased WF_6 partial pressure yielded a mixed prismatic texture with increasing contribution from the $\{11\bar{2}0\}$ orientation, parallel with an increasing grain size. The overall growth rate decreased as the WF_6 partial pressure increased (Fig. 5.10.b), which could partially explain an increased grain size, even though F species on the surface could have slowed down the surface diffusion at the same time.

The trend observed with the increase of the $p(\text{H}_2)$ (Fig. 5.16.c) could be explained based on similar principles. A lower growth rate at a lower $p(\text{H}_2)$ resulted in larger grains. At the lowest studied $p(\text{H}_2)$, the orientation of a significant proportion of grains was tilted from the prismatic. This was indicated by a wider intensity distribution in the EBSD pole figures than for a higher $p(\text{H}_2)$ (Fig. 5.8.a,b) and by two pyramidal texture coefficients that were close to 1 (and lower than 0.3 for other prismatic coatings), these TCs are included in Fig. 5.16.c. In the cross-section STEM image of this coating, a central defect line that was inclined from the substrate normal was observed for some grains, indicating that the grain growth direction deviated from the substrate normal direction (Fig. 5.11.c). The highest studied $p(\text{H}_2)=57$ Pa resulted in small grains, following the grain size trend (Fig. 5.8.a.), but also in a too rapid W incorporation rate, resulting in W-rich phases (Fig. 5.6), i.e. the process fell outside the process window (Fig. 5.16.c).

CH₃CN partial pressure

The trends for the CH_3CN partial pressure are more difficult to explain. The partial pressure of CH_3CN did not influence the deposition rate in the studied partial pressure range, but it had a significant influence on the microstructure. It probably influenced the growth by blocking surface sites and slowing down surface diffusion of the adspecies. Blocking of surface sites by C-species was proposed in [58]. This resulted in an increased grain size first (at $p(\text{CH}_3\text{CN})=4.0$ Pa), which could be the result of the slower surface diffusion but an unchanged overall growth rate (Figs. 5.9.b and 5.16.c). The texture was partially tilted prismatic in this case as well, indicated by the EBSD pole figures in Fig. 5.9.b. Some pyramidal texture coefficients were slightly higher than for the prismatic samples (see Paper II), but not as significantly as for $p(\text{H}_2)=17$ Pa. A further increase in the CH_3CN partial pressure considerably changed the microstructure. Two domains were observed, one with a star-like and one with a ridge-like top surface where the ridges were clustered in a hay-like manner (Fig. 5.9.c). As mentioned in section 5.2, the relative amounts of the two domains varied and by a comparison of the two X-ray diffractograms (Fig. 5.6) against the SEM images (Fig. 5.9.c) of two samples, it was deduced that the star-like domains had a dominantly basal ($\{0001\}$) texture and the ridge-like domains had a prismatic texture. SAED in TEM confirmed the preferred orientation of the two domains (Fig. 5.17). Fig. 5.17.a shows a STEM

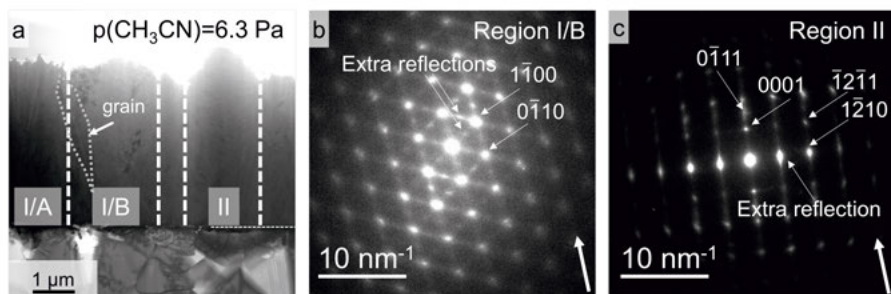


Figure 5.17. a) STEM BF image of the cross-section of the coating deposited at $p(\text{CH}_3\text{CN})=6.3$ Pa in the CH_3CN series. Regions I/A and I/B belong to ridge-like domains, in region I/A with ridges perpendicular to, in region I/B with ridges parallel to the image plane. Region II belongs to a star-like domain. A grain that is similar in morphology to the grains of prismatic coatings in Fig. 5.11 is also marked with a dotted line. Indexed SAED patterns from b) region I/B and c) region II with arrows indicating the substrate surface normal direction. The zone axis in b) is $[0001]$ and in c) is $[10\bar{1}0]$. Adapted from Paper III.

BF image of the coating cross-section. In the figure regions I/A and I/B are from ridge-like domains, in I/A the ridges are perpendicular to, in I/B they are parallel with the image plane. Region II belongs to a star-like domain. The diffraction patterns in Fig. 5.17.b,c from regions I/B and II, respectively confirm a prismatic texture for the ridge-like and a basal texture for the star-like domains. The two domains and the diffraction patterns are discussed in more detail in Paper III. The sharp edges of the star-like features (Fig. 5.9.c) were probably an indication that the growth in one of the prismatic directions was still preferred, but in an in-plane direction.

On the orientation distribution in general

The orientation distribution of the coatings was investigated by rocking curve measurements, the curves obtained after the corrections described in section 3.1 are shown in Fig. 5.18. In general, the orientation distribution was wide, being the narrowest for the $\{10\bar{1}0\}$ textured coatings ($T=665$ °C in the temperature series and $p(\text{WF}_6)=1.0$ Pa in the WF_6 series). The corresponding rocking curves had a full width at half maximum of approximately 20° (Fig. 5.18.a,b). The trends in the widths of the curves in the different series followed the earlier described trends, i.e. a wider texture distribution was observed as the deposition temperature, $p(\text{WF}_6)$ or $p(\text{CH}_3\text{CN})$ was increased or the $p(\text{H}_2)$ was decreased in the deposition process.

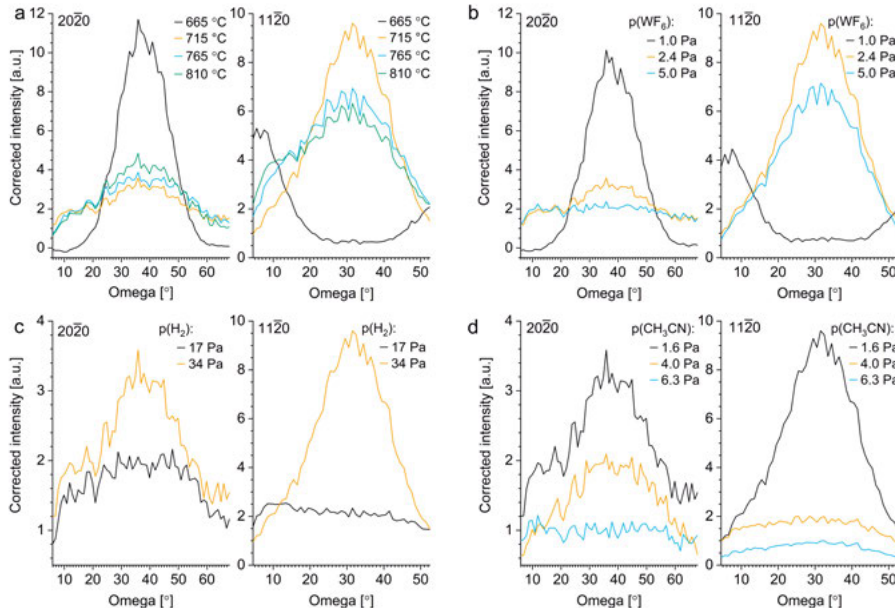


Figure 5.18. Rocking curves of the coatings in the different sample series: a) temperature, b) WF_6 c) H_2 and d) CH_3CN . The intensities are expressed in arbitrary units, but are comparable for the different samples. Note that instead of the reflections belonging to the $\{10\bar{1}0\}$ planes the reflections of the $\{20\bar{2}0\}$ planes were measured to enable a wider scanning range.

5.4.3 Microstructure and texture — a comparison with other ceramic coatings

There are similarities between the CVD growth of the W(C,N) coatings with a δ -WC type structure and other, cubic (NaCl type) and hexagonal (AlB_2 type) ceramic coatings. The metallic lattice in the δ -WC type and AlB_2 type structures is hexagonal simple packed (hsp) and in the NaCl type structure it is cubic close packed (ccp). The difference between the hsp and ccp lattices is the stacking of the close packed planes, the sequence is ...AA... and ...ABC..., respectively, a comparison is shown in Fig. 5.19.b.

When the texture is prismatic in case of the hexagonal systems, the close packed planes are parallel to the substrate surface normal. The orientations of the close packed planes relative to the substrate normal for the two main prismatic textures are shown in Fig. 5.19.a. In case of the $\{10\bar{1}0\}$ and $\{11\bar{2}0\}$ textures the $\langle 10\bar{1}0 \rangle$ and $\langle 11\bar{2}0 \rangle$ directions are parallel to the substrate surface normal. These directions are respectively related to the $\langle 211 \rangle$ and $\langle 110 \rangle$ directions in the ccp lattice if only the metallic close packed planes are considered. The $\langle 211 \rangle$ texture is common for the growth of NaCl structured transition metal carbides, nitrides and carbonitrides when a twin is formed at the $\{111\}$ plane [102, 113–115]. At the apparent defect lines parallel to the growth direction observed for the W(C,N) coatings (Fig. 5.13.a–c) the stacking of the close packed planes changes, similarly to the formation of a twin in the NaCl type materials. In TiN growth $\langle 110 \rangle$ texture (similar to the $\langle 11\bar{2}0 \rangle$ texture) is commonly observed when multiple twins occur within one grain [100, 102].

An example of an AlB_2 structured material for which the dependence of the texture on the CVD process parameters was studied is hafnium diboride (HfB_2) deposited from a $\text{Hf}(\text{BH}_4)_4$ precursor [116]. Similarly to the W(C,N) coatings, a prismatic texture and a slow growth in the $\langle 0001 \rangle$ direction was observed over 800 °C. The microstructure was platelet like similar to the W(C,N) grain ridges, except the grains were much narrower for HfB_2 . At lower deposition temperatures, where the mobility of the adspecies was lower, the texture was basal and domains with a star-like top surface developed. The morphology was similar to the star-like domains of the W(C,N) coating that was deposited at a high $p(\text{CH}_3\text{CN})=6.3$ Pa, where the CH_3CN derivatives probably hindered the surface diffusion of the adspecies. $\{10\bar{1}0\}$ and $\{11\bar{2}0\}$ textures were also achieved by CVD of titanium diboride (TiB_2) [117].

A prismatic texture was also observed for W-based PVD coatings with a δ -WC type structure and therefore may not be related to a chemical process step [37, 38, 118, 119].

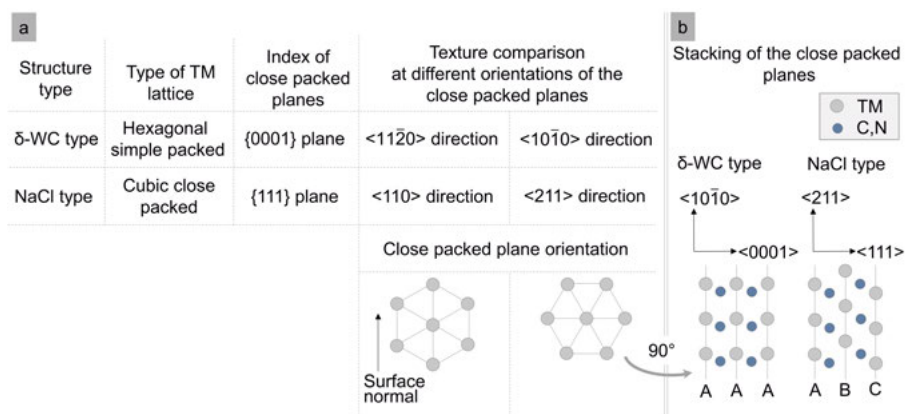


Figure 5.19. a) Comparison between crystallographic directions important for the texture of δ -WC type (hsp metallic lattice) and NaCl-type (ccp metallic lattice) structured coatings. b) The stacking of the close packed planes in the two structures, including the positions of the p-elements.

5.5 Elemental composition and spectroscopy of W(C,N)

As described in sections 3.5 and 3.6, the compositional and spectroscopic analysis of ceramic coatings containing both light (e.g. B, C, N) and heavy (e.g. Hf, Ta, W) elements is challenging. The elemental composition of the W(C,N) coatings was determined by ERDA in Paper II. The coatings appeared to be C- and N-rich according to ERDA, while the N/(C+N) ratio was stable around 0.3 for most of the coatings (for the detailed compositions see Paper II). The STEM characterization in section 5.4 and the XPS characterization below did not show the presence of free carbon and therefore the C- and N-rich composition (with a 20-80 % excess of the p-elements) could not be explained with the presence of a free carbon phase. An exact concentration determination of heavier elements in ERDA can be hindered by scattering events such as multiple scattering [79]. Therefore, for a more accurate determination of the (C+N)/W ratio combined ERDA and relative RBS measurements were carried out for selected coatings. The selected W(C,N) coatings are listed in Table 5.3. The coatings were selected based on the process parameters, where S1 was deposited in a reference process, which was included in all deposition series in the process window investigation (Table 5.2). Coatings S2–S4 were deposited by varying one precursor partial pressure at a time relative to the deposition of S1. Additionally, a WC reference (called WC reference 1) was also included. The WC reference contained 6.15 ± 0.01 wt.% (50.1 at.%) carbon and maximum 0.02 wt.% free carbon, corresponding to a C/W ratio of 1.003 ± 0.002 and it had an average grain diameter of $2.38 \mu\text{m}$ (Fisher sieve size). The powder was pressed into In foil for the ERDA measurement (99.99 % trace metal basis; the carbon content of the foil was under the detection limit of ERDA).

The combined ERDA and relative RBS measurements of the W(C,N) coatings resulted in a (C+N)/W atomic ratio that was close to 1, as presented in Table 5.3. The atomic concentrations in ERDA showed a systematic error of approximately 20 %, with an overestimation of the light and an underestimation of the heavy element concentrations. These systematic errors propagated to an approximate 50 % systematic error in the relative atomic concentrations between the light and heavy elements determined by ERDA. The ERDA measurement on the stoichiometric WC powder confirmed that ERDA underestimates the W content relative to light elements, C in this case. The N/(C+N) ratio could only be determined from ERDA, which has a high accuracy for the determination of the relative concentrations of light elements [78]. It was also noted here that for some samples, the (C+N)/W atomic ratios determined by ERDA varied when a new batch of samples was measured compared to Paper II, which can depend on the ERDA measurements, but also variations in the CVD processes. The W(C,N) stoichiometry obtained from the combined ERDA and RBS measurements corresponds to what would be expected for a thermodynamically stable solid solution of the stoichiometric hexagonal δ -WC type phase WN and WC [49, 50]. The measurement on the WC reference also showed that ERDA overestimates the relative carbon content.

Table 5.3. Atomic ratios determined with the ion beam analysis techniques together with the synthesis parameters of the samples. The CVD processes were carried out at a total pressure of 133 Pa, $p(\text{Ar})=\text{balance}$.

Sample name	CVD process description	CVD process parameters or synthesis/treatment method				(C+N)/W from RBS	N/(C+N) from ERDA	(C+N)/W from ERDA
		T[°C]	p(WF ₆) [Pa]	p(H ₂) [Pa]	p(CH ₃ CN) [Pa]			
S1	Reference	715	2.4	34	1.6	1.0	0.3	1.5
S2	Low p(WF ₆)	715	1.0	34	1.6	1.0	0.3	1.4
S3	Low p(H ₂)	715	2.4	17	1.6	1.0	0.3	1.5
S4	High p(CH ₃ CN)	715	2.4	34	6.3	1.1	0.3	1.6
WC reference 1	n/a		W powder carbonation			n/a	n/a	1.3
WN _x reference	n/a	565	3.0	22	p(NH ₃)=17 Pa	1.0	n/a	1.5

HAXPES measurements were carried out for all the samples in Table 5.3, except that another WC reference was used, called WC reference 2. This WC powder contained 6.11 wt.% C (lower limit 6.08 wt.%, upper limit 6.18 wt.%, 0.02 wt.% free carbon, 0.18 wt.% O), with a grain size of 0.64 μm (Fisher sieve sizer). The aims of the measurements were to investigate the free carbon content of the samples and a chemical analysis of the coatings without the need for Ar⁺ etching. Two photon energies (2.3 keV and 8 keV) were used in order to obtain information from different probing depths.

Figure 5.20 shows core level spectra of C 1s, N 1s and W 4f of all samples, measured using a photon energy of 8 keV. The W(C,N) samples S1–S4 showed very similar binding energies of the C 1s, N 1s and W 4f core levels, 283.6 eV, 399.0 eV and 32.2 eV, respectively. The chemical shifts from

the tungsten carbide and nitride reference samples were +0.9 eV and +1.7 eV for carbon and nitrogen, respectively, both shifts indicating a bonding with more electronegative atoms than tungsten or an environment that results in a stronger polarization than in the references. For W 4f_{7/2} the shifts were +0.7 eV and -0.5 eV from the tungsten carbide and nitride references, respectively.

An earlier study of the hexagonal WC_{0.75}N_{0.25} presented C 1s, N 1s and W 4f_{7/2} binding energies of 282.9 eV, 397.0 eV and 32.4 eV [38]. In the same study the C 1s and N 1s binding energies in W(C,N) were shifted by -0.1 eV and +0.1 eV from the tungsten carbide and nitride references and the W 4f_{7/2} binding energies in W(C,N) were shifted respectively by +0.6 eV and -0.8 eV.

The W 4f_{7/2} core level binding energies and their shifts from the carbide and nitride were similar for the W(C,N) coatings presented in this thesis and in [38]. The C 1s and N 1s binding energies were higher for the here presented coatings, by +0.7 eV and +2.0 eV, respectively. The shifts of the p-element binding energies from the carbide and nitride references were also significantly higher in this thesis.

In [38] Ar⁺ etching was used prior to the XPS measurements to a depth of 30 nm (exact etching conditions not described), which may have caused chemical shifts. Damage caused by Ar⁺ etching was studied by Greczynski et. al on Hf-based ceramics [81], which in terms of the TM atomic number are close to the here studied W-based ceramics. Ar⁺ etching at a 4 kV acceleration voltage caused a -0.3 eV shift for the Hf 4f_{7/2} and no shift for the C 1s binding energy in HfC compared to the case without Ar⁺ etching. In HfN, the shift of the Hf 4f_{7/2} binding energy was -0.7 eV and the N 1s peak was split to two contributions, one without and one with a +0.6 eV shift. HfN was thus more prone to sputter damage. Based on the reported shifts caused by Ar⁺ etching, in W(C,N) the difference between the N 1s and C 1s core level energies in the previous literature [38] and in the HAXPES measurements in this thesis cannot be explained by Ar⁺ sputter damage.

The N 1s binding energy at 399.0 eV in the W(C,N) coating in this thesis was close to the binding energy of nitrogen in a nitrile group or in C_xN_y materials [120]. The HAXPES spectra of the undamaged W(C,N) coatings presented in Fig. 5.20 indicates that the carbon dominantly resided in a nitrogen environment and vice versa, while W was found in a carbon-nitrogen environment. Chemical bonds between C and N are, however, not possible in a δ -WC type structure. To further investigate the origin of the chemical shifts, the top surface of an S1 type sample was investigated in STEM and the result is shown in Fig. 5.22. The coating was aligned along a $\langle 10\bar{1}0 \rangle$ zone axis. An approximately 20 nm thick amorphous or nanocrystalline layer was found on top of the crystalline grains with an even thickness all over on the surface. The presence of W in the layer could be confirmed by EDS. The thickness of this layer was comparable with the analysis depth of the HAXPES measurements, a maximum of 27 nm. Therefore, the bonding character of the elements in this

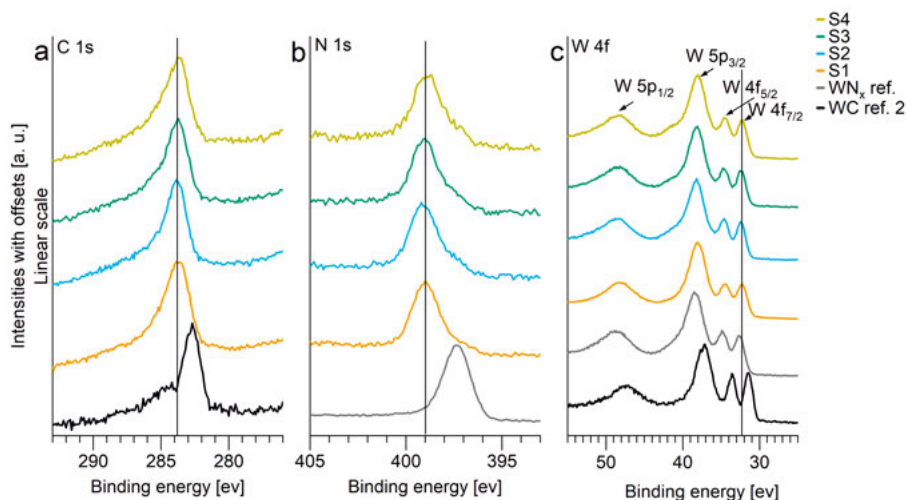


Figure 5.20. Core level HAXPES spectra of the selected W(C,N) coatings and WC and WN_x references acquired at a photon energy of 8 keV. The vertical lines at the positions of the core level binding energies of the W(C,N) coatings are included as a guide.

layer was investigated most probably, instead of that in the crystalline coating. Further investigations would be needed to identify the reason for the formation of this layer.

To investigate the effects of the Ar^+ sputter etching, the S1 coating was also investigated in the in-house XPS instrument both with and without Ar^+ etching. Two Ar^+ etching experiments were carried out, using acceleration voltages of 200 V and 4 kV (pass energy 112 eV). In the first case a sputter etching profile was recorded for 4 hours in 5-minute cycles, in the second case for 15 minutes in half-minute cycles. Since no spectral changes occurred after the second cycle in either case, the spectra of the last 10 cycles were summed for both to reduce the level of noise. Based on previous measurements on other materials, the etching using the 200 V and 4 kV voltages was estimated to result in a material removal to a depth of tens of nanometers and 100–200 nm, respectively. The spectra, including the HAXPES spectra are shown in Fig. 5.21.

The core-level binding energies were the same in the unsputtered XPS and the 8 keV HAXPES spectra. A mild etching with 200 V Ar^+ for several hours resulted in a split N 1s peak, the two components around 398.8 eV and 397.6 eV corresponded to the binding energies of nitrogen in the amorphous or nanocrystalline coating layer and in tungsten nitride, respectively. The W 4f_{7/2} peak was also split, to a carbonitride-like component at 32.4 eV and a carbide-like component at 31.4 eV. The C 1s peak shifted closer to the carbidic core level energy, but only by -0.3 eV, to 283.3 eV. A more energetic etching with 4

kV Ar⁺ for 10–15 minutes resulted in one single N 1s, C 1s and W 4f peak at binding energies of 397.6 eV, 283.3 eV and 31.6 eV. The N 1s binding energy was close to that in tungsten nitride, the C 1s was in between that in tungsten carbide and the surface layer, but closer to the latter and the W 4f binding energy was close to that in tungsten carbide. The W 4f_{7/2} binding energy is expected to have shifted to a carbidic binding energy due to a preferential sputtering of N. Free carbon at a higher binding energy than the main peak could not be detected in either case.

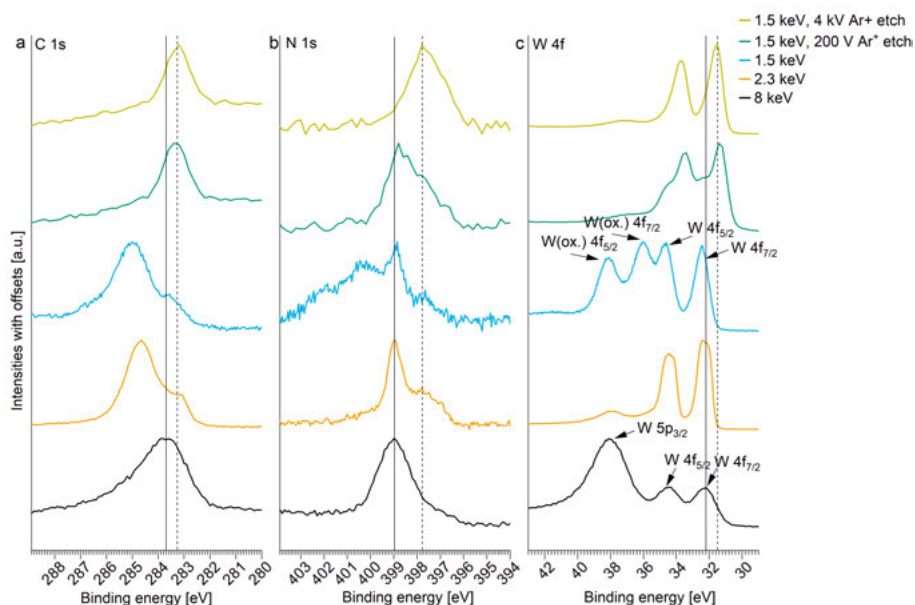


Figure 5.21. Core level photoelectron spectra of coating S1 acquired at photon energies of 2.3 keV and 8 keV using synchrotron radiation and 1.5 keV photon energy using an in-house XPS. In the in-house XPS Ar⁺ etching was also carried out using an acceleration voltage of 200 V (summed spectra of a sputter profile summed between 3 and 4 hours) and 4 kV (summed spectra of a sputter profile summed between 10 and 15 minutes).

5.6 Mechanical and tribological properties of W(C,N)

Five coatings (S1–S5, Table 5.4) that were regarded significantly different in terms of microstructure were selected for the investigations of the mechanical and tribological properties. The coatings differed in grain size and texture as described in Table 5.4. The column widths of the grains and the textures of the coatings were determined from the EBSD data in Paper II. The first mechanical properties are presented in Paper II and a more detailed investigation of the mechanical and tribological properties are the focus of Paper IV.

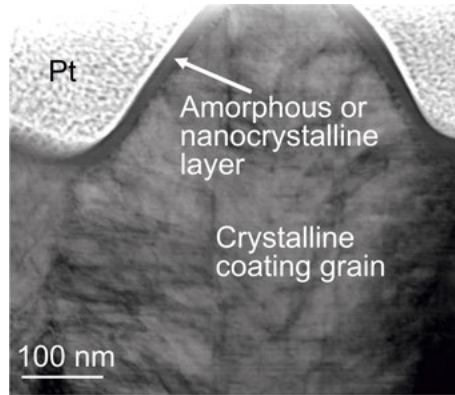


Figure 5.22. STEM BF image of the top part of coating S1.

Table 5.4. Deposition parameters and material properties of the coatings used in the mechanical and tribological investigations. The errors in the column widths indicate a standard deviation based on 100–150 grains.

Sample name	Process description	T[°C]	p(WF ₆) [Pa]	p(H ₂) [Pa]	p(CH ₃ CN) [Pa]	Column width from EBSD [μm]	Texture description
S1	Reference	715	2.4	34	1.6	0.24±0.08	Mixed prismatic
S2	Low p(WF ₆)	715	1.0	34	1.6	0.21±0.08	Prismatic {10 $\bar{1}$ 0}
S3	Low p(H ₂)	715	2.4	17	1.66	0.37±0.08	Partially tilted prismatic
S4	High p(CH ₃ CN)	715	2.4	34	6.3	n/a	Basal+prismatic
S5	High T _{dep}	810	2.4	34	1.6	0.26±0.09	Mixed prismatic

5.6.1 Hardness, elastic modulus and residual stress

The nanoindentation hardness and elastic modulus values are shown in Fig. 5.23. The coatings had a high hardness, and some of the coatings were super-hard with a hardness over 40 GPa. These values are considerably higher than most of the hardness values reported for bulk δ -WC type tungsten carbide, but close to those reported in [29]. Similar values to those of the here presented coatings or even higher values up to 49.2 GPa were reported for W(C,N) coatings deposited by DC magnetron sputtering; the compressive stresses of those coatings were at least 1 GPa and had a maximum 7 GPa [37, 38]. Figure 5.23 shows that the W(C,N) coatings in this thesis deposited by CVD also exhibited compressive stresses, which are believed to have contributed to the high hardness values, especially when compared with other CVD coatings with tensile stresses. The compressive residual stresses in the W(C,N) coatings are likely to be introduced during the post-deposition cooling due to the difference in the coefficient of thermal expansion (CTE) between the substrate and the coating. Assuming a similar CTE for W(C,N) and WC, the substrate has a larger CTE due to its Co content [47, 48]. A high density of defects, e.g. stacking faults and dislocations, observed in the TEM investigation (Figs. 5.11–5.13, 5.15)

was probably a major contributor to the overall high hardness of the coatings as well.

The hardness, elastic modulus and residual stress values are presented in Fig. 5.23. For the hardness values, the 95% confidence intervals are approximately half of the shown standard deviations and therefore S1–S3 had a significantly higher hardness than S4 and S5. S2 was also significantly harder than S3, while S1 and S2 were similar. The expected residual stress values introduced by the CTE differences were around -1 GPa (-0.75 GPa for S4 and -1.25 GPa for S5) as calculated in Paper IV and similar values were obtained for S1, S2 and S4, although the exact peak position determination after the XRD measurements was not certain for S4. S3 exhibited a lower residual stress than expected. For S5 a higher residual stress was expected than for the other coatings based on its higher deposition temperature and Young's modulus, but these experimental and material parameters could not explain a residual stress of -2.5 GPa. Residual stresses that differ from the predicted values have been reported in the literature, but the reasons are not completely understood [46, 121]. In the cited publications some coatings had lower residual tensile stresses than expected.

Several material properties that were determined in Papers II–IV can be the reason for the slightly different hardness values of the coatings. The hardness trend did not follow the trend in the residual stresses. A reason for the superior hardness of S2 may be its narrow grain width (Table 5.4). The lower hardness of S4 may be attributed to its lower coating density, since voids were detected in the coating by STEM imaging (Fig. 5.24.a). Based on its partially basal texture, the hardness of S4 would otherwise be expected to be higher than the hardness of the prismatic textured coatings [29]. The reason for the lower hardness of S5 is currently not known. The deposition at a higher temperature may have influenced the material properties. As mentioned earlier, the high density of defects in the coatings was likely a significant contributor to their high hardness values. Further TEM investigations would be needed to determine if the differences in the coating hardnesses can also be explained by different defect densities in the coatings.

5.6.2 Toughness

The toughness of the W(C,N) coatings was investigated by nanoindentation using a cube corner tip. Two examples of indents on each coating are shown in Fig. 5.25. Additional two indents for each coating are shown in the Supporting information of Paper IV. For all coatings pile-ups at the sides of the indents could be observed. S5 only showed pile-ups and no cracks, indicating that this coating had the highest toughness. S2 only exhibited some short cracks and S1 had more and longer cracks, but was still dominantly plastically deformed by pile-ups. The longer cracks in S3 and S4 indicated that they had the weak-

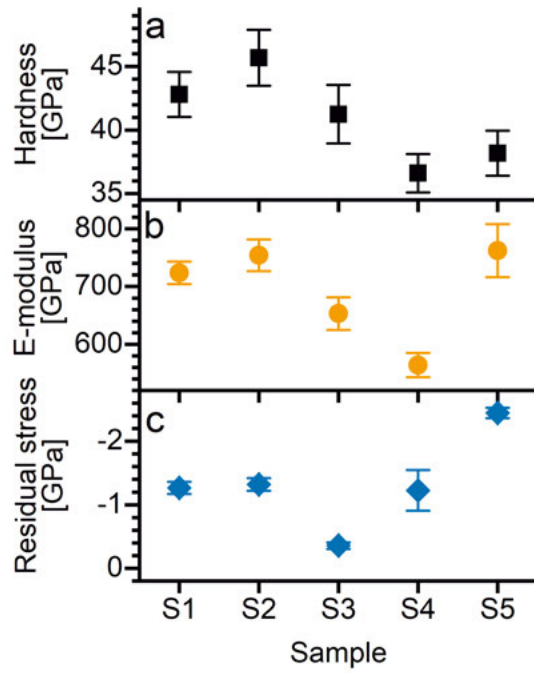


Figure 5.23. Nanoindentation a) hardness, b) elastic modulus and c) residual stress values of the selected W(C,N) coatings. The error bars in a) and b) correspond to one standard deviation calculated from 18–20 indentations. The error bars in c) show one standard deviation based on the linear fitting of 11 measurement points. Adapted from Paper IV.

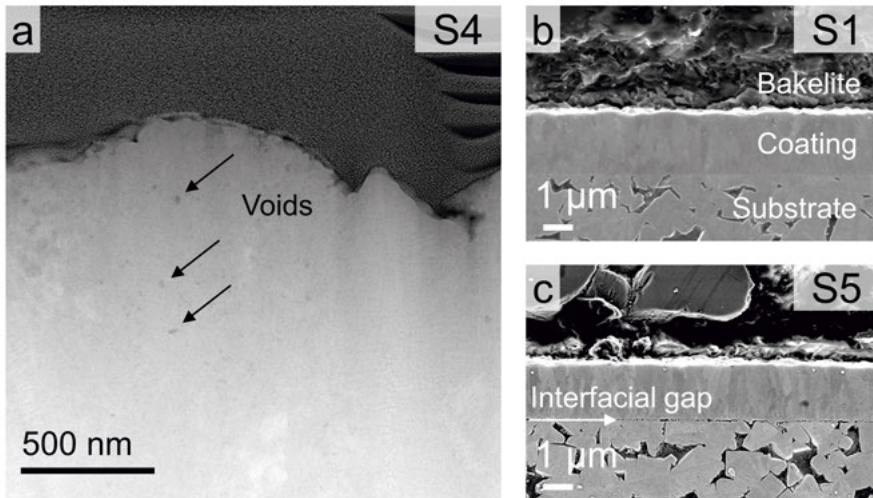


Figure 5.24. a) STEM HAADF image of coating S4. b) and c) are SEM in-lens images of the mechanically polished cross-sections of samples S1 and S5, respectively. Adapted from Papers III and IV.

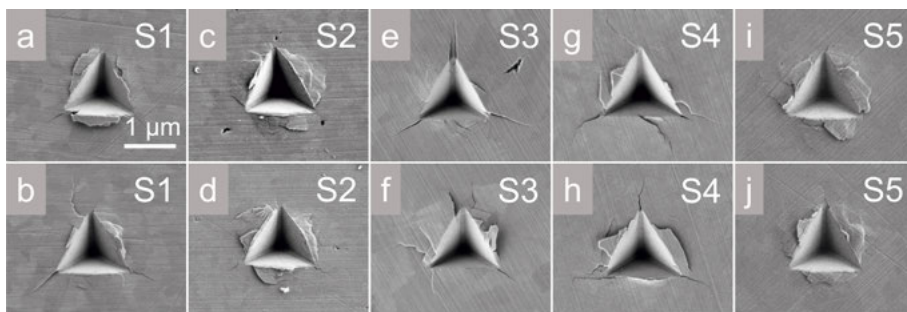


Figure 5.25. SEM secondary electron images of the indents in the W(C,N) coatings obtained with the cube corner tip at a maximum load of 50 mN. Adapted from Paper IV.

est resistance to cracking among the investigated coatings. It is common that similar investigations use maximum loads of 100–200 mN [122, 123], but the instrument used for this thesis had a limit of 50 mN. Higher loads could have initiated more or longer cracks, but the load of 50 mN clearly showed that a plastic deformation with pile-ups is the dominating initial mechanism. The indentation depths were 575–600 nm, and higher loads were therefore not motivated. Considering the Palmqvist crack morphology of WC in a FIB tomography study it is likely that the cracks did not reach the substrate, meaning that only the coatings were probed [89].

In one case for S3, radial cracks formed at all the three edges of the indent, even though some slip traces and an additional crack at one of the edges were observed. From the crack lengths a fracture toughness of $10.3 \text{ MPa} \cdot \text{m}^{1/2}$ could be calculated using equation 3.5, i.e. assuming a Palmqvist crack morphology. Equation 3.5 was used to calculate the toughness of WC grains in cemented carbide in [41] and the values obtained for the basal and prismatic toughness — $7.2 \pm 2.4 \text{ MPa} \cdot \text{m}^{1/2}$ and $8.7 \pm 1.1 \text{ MPa} \cdot \text{m}^{1/2}$ — were lower than the toughness values determined for the W(C,N) coating here. It should be stressed that the radial cracking only occurred for one indent out of four and the effect of the substrate has not been investigated, therefore the calculated value is only an indication of the toughness.

Scratch tests with a 50 μm diamond stylus were used to further investigate the crack resistance of the coatings. The average AE signal values from three scratches are shown in Fig. 5.26.a. The critical loads were determined at the onset of the stabilized elevated AE signal as indicated in the figure. S5 had the highest critical load, which, using a 95% confidence level, was significantly higher than that of S1, S3 and S4. S4 had the lowest critical load, significantly lower than that of S2 and S5. Besides the AE signal, an SEM investigation of the scratch tracks was used to evaluate the crack resistance of the coatings. For all samples except for S5 continuous micro chipping started at the critical load. For S5 the continuous micro chipping started at a higher load. The area

around L_c for S5 is shown in Fig. 5.26.c and Fig. 5.26.b shows the same for S3 for the sake of comparison. The scratch tracks were then compared at a 2 mm sliding distance. S3 had the largest volume of micro chipping at the edge of the scratch track around a 2 mm scratch length as seen in Fig. 5.26.f. This can be compared to Fig. 5.26.d–e,g–h, confirming that S3 had the poorest crack resistance of the coatings. A small area of the flat substrate surface was exposed for coatings S2 and S5 as indicated in Fig. 5.26.e,h and this was not the case for the other coatings in Fig. 5.26.d,f,g,h. An exposed flat substrate surface is an indication of a poorer coating adhesion, which is further discussed in section 5.6.4. The scratch tests with a 50 μm diamond stylus showed that S5 had the best crack resistance, followed by S1 and S2, which performed similarly and then finally by S3 and S4, with S3 exhibiting the largest micro chipping volume.

The toughness trends observed with the cube corner indentations and the scratch tests were the same, S5 had the highest toughness and S3 and S4 exhibited a poorer crack resistance. The superior crack resistance of S5 may be attributed to its lower hardness and higher compressive stress (Fig. 5.23). S2 had the smallest column width of the studied coatings, which may have been contributor to its good toughness (Table 5.4). S3 had larger grains and S4 had voids, which are possible contributors to their poorer crack resistance. As in case of the hardness, the defect density and the types of defects in the coatings may be contributors to their different cracking behaviors.

5.6.3 Abrasive wear resistance

The abrasive wear rate of coatings S1–S5 is summarized in Fig. 5.27. The wear rates were similar for the coatings, S3 had the highest wear rate and S2 the lowest, but there were uncertainties in the determination of the crater diameters. The character of the abrasive wear was investigated with the help of SEM imaging to determine the relative area where micro chipping, a more aggressive wear mechanism than micro cutting or micro plowing occurred. One crater was analyzed for each coating. The relative micro chipped areas of S1–S5 were, respectively 1.5 %, 0.9 %, 7.1 %, 8.1 % and 0.3 %. Similarly to other tests above, S3 and S4 showed the poorest performance in the abrasive wear tests as well. Half of a worn crater for S3 and S5 is compared in Fig. 5.28.a,b. An example of an area with micro chipping is shown in Fig. 5.28.c. Figure 5.28.d shows an example of an area with micro cutting (or micro plowing, a differentiation is not possible with the applied imaging method), the almost exclusive mechanism for S5. The low proportion of micro chipped area for all W(C,N) coatings indicates a good coating quality and that a predictable coating performance can be expected in cutting applications.

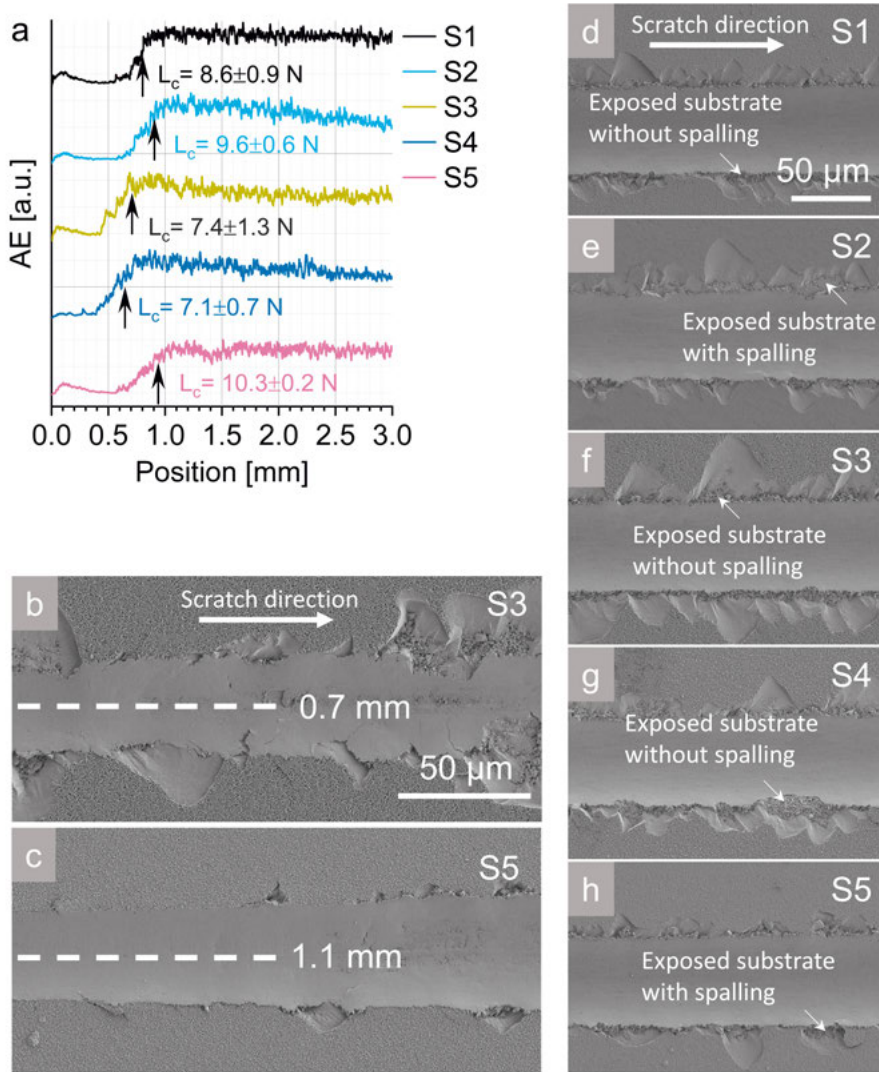


Figure 5.26. Results of the scratch tests carried out with the 50 μ m diamond stylus. a) averaged AE signals and average L_c values with 95% confidence intervals for samples S1–S5. b) and c) are SEM secondary electron images of scratch tracks centered at the critical loads with the sliding distances indicated, for samples S3 and S5, respectively, for the scale see b). d–h are SEM secondary electron images of a scratch track centered at 2 mm for samples S1–S5, for the scale see d). Adapted from Paper IV.

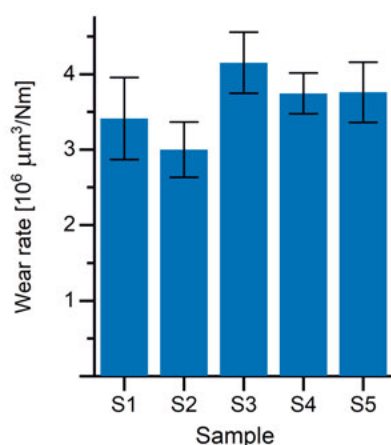


Figure 5.27. Wear rates of the coatings in micro-scale abrasion tests carried out with $1 \mu\text{m}$ diamond particles. The error bars show one standard deviation propagated from the statistical error of the diameter measurements from at least 9 craters for each coating. Adapted from Paper IV.

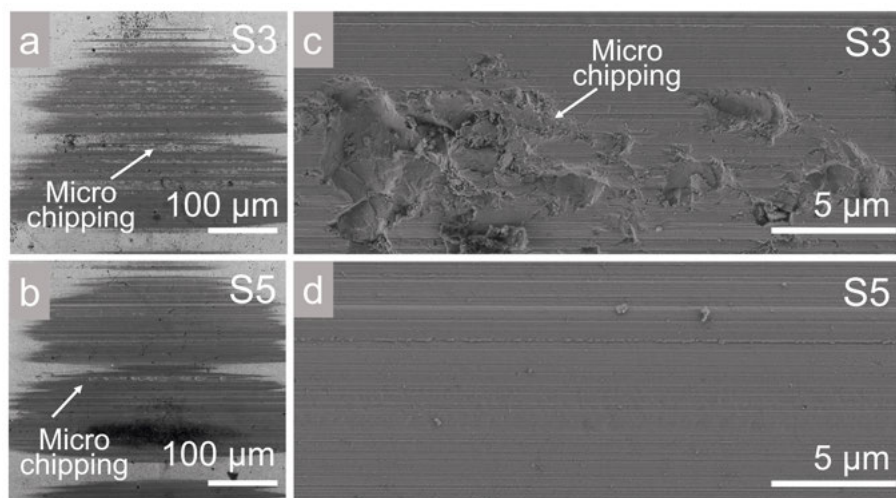


Figure 5.28. SEM secondary electron micrographs of a part of the wear craters formed during the abrasive wear tests with $1 \mu\text{m}$ diamond particles. In a) and b) half of a crater for S3 and S5 are compared and the brighter areas inside the crater are areas where micro chipping occurred. c) shows an example of coating micro chipping for sample S3 and d) shows coating micro cutting for sample S5. Adapted from Paper IV.

5.6.4 Adhesion

An overall good adhesion of the W(C,N) coatings to the cemented carbide substrate was observed in the multi-pass scratch tests with a 200 μm diamond stylus. The critical loads were determined where a significant increase was observed in the AE signal and are presented in more detail in Paper IV. Figure 5.29 shows the wear tracks for all coatings at a 2 mm sliding distance, which was a position beyond the scratch length where the critical loads were reached according to the AE signals. No coating spalling was observed for samples S1, S3 and S4, instead substrate micro chipping occurred as shown in Fig. 5.29.a,f,c,h,d,i. The edge of the wear track followed the granularity of the substrate for these coatings. The chemical and mechanical similarity between the coatings and the substrate is probably the reason for a good adhesion. For S2 and S5 spalling occurred and the flat surface of the substrate can be observed in Fig. 5.29.b,g,e,j. The poorer adhesion of these coatings could be related to Co diffusion to the substrate-to-coating interface. Co was etched during the oxide polishing step when preparing the cross-sections for SEM, but its presence was confirmed by EDS. A narrow interfacial gap was observed in SEM. Such a gap was not observed for samples S1, S3 and S4. A comparison of two cross-sections, one with and one without an interfacial gap is shown in Fig. 5.24.b and c. In general, Co or an η -phase at the interface could be related to a higher deposition temperature in Paper II, which probably explains the described phenomenon at 810 °C for S5. As the experiments at 715 °C were repeated several times, a higher amount of Co was obtained at the substrate-to-coating interface occasionally, but the mechanism of Co enrichment could not be connected to a certain process. The low pressure (0.2 Torr) and high temperature during the heating of the reactor or tungsten fluoride (WF_x) residues from a previous deposition process reacting with the substrate before the depositions can be the cause of Co enrichment. The Co enrichment may therefore be avoided and the adhesion can be improved by a higher total pressure during the heating step or by baking out the reactor between processes. For higher deposition temperatures a starting layer deposited at a lower temperature can also be a strategy to improve the adhesion, which is important for the otherwise tough S5 coating.

5.6.5 Conclusions from the mechanical and tribological investigations

The W(C,N) coatings deposited by CVD were superhard with hardness values close to 40 GPa and at the same time they showed indications of a good toughness. The adhesion to the substrate was excellent, no adhesive failure occurred for three coatings under the applied test conditions and only two of the five coatings showed a poorer adhesion. Co at the substrate-to-coating interface was identified as a reason for a poorer coating adhesion and some strategies

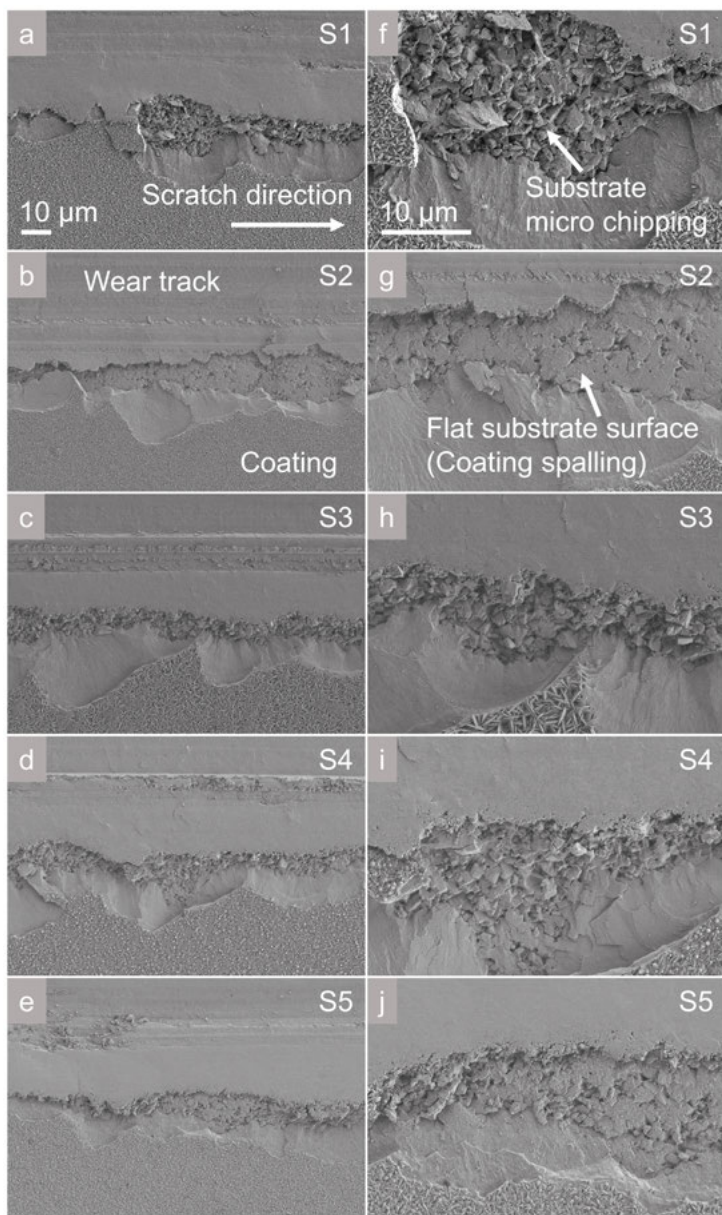


Figure 5.29. SEM secondary electron images of the edges of the wear tracks at a 2 mm sliding distance after the multi-pass scratch tests carried out with a 200 μm Rockwell C diamond stylus. The images in the left and the right, respectively, were recorded at the same magnifications. Adapted from Paper IV.

were suggested to avoid Co at the interface. No significant effect of the texture on the mechanical and tribological properties could be determined. Instead, a dense columnar microstructure is preferred for a good material performance, the coating that had a less dense microstructure (sample S4) showed an overall poorer performance. The hardest coating with a superior hardness was S2 having the narrowest grain column width and this coating had also a good toughness. This coating was similar to coating S1 in terms of performance. The best toughness was achieved by the highest deposition temperature, 810 °C (sample S5). A high hardness and toughness of the coatings can probably be attributed to a high density of defects and that the grains consisted of coherent nano-domains in the 5 nm size range, as discussed in Section 5.4. The good toughness may also be attributed to the high VEC and the compressive stresses, the two main considerations when deciding for the development of W(C,N) coatings (Sections 2.2.2 and 2.2.4). The dominating wear mechanism for abrasive wear was micro cutting (or micro plowing), indicating a predictable wear behavior.

6. Summary, conclusions and outlook

In Paper I it was shown that CoCrFeNi is a substrate that can be coated by TiN in CVD processes carried out between 850 °C and 950 °C using TiCl₄, N₂ and H₂ precursors. No severe substrate etching or intermetallic phase formation between the substrate and Ti in the gas phase or in the coating occurred. Cr appeared in the grain boundaries and on the top surface of the coating deposited at 950 °C and nitride formation was determined as the driving force. The coating growth was not disturbed by the Cr diffusion, columnar grains grew as expected for the TiN deposition under the applied conditions. CoCrFeNi is therefore a possible alternative binder phase for cemented carbide and could possibly be coated with CVD TiN as a standalone alloy for other applications. Further investigations will be needed on how Cr in the grain boundaries influences the mechanical properties of the coatings and on the influence of Cr at the top surface on the nucleation and growth of the next layer in a multi-layer coating.

The main part of the thesis, based on Papers II–IV, presents the successful deposition of W(C,N) coatings on cemented carbide by CVD with a coating quality yielding good mechanical and tribological properties. The coatings are thus promising candidates for future applications in cutting tools. Paper II describes the development of the deposition process and the current understanding of the coating growth. In Paper II a process parameter window was determined, the possible deposition temperatures ranged between 665 °C and 810 °C and the processes were carried out at 133 Pa. The WF₆ and CH₃CN precursor partial pressures were similar and H₂ was used in excess. Paper II shows that the selection of the CH₃CN and WF₆ precursors, together with H₂ results in a balanced deposition chemistry. Within the defined process parameter window, the temperatures are high enough for CH₃CN decomposition and the W(C,N) deposition is kinetics controlled, where CH₃CN has a role in slowing down the deposition compared to pure W deposition without CH₃CN. From the reaction orders of the reactants it was suggested that the reaction rate within the process window is mainly dependent on the W incorporation rate.

The coatings consisted of the hexagonal δ -WC type phase. The microstructure of the coatings was columnar and the column width and to some extent the top morphology could be tuned by process parameter variations. The top surface of the grains was ridge-like. A larger grain size positively correlated with a broader texture distribution. The texture was prismatic, i.e. the c-planes of the hexagonal structure were parallel to the growth direction. STEM and EBSD investigations in Paper III revealed that the c-planes were also parallel to the grain ridges, and thus the coating texture could be related to the

grain morphology. A basal texture would be desirable for a higher hardness, but a partially basal texture could only be achieved together with a significantly changed microstructure, at a high CH_3CN partial pressure. Superior mechanical properties that would be expected for a basal microstructure were not achieved in this case, shown in Papers II and III and voids in the coating were identified as a possible reason.

TEM/STEM investigations in Paper III on the atomic and nano level structure of the coatings showed that the coatings were rich in stacking faults and dislocations. Stacking faults in the stacking of the $\{10\bar{1}0\}$ planes yielded grains with defect-free domains with a diameter of only 5 nm. At the center of the grains the ...AA... stacking of the tungsten c-planes along the c-direction changed and some planes were instead positioned in a shifted B position. It was proposed that the nucleation and the growth is probably fast at these stacking faults, governing the initial growth stage. Similarities were found between the texture and top morphology of the prismatic textured hexagonal W(C,N) coatings and $\langle 211 \rangle$ or $\langle 110 \rangle$ textured cubic NaCl structured ceramic coatings. The close packed metallic planes are parallel to the growth direction in both material systems. At the center of the grains, the stacking faults of the close packed W planes can be compared with the $\{111\}$ twin plane at the center of grains of the cubic ceramic coatings.

A combined relative RBS and ERDA characterization was needed to determine a composition that is believed to be accurate, with a (C+N)/W ratio close to 1 and a N/(C+N) ratio close to 0.3. HAXPES analysis completed with STEM characterization showed that a 20 nm amorphous or nanocrystalline layer formed on top of the coatings, hindering the characterization by HAXPES, which would otherwise be preferred to XPS characterization with Ar^+ etching. The results proved the importance of a careful characterization technique selection for the elemental and spectroscopic analysis of materials containing both heavy and light elements and stressed the necessity to apply multiple characterization techniques.

The coatings had a high nanoindentation hardness between 37 and 46 GPa, shown in Paper II, which was higher than would be expected based on the hardness of bulk WC and WN with a δ -WC type structure. Cube corner indentations and scratch tests in Paper IV indicated a good coating toughness as well. A high VEC, an intrinsic material property was probably part of the reason for a high toughness. It is likely that a combined high hardness and toughness is a result of a high density of defects and the grains consisting of domains that were only about 5 nm in size (Paper III). A compressive stress in the coatings is probably a further contributor to the high hardness and toughness of the coatings. The coating with the smallest column width had the highest hardness and the coating deposited at a high deposition temperature (810 °C) exhibited the best toughness. Differences in the nano level structure and the defect densities of the coatings are probably also reasons for the differences in the mechanical and tribological properties, but further investigations

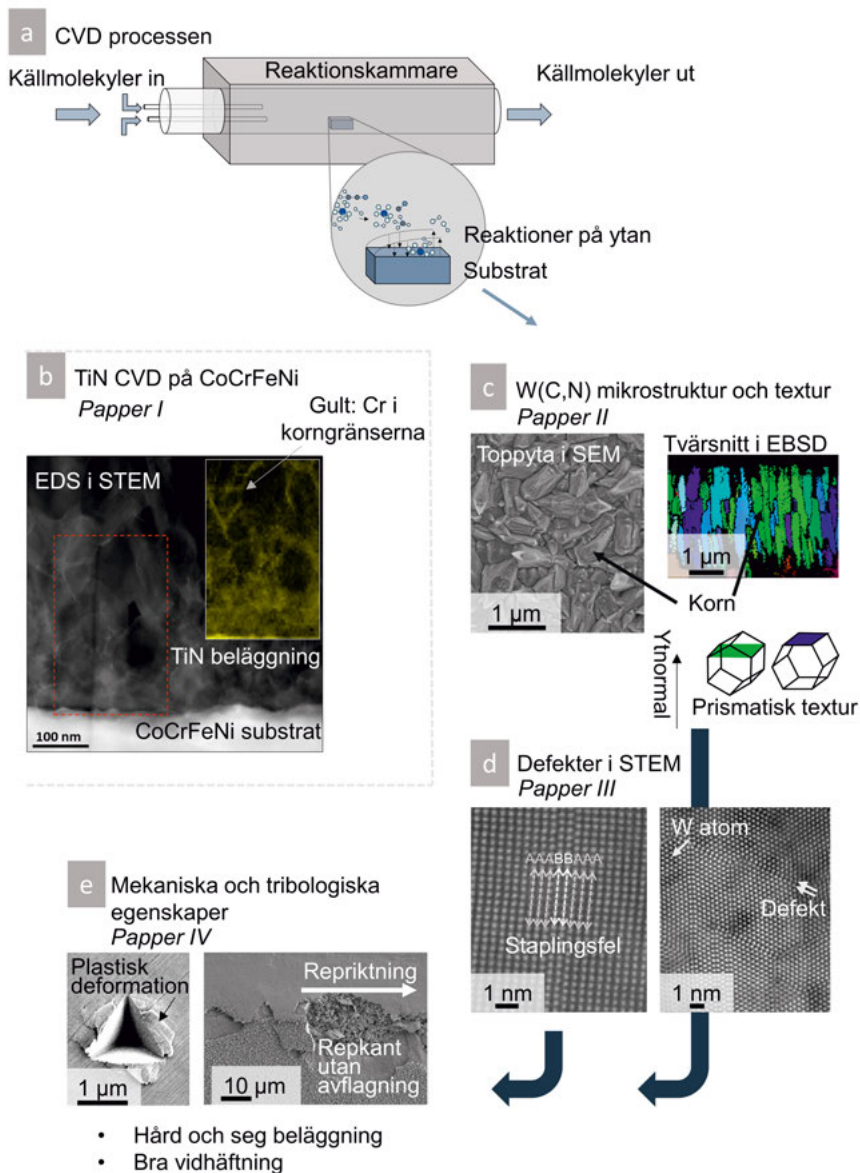
will be needed to reveal these structural differences. An overall good coating adhesion was observed, some substrate-coating systems did not show any coating spalling under the applied scratch test conditions.

This thesis presents the development and a first detailed characterization of new W(C,N) CVD coatings on cemented carbide. Further work could include toughness measurements of the coatings by microcantilever or micropillar tests. These tests would allow for the characterization of the coating material itself and a fairer comparison with other materials, since the substrate effects are eliminated in the suggested tests. The cube corner tests carried out in the thesis are, however, believed to be more suitable for the investigation of the coatings as part of the whole coating-substrate system. The deformation mechanism during the cube corner indentation could be revealed in the future by STEM investigation of the coating volume where pile-ups occurred. The next investigation step towards applications would be to carry out cutting tests and preferably compare the coatings to previously developed coatings for cutting tools. Given the excellent adhesion of the coatings to the substrate, their compressive stresses, high hardness and good toughness, a thinkable application is intermittent cutting, such as milling or facing.

7. Populärvetenskaplig sammanfattning

Verktyg för skärande bearbetning av metaller behöver klara av miljön som uppstår vid användningen vid höga temperaturer och höga tryck. Hårdmetall är ett material som ofta används i verktyg. Den vanligaste huvudkomponenten i hårdmetall är därför volframkarbid (WC), som är ett keramiskt material. Keramiska material kan ha olika typer av bindningar: joniska, kovalenta och metalliska och bindningarna i materialet avgör dess egenskaper. I volframkarbid är de kovalenta och metalliska bindningarna dominerande. De kovalenta bindningarna gör att WC är ett hårt material som är svårt att deformera jämfört med metaller, en egenskap som gör att WC kan användas för metallbearbetning. Volframkarbid är dock också spröd, vilket innebär att sprickor uppstår när materialet utsätts för hög belastning. För att minska sprödheten (öka segheten) hos volframkarbid så tillsätts små mängder kobolt (Co), en metall som är segare än volframkarbid men också mjukare, denna mjuka fas kallas för bindefas. För att få optimala egenskaper för vissa applikationer kan den relativa mängden av WC och Co varieras och hårdare keramer, titankarbonditrider kan också tillsättas. Ett annat vanligt sätt som används för att göra verktyget mer motståndskraftigt och optimera det för tuffa bearbetningsprocesser är att belägga materialet med ett eller flera lager av några mikrometer tjocka keramiska material. Kemisk ångdeponering, som oftast kallas för chemical vapor deposition (CVD) även på svenska, är en metod för att framställa tunna beläggningar. Materialet som beläggningen deponeras på kallas för substrat i denna process. Figur 7.1.a visar en skiss på CVD processen. Processen innebär att gasmolekyler (källmolekyler) transporteras över substratyten där de reagerar och ett nytt fast material bildas. För att reaktionen ska kunna ske behövs någon form av aktivering, till exempel termisk aktivering, och därför värms reaktionskammaren till temperaturer från typiskt 750 °C till temperaturer över 1000 °C. I det allra vanligaste fallet transporteras källmolekyler kontinuerligt till reaktionskammaren och de flyktiga biprodukterna och oreagerade källmolekylerna transporteras sedan bort från reaktionskammaren. En viktig fördel med CVD är att sådana mikrostrukturer kan skapas som inte är möjliga att skapa med andra metoder och att mikrostrukturen kan styras med hjälp av processparametrarna.

Det finns ett ständigt behov av utveckling av både hårdmetallen och beläggningarna. Utvecklingen måste ske parallellt, eftersom substratet och beläggningarna utgör ett system tillsammans och dessutom kan substratet och källmolekylerna reagera med varandra under beläggningsprocesserna. Denna avhandling handlar om två forskningsprojekt, i det första har ett nytt substratmaterial undersökts i en konventionell CVD process, i det andra har en ny



Figur 7.1. a) Skiss på CVD processen. b) STEM-EDS bild som visar Cr i korngränserna när TiN deponerades på CoCrFeNi substrat. c) Mikrostruktur och textur på en W(C,N) beläggning. d) Högupplösta STEM bilder som visar typiska defekter i W(C,N) beläggningar. e) Plastisk deformation av W(C,N) beläggningen under ett intryck med diamantspets och reptestresultat som visar på en bra vidhäftning till hårdmetall.

beläggning utvecklats, karakteriserats och testats med mekaniska och tribologiska tester.

Det nya substratmaterialet är kobolt-krom-järn-nickel (CoCrFeNi), en multikomponentlegering som innehåller fyra olika metaller i lika mängder och därför kan förväntas att ha andra egenskaper än konventionella legeringar som har en eller två huvudkomponenter. CoCrFeNi är ett korrosionsresistent och värmetåligt material som har dessutom redan testats som alternativ bindefas istället för Co i hårdmetall. Den första beläggningen som läggs på hårdmetallen för verktygstillverkning är vanligtvis titannitrid (TiN), och det är därför viktigt att förstå om CoCrFeNi kan beläggas med TiN. TiN är dessutom en korrosionsresistent och hård beläggning som möjligen kan tillämpas i andra applikationer av CoCrFeNi. Under de höga temperaturerna som används i CVD processerna finns det en risk att substratet reagerar med källmolekylerna. Titannitrid deponeras ofta från titantetraklorid (TiCl_4), kväve (N_2) och väte (H_2) källmolekyler vid temperaturer över 850 °C. Vid dessa temperaturer är TiCl_4 mycket korrosiv mot många substrat. I paper I har det visats att CoCrFeNi inte etsas och att den inte bildar några icke-önskvärda intermetalliska faser såsom Ni_3Ti . Detta bevisades med hjälp av röntgendiffraktion (XRD), svepelektronmikroskopi (SEM) och sveptransmissionselektronmikroskopi (STEM), karakteriseringsmetoder som används för att identifiera kristallina faser och avbilda materialens mikrostruktur ner till en atomär nivå. Det enda komplikationen som kunde identifieras var att krom diffunderar in i beläggningen längs titanitridens korngränser. Detta har visats med energidispersiv röntgenspektroskopi (EDS) i STEM, en metod som kan användas för kartläggning av grundämnen på nanometerskala (Figur 7.1.b). Fenomenet kunde förklaras med hjälp av termodynamiska beräkningar, som visade att krom gärna bildar en nitridfas med N_2 i gasfasen eller med TiN beläggningen.

Huvudprojektet i denna avhandling var framställningen av en ny beläggning, volframkarbonitrid (W(C,N)) för hårdmetall. W(C,N) förväntades vara segare än titankarbonitrid (Ti(C,N)), en CVD beläggning som används kommersiellt på hårdmetall, på grund av att W(C,N) har en starkare metallisk karaktär. Eftersom W(C,N) liknar huvudkomponenten i hårdmetall, var förväntningen också att substratet och beläggningen kommer att ha liknande utvidningskoefficienter eller att beläggningens utvidningskoefficient skulle vara högre. Det skulle innebära att inga dragspänningar och istället tryckspänningar introduceras i beläggningen under nedkylningen efter CVD processen. Tryckspänningar leder till högre hårdhet och sprickmotstånd. Volframhexafluorid (WF_6), acetonitril (CH_3CN) och vätgas användes för att deponera W(C,N) . Ett processparameterfönster har definierats i Paper II: W(C,N) beläggningar med en mikrostruktur som består av kolumnära korn och hexagonal kristallstruktur (Figur 7.1.c) kunde deponeras mellan 665 °C och 810 °C och under ett väldigt lågt tryck, 133 Pa. WF_6 och CH_3CN användes i jämförbara mängder med vätgas i överskott. I Paper II och III undersöktes mikrostrukturen, den dominerande orienteringen av kornen (texturen) och hur filmtillväx-

ten leder till dessa materialegenskaper. SEM och elektrondiffraktion i SEM (EBSD) visade att kolumnbredden på kornen kunde justeras med processparametrarna. Beläggningarna hade en prismatiskt textur (se Figur 7.1.c för en förklaring) enligt EBSD och XRD. Texturen kunde kopplas till beläggningarnas toppmorfologi, de hexagonala kristallplanen var parallella med kornens bergsrygg-liknande centrala linje, vilket visades av en STEM-undersökning i papper III. Staplingsfel (defekter) hittades i staplingen av de hexagonala kristallplanen i mitten av kornen och dessa staplingsfel kan ha påverkat kornens tillväxt. Ett sådant staplingsfel visas i Figur 7.1.d. Hårdhetsmätningar och seghetsmätningar där små diamantspetsar används för att deformera material på ett kontrollerat sätt på nanometerskala visade att beläggningarna var superhårda och samtidigt sega (Fig. 7.1.e). Den högsta hårdheten som uppmättes, 46 GPa, är en hårdhet som når upp till halva värdet för diamant, det hårdaste material vi känner till. Dessa egenskaper kunde förklaras med tryckspänningarna som uppmättes, en hög densitet på defekter (ett exempel visas i Figur 7.1.d) och en kolumnbredd på några hundra nanometer (Figur 7.1.c). Reptester med en rund diamantspets med en 200 μm radie som används för att undersöka om beläggningen flagnar av vid belastning visade utmärkt vidhäftning mellan substratet och beläggningen, några beläggningar visade ingen avflagnings i testerna (Figur 7.1.e). Slutsatsen av studierna är att de nya CVD W(C,N) beläggningarna är lovande kandidater som beläggningar på hårdmetall för skärande bearbetning.

8. Acknowledgements

First of all, I would like to thank my main supervisor, Mats Boman for giving me an interesting project, all the scientific discussions and his guidance throughout my PhD. My co-supervisor Linus von Fieandt for all his valuable suggestions and for the discussions. Erik Lindahl, my co-supervisor for all the input and help at the beginning of my PhD. Ulf Jansson and Leif Nyholm for their valuable comments on my work and thesis.

I am happy to have been part of the CVD group. I would like to thank Johan Gerdin Hulkko for constructing the CVD reactor and integrating very useful features into the control software. Sebastian Öhman for the all the conversations and the shared conference and beamtime experiences.

I would like to thank my collaborators and co-authors. Ren Qiu, Olof Bäcke and Mats Halvarsson for the TEM work. Axel Forslund and Henrik Larsson for the CALPHAD calculations. Mikael Fallqvist for all the help with the tribological tests. Rebecka Lindblad for guiding me during the beamtime and through the HAXPES/XPS data evaluation. Fredrik Johansson, Elin Berggren and Sebastian Öhman and the scientists at Soleil for the support during the beamtime. Mauricio Sortica and Daniel Primetzhofer for the ion beam analyses and the discussions on the results. I also thank Tommy Larsson, Jonas Lauridsen, Oscar Alm, Ulrika Medin and Wei Wan for the collaboration.

I would like address special thanks to some colleagues at the Ångström Laboratory. I thank Mikael Ottosson for taking care of the XRD lab and the discussions on the measurements. Erik Lewin for the discussions on XPS data. Rolf Berger for the linguistic review of some of my papers. Leif Edlén, Jan Bohlin for their engineering work on the reactor components, Pedro Berastegui and Dennis Karlsson for taking care of the equipment in the basement. The research engineers at Myfab for the assistance in the clean room. The PVD group, Babsi, León, Stefan, Anna and Kristina for the interesting discussions and the great times at conferences. The administration for making administrative work easier. I am happy to have worked in the bulk group led by Martin Sahlberg during my master thesis before I started to work with thin films.

I would like to thank my colleagues in the structural and inorganic chemistry groups: Markus, Sarmad, Lejdan, Therese, Zack, Tatiana, Gustav, Aishwarya, Yu-Chuan, Ashok, Andoria, Le Anh, Simon L., Victor, Yonas, Isabelle, Simon C., Olle, Robin, Rassmus, Andy, Guiomar, Tim, Viktor, Maria, Elina, Rebecca, Johan C., Adriano, Rodrigo, Ida, Djurdjija and all others not mentioned here for creating a pleasant work environment and for the activities

outside work. I would like to thank Mario for being a nice office mate, the nice conversations and the scientific discussions.

Finally, I would like to thank my family and friends for all the meaningful time spent together and special thanks for your support during the last months of my PhD. I thank my grandparents for their support over the years. My siblings, Zsófi and Peti and my parents for their endless support and for being always there for me.

Bibliography

- [1] N. Schalk, M. Tkadletz, and C. Mitterer. Hard coatings for cutting applications: Physical vs. chemical vapor deposition and future challenges for the coatings community. *Surf. Coatings Technol.* 429 (2022), 127949. <https://doi.org/10.1016/j.surfcoat.2021.127949>.
- [2] K. Bobzin. High-performance coatings for cutting tools. *CIRP J. Manuf. Sci. Technol.* 18 (2017), 1–9. <https://doi.org/10.1016/j.cirpj.2016.11.004>.
- [3] I. Hutchings and P. Shipway. Wear by hard particles. *Tribol. Frict. Wear Eng. Mater.* 2nd. Butterworth-Heinemann, 2017. Chap. 6, 165–236. <https://doi.org/10.1016/B978-0-08-100910-9.00006-4>.
- [4] I. Endler et al. Novel aluminum-rich $\text{Ti}_{1-x}\text{Al}_x\text{N}$ coatings by LPCVD. *Surf. Coatings Technol.* 203 (2008), 530–533. <https://doi.org/10.1016/j.surfcoat.2008.04.098>.
- [5] B. Cantor, I. T. Chang, P. Knight, and A. J. Vincent. Microstructural development in equiatomic multicomponent alloys. *Mater. Sci. Eng. A* 375–377 (2004), 213–218.
- [6] J.-W. Yeh et al. Formation of simple crystal structures in Cu-Co-Ni-Cr-Al-Fe-Ti-V alloys with multiprincipal metallic elements. *Metall. Mater. Trans. A* 35A (2004), 2533–2536.
- [7] J. W. Yeh et al. Nanostructured high-entropy alloys with multiple principal elements: Novel alloy design concepts and outcomes. *Adv. Eng. Mater.* 6 (2004), 299–303.
- [8] E. Holmström et al. High entropy alloys: Substituting for cobalt in cutting edge technology. *Appl. Mater. Today* 12 (2018), 322–329. <https://doi.org/10.1016/j.apmt.2018.07.001>.
- [9] J. García et al. In situ investigations on stress and microstructure evolution in polycrystalline $\text{Ti}(\text{C,N})/\alpha\text{-Al}_2\text{O}_3$ CVD coatings under thermal cycling loads. *Crystals* 11 (2021), 1–18. <https://doi.org/10.3390/cryst11020158>.
- [10] H. Kindlund, D. G. Sangiovanni, I. Petrov, J. E. Greene, and L. Hultman. A review of the intrinsic ductility and toughness of hard transition-metal nitride alloy thin films. *Thin Solid Films* 688 (2019), 137479. <https://doi.org/10.1016/j.tsf.2019.137479>.

- [11] H. O. Pierson. Handbook of Chemical Vapor Deposition. Ed. by H. O. Pierson. 1st. Westwood, NJ, USA: Noyes Publications, 1992. <https://doi.org/10.1016/b978-0-8155-1300-1.50007-6>.
- [12] J. Gerdin Hulkko. “Muspel and Surtr: CVD system and control program for WF6 chemistry”. Licentiate thesis, Monograph. Uppsala University, 2019. <http://uu.diva-portal.org/smash/record.jsf?pid=diva2%5C%3A1317466%5C&dswid=-4885>.
- [13] J.-O. Carlsson and P. M. Martin. Chemical Vapor Deposition. *Handb. Depos. Technol. Film. Coatings*. Ed. by P. M. Martin. 3rd. Oxford, UK: William Andrew Publishing, 2010. Chap. 7.
- [14] V. Pacheco et al. Thermal Stability of the HfNbTiVZr High-Entropy Alloy. *Inorg. Chem.* 58 (2019), 811–820. <https://doi.org/10.1021/acs.inorgchem.8b02957>.
- [15] L. von Fieandt, T. Larsson, E. Lindahl, O. Bäcké, and M. Boman. Chemical vapor deposition of TiN on transition metal substrates. *Surf. Coat. Technol.* 334 (2017), 373–383. <https://doi.org/10.1016/j.surfcoat.2017.11.063>.
- [16] P. H. Mayrhofer, R. Rachbauer, D. Holec, F. Rovere, and J. M. Schneider. Protective Transition Metal Nitride Coatings. Vol. 4. Elsevier, 2014, 355–388. <http://dx.doi.org/10.1016/B978-0-08-096532-1.00423-4>.
- [17] E. Broitman. Indentation Hardness Measurements at Macro-, Micro- and Nanoscale: A Critical Overview. *Tribol. Lett.* 65 (2017), 1–18. <https://doi.org/10.1007/s11249-016-0805-5>.
- [18] W. F. Hosford. Ductility and Fracture. *Mech. Behav. Mater.* 1st. Cambridge: Cambridge University Press, 2005, 210–226. <https://doi.org/10.1017/CB09780511810930.015>.
- [19] K. Balasubramanian, S. V. Khare, and D. Gall. Valence electron concentration as an indicator for mechanical properties in rocksalt structure nitrides, carbides and carbonitrides. *Acta Mater.* 152 (2018), 175–185. <https://doi.org/10.1016/j.actamat.2018.04.033>.
- [20] U. Jansson and E. Lewin. Sputter deposition of transition-metal carbide films - A critical review from a chemical perspective. *Thin Solid Films* 536 (2013), 1–24. <http://dx.doi.org/10.1016/j.tsf.2013.02.019>.
- [21] T. Glechner et al. Tuning structure and mechanical properties of Ta-C coatings by N-alloying and vacancy population. *Sci. Rep.* 8 (2018), 1–11. <https://doi.org/10.1038/s41598-018-35870-x>.

- [22] H. W. Hugosson, O. Eriksson, U. Jansson, and B. Johansson. Phase stabilities and homogeneity ranges in 4d-transition-metal carbides: A theoretical study. *Phys. Rev. B - Condens. Matter Mater. Phys.* 63 (2001), 1–11. <https://doi.org/10.1103/PhysRevB.63.134108>.
- [23] C. Saringer et al. Thermal expansion of magnetron sputtered $\text{TiC}_x\text{N}_{1-x}$ coatings studied by high-temperature X-ray diffraction. *Thin Solid Films* 688 (2019), 137307. <https://doi.org/10.1016/j.tsf.2019.05.026>.
- [24] R. Qiu et al. Schmid factor analysis for chip flow induced plastic deformation of textured cubic carbonitride coatings. *Int. J. Refract. Met. Hard Mater.* 108 (2022).
- [25] T. Takahashi and E. J. Freise. Determination of the slip systems in single crystals of tungsten monocarbide. *Philos. Mag. A J. Theor. Exp. Appl. Phys.* 12 (1965), 1–8. <https://doi.org/10.1080/14786436508224941>.
- [26] S. B. Luyckx. Slip system of tungsten carbide crystals at room temperature. *Acta Metall.* 18 (1970), 233–236. [https://doi.org/10.1016/0001-6160\(70\)90028-3](https://doi.org/10.1016/0001-6160(70)90028-3).
- [27] A. I. Gusev and A. S. Kurlov. Tungsten Carbides Structure, Properties and Application in Hardmetals. Springer International Publishing Switzerland, 2013. <https://doi.org/10.1007/978-3-319-00524-9>.
- [28] J. García, V. Collado Ciprés, A. Blomqvist, and B. Kaplan. Cemented carbide microstructures: a review. *Int. J. Refract. Met. Hard Mater.* 80 (2019), 40–68. <https://doi.org/10.1016/j.ijrmhm.2018.12.004>.
- [29] T. Csanádi, M. Bl’Anda, N. Q. Chinh, P. Hvizdoš, and J. Dusza. Orientation-dependent hardness and nanoindentation-induced deformation mechanisms of WC crystals. *Acta Mater.* 83 (2015), 397–407. <https://doi.org/10.1016/j.actamat.2014.09.048>.
- [30] R. Pero, G. Maizza, R. Montanari, and T. Ohmura. Nano-indentation properties of tungsten carbide-cobalt composites as a function of tungsten carbide crystal orientation. *Materials (Basel)*. 13 (2020), 2137. <https://doi.org/10.3390/ma13092137>.
- [31] H. L. Brown, P. E. Armstrong, and C. P. Kempter. Elastic Properties of Some Polycrystalline Transition-Metal Monocarbides. *J. Chem. Phys.* 45 (1966), 547–549. <https://doi.org/10.1063/1.1727602>.
- [32] M. Lee and R. S. Gilmore. Single crystal elastic constants of tungsten monocarbide. *J. Mater. Sci.* 17 (1982), 2657–2660. <https://doi.org/10.1007/BF00543901>.

- [33] J. Kim, Y. J. Suh, and I. Kang. First-principles calculations of the phase stability and the elastic and mechanical properties of η -phases in the WC-Co system. *J. Alloys Compd.* 656 (2016), 213–217. <https://doi.org/10.1016/j.jallcom.2015.09.214>.
- [34] P. Hones, N. Martin, M. Regula, and F. Lévy. Structural and mechanical properties of chromium nitride, molybdenum nitride, and tungsten nitride thin films. *J. Phys. D. Appl. Phys.* 36 (2003), 1023–1029. <https://doi.org/10.1088/0022-3727/36/8/313>.
- [35] N. M. Parreira, N. J. Carvalho, F. Vaz, and A. Cavaleiro. Mechanical evaluation of unbiased W-O-N coatings deposited by d.c. reactive magnetron sputtering. *Surf. Coatings Technol.* 200 (2006), 6511–6516. <https://doi.org/10.1016/j.surfcoat.2005.11.020>.
- [36] T. Polcar, N. M. Parreira, and A. Cavaleiro. Structural and tribological characterization of tungsten nitride coatings at elevated temperature. *Wear* 265 (2008), 319–326. <https://doi.org/10.1016/j.wear.2007.10.011>.
- [37] Y. D. Su, C. Q. Hu, C. Wang, M. Wen, and W. T. Zheng. Relatively low temperature synthesis of hexagonal tungsten carbide films by N doping and its effect on the preferred orientation, phase transition, and mechanical properties. *J. Vac. Sci. Technol. A* 27 (2009), 167–173. <https://doi.org/10.1116/1.3058721>.
- [38] Y. D. Su et al. Effects of bias voltage and annealing on the structure and mechanical properties of $WC_{0.75}N_{0.25}$ thin films. *J. Alloys Compd.* 486 (2009), 357–364. <https://doi.org/10.1016/j.jallcom.2009.06.147>.
- [39] L. von Fieandt, K. Johansson, T. Larsson, M. Boman, and E. Lindahl. On the growth, orientation and hardness of chemical vapor deposited Ti(C,N). *Thin Solid Films* 645 (2018), 19–26. <https://doi.org/10.1016/j.tsf.2017.10.037>.
- [40] L. Ortiz-Membrado et al. Measuring the fracture toughness of single WC grains of cemented carbides by means of microcantilever bending and micropillar splitting. *Int. J. Refract. Met. Hard Mater.* 98 (2021), 105529. <https://doi.org/10.1016/j.ijrmhm.2021.105529>.
- [41] N. Cuadrado, D. Casellas, L. Llanes, I. Gonzalez, and J. Caro. Effect of crystal anisotropy on the mechanical properties of WC embedded in WC-Co cemented carbides. *Proc. Euro Int. Powder Metall. Congr. Exhib. Euro PM 2011*. 2011, 215–220.
- [42] C. Maerky, M. O. Guillou, J. L. Henshall, and R. M. Hooper. Indentation hardness and fracture toughness in single crystal $TiC_{0.96}$. *Mater. Sci. Eng. A* 209 (1996), 329–336. [https://doi.org/10.1016/0921-5093\(95\)10152-7](https://doi.org/10.1016/0921-5093(95)10152-7).

- [43] R. Stylianou et al. Thermal crack formation in TiCN/ α -Al₂O₃ bilayer coatings grown by thermal CVD on WC-Co substrates with varied Co content. *Surf. Coatings Technol.* 392 (2020), 125687. <https://doi.org/10.1016/j.surfcoat.2020.125687>.
- [44] R. Stylianou et al. Stress relaxation through thermal crack formation in CVD TiCN coatings grown on WC-Co with different Co contents. *Int. J. Refract. Met. Hard Mater.* 86 (2020), 105102. <https://doi.org/10.1016/j.ijrmhm.2019.105102>.
- [45] J. García et al. In situ investigations on stress and microstructure evolution in polycrystalline Ti(C,N)/ α -Al₂O₃ CVD coatings under thermal cycling loads. *Crystals* 11 (2021), 1–18. <https://doi.org/10.3390/cryst11020158>.
- [46] I. El Azhari et al. Contact damage investigation of CVD carbonitride hard coatings deposited on cemented carbides. *Int. J. Refract. Met. Hard Mater.* 86 (2020), 105050. <https://doi.org/10.1016/j.ijrmhm.2019.105050>.
- [47] Thermal and Physical Properties of Pure Elemental Metals. *CRC Handb. Chem. Phys.* Ed. by J. R. Rumble. 103rd. Boca Raton, FL: CRC Press/Taylor & Francis.
- [48] H. Wang, T. Webb, and J. W. Bitler. Study of thermal expansion and thermal conductivity of cemented WC-Co composite. *Int. J. Refract. Met. Hard Mater.* 49 (2015), 170–177. <https://doi.org/10.1016/j.ijrmhm.2014.06.009>.
- [49] W. Huang. Thermodynamic Properties of the Nb-W-C-N System. *Zeitschrift für Met.* 88 (1997), 63–68.
- [50] S. Jonsson. Assessment of the Ti-W-C System and Calculations in the Ti-W-C-N System. *Zeitschrift für Met.* 87 (1996), 788–795.
- [51] A. H. Abdelhameed and W. Jacob. Deposition of thermally stable tungsten nitride thin films by reactive magnetron sputtering. *Surf. Coatings Technol.* 375 (2019), 701–707. <https://doi.org/10.1016/j.surfcoat.2019.07.046>.
- [52] B. Wicher et al. Chemical and structural characterization of tungsten nitride (WN_x) thin films synthesized via Gas Injection Magnetron Sputtering technique. *Vacuum* 165 (2019), 266–273. <https://doi.org/10.1016/j.vacuum.2019.04.020>.
- [53] H. T. Chiu and S. H. Chuang. Tungsten nitride thin films prepared by MOCVD. *J. Mater. Res.* 8 (1993), 1353–1360. <https://doi.org/10.1557/JMR.1993.1353>.

- [54] S. H. Mohamed. Thermal stability of tungsten nitride films deposited by reactive magnetron sputtering. *Surf. Coatings Technol.* 202 (2008), 2169–2175. <https://doi.org/10.1016/j.surfcoat.2007.09.005>.
- [55] S.-H. Kim et al. Characterization of Atomic Layer Deposited W_Nx_Cy Thin Film as a Diffusion Barrier for Copper Metallization. *J. Electrochem. Soc.* 151 (2004), 272–282. <https://doi.org/10.1149/1.1652054>.
- [56] H. M. Ajmera, T. J. Anderson, J. Koller, L. McElwee-White, and D. P. Norton. Deposition of W_Nx_Cy thin films for diffusion barrier application using the dimethylhydrazido (2-)tungsten complex $(CH_3CN)Cl_4W(NNMe_2)$. *Thin Solid Films* 517 (2009), 6038–6045.
- [57] X. X. Zhang et al. Thermal stability of tungsten sub-nitride thin film prepared by reactive magnetron sputtering. *J. Nucl. Mater.* 485 (2017), 1–7. <https://doi.org/10.1016/j.jnucmat.2016.12.009>.
- [58] H. Zhang et al. Microstructure and growth mechanism of tungsten carbide coatings by atmospheric CVD. *Surf. Coatings Technol.* 344 (2018), 85–92. <https://doi.org/10.1016/j.surfcoat.2018.03.011>.
- [59] D. Garg et al. Low-temperature CVD tungsten carbide coatings for wear/erosion resistance. *12th Annu. Conf. Compos. Adv. Ceram. Mater. Ceram. Eng. Sci. Proc.* John Wiley & Sons, Ltd, 1988, 1215–1222. <https://doi.org/10.1002/9780470310502.ch15>.
- [60] N. J. Archer and K. K. Yee. Chemical vapour deposited tungsten carbide wear-resistant coatings formed at low temperatures. *Wear* 48 (1978), 237–250. [https://doi.org/10.1016/0043-1648\(78\)90222-3](https://doi.org/10.1016/0043-1648(78)90222-3).
- [61] P. Gouy-Pailler and Y. Pauleau. Tungsten and tungsten-carbon thin films deposited by magnetron sputtering. *J. Vac. Sci. Technol. A Vacuum, Surfaces, Film.* 11 (1993), 96–102. <https://doi.org/10.1116/1.578725>.
- [62] T. Tavsanoğlu, C. Begum, M. Alkan, and O. Yücel. Deposition and characterization of tungsten carbide thin films by DC magnetron sputtering for wear-resistant applications. *JOM* 65 (2013), 562–566. <https://doi.org/10.1007/s11837-013-0571-x>.
- [63] P. K. Srivastava, T. V. Rao, V. D. Vankar, and K. L. Chopra. Synthesis of tungsten carbide films by rf magnetron sputtering. *J. Vac. Sci. Technol. A Vacuum, Surfaces, Film.* 2 (1984), 1261–1265. <https://doi.org/10.1116/1.572392>.

- [64] P. Tägtström, H. Högberg, U. Jansson, and J.-O. Carlsson. Low Pressure CVD of Tungsten Carbides. *Le J. Phys. IV* 5 (1995), 967–974. <https://doi.org/10.1051/jphyscol:19955114>.
- [65] J. M. Blocher. Structure/property/process relationships in chemical vapor deposition CVD. *J. Vac. Sci. Technol.* 11 (1974), 680–686. <https://doi.org/10.1116/1.1312735>.
- [66] K. A. Beadle, R. Gupta, A. Mathew, J. G. Chen, and B. G. Willis. Chemical vapor deposition of phase-rich WC thin films on silicon and carbon substrates. *Thin Solid Films* 516 (2008), 3847–3854. <https://doi.org/10.1016/j.tsf.2007.06.170>.
- [67] T. Nakajima and T. Shirasaki. Chemical Vapor Deposition of Tungsten Carbide, Molybdenum Carbide Nitride, and Molybdenum Nitride Films. *J. Electrochem. Soc.* 144 (1997), 2096–2100. <https://doi.org/10.1149/1.1837747>.
- [68] A. Osada, E. Nakamura, S. Tsuchiya, and A. Nishiyama. Chemical vapor deposition of tungsten carbide layer for cutting tool. *EURO CVD - 15 Fifteenth Eur. Conf. Chem. Vap. Depos.* Ed. by A. Devi, R. A. Fisher, H. Parala, M. D. Allendorf, and M. L. Hitchman. Vol. 09. Pennington, New Jersey: The Electrochemical Society, Inc., 2005, 1006–1013.
- [69] C. Hammond. The Basics of Crystallography and Diffraction. 4th. Oxford, UK: Oxford University Press, 2015. <https://doi.org/10.1093/acprof:oso/9780198738671.001.0001>.
- [70] P. Villars and K. Cenzual. *Pearson's Crystal Data - Crystal Structure Database for Inorganic Compounds, Release 2016/17*.
- [71] M. Birkholz. Thin Film Analysis by X-ray Scattering. Weinheim: Wiley-VCH Verlag GmbH & Co. KGaA, 2006.
- [72] Y. Leng. Materials characterization: Introduction to Microscopic and Spectroscopic Methods. 1st. Singapore, 2008.
- [73] D. B. Williams and C. B. Carter. Transmission Electron Microscopy. 2nd. New York, NY, USA: Springer Science+Business Media, 2009.
- [74] A. J. Schwartz, M. Kumar, B. L. Adams, and D. P. Field. Electron Backscatter Diffraction in Materials Science. Ed. by A. J. Schwartz, M. Kumar, B. L. Adams, and D. P. Field. 2nd Editio. New York, NY, USA: Springer Science+Business Media, 2009.
- [75] V. Moraes et al. Substoichiometry and tantalum dependent thermal stability of α -structured W-Ta-B thin films. *Scr. Mater.* 155 (2018), 5–10. <https://doi.org/10.1016/j.scriptamat.2018.06.005>.

- [76] G. Greczynski, D. Primetzhofer, J. Lu, and L. Hultman. Core-level spectra and binding energies of transition metal nitrides by non-destructive x-ray photoelectron spectroscopy through capping layers. *Appl. Surf. Sci.* 396 (2017), 347–358. <https://doi.org/10.1016/j.apsusc.2016.10.152>.
- [77] C. Adelman et al. Compositional depth profiling of TaCN thin films. *J. Vac. Sci. Technol. A Vacuum, Surfaces, Film.* 30 (2012), 041510. <https://doi.org/10.1116/1.4726261>.
- [78] M. Nastasi, J. W. Mayer, and Y. Wang. *Ion Beam Analysis: Fundamentals and Applications*. 1st. Boca Raton, FL: CRC Press/Taylor & Francis Group, 2015.
- [79] B. Bakht et al. Systematic compositional analysis of sputter-deposited boron-containing thin films. *J. Vac. Sci. Technol. A* 39 (2021), 063408. <https://doi.org/10.1116/6.0001234>.
- [80] *Potku software*, <https://www.jyu.fi/science/en/physics/research/infrastructures/accelerator-laboratory/pelletron/potku>. 2022.
- [81] G. Greczynski and L. Hultman. Towards reliable X-ray photoelectron spectroscopy: Sputter-damage effects in transition metal borides, carbides, nitrides, and oxides. *Appl. Surf. Sci.* 542 (2021), 148599. <https://doi.org/10.1016/j.apsusc.2020.148599>.
- [82] M. P. Seah. Summary of ISO/TC 201 standard: VII ISO 15472 : 2001 - surface chemical analysis - x-ray photoelectron spectrometers - calibration of energy scales. *Surf. Interface Anal.* 31 (2001), 721–723. <https://doi.org/10.1002/sia.1076>.
- [83] D. Céolin et al. Hard X-ray photoelectron spectroscopy on the GALAXIES beamline at the SOLEIL synchrotron. *J. Electron Spectros. Relat. Phenomena* 190 (2013), 188–192. <https://doi.org/10.1016/j.elspec.2013.01.006>.
- [84] J. P. Rueff et al. The GALAXIES beamline at the SOLEIL synchrotron: Inelastic X-ray scattering and photoelectron spectroscopy in the hard X-ray range. *J. Synchrotron Radiat.* 22 (2015), 175–179. <https://doi.org/10.1107/S160057751402102X>.
- [85] S. Tanuma, H. Shinotsuka, C. J. Powell, and D. R. Penn. Electron inelastic mean free paths in compounds. *J. Surf. Anal.* 26 (2019), 106–107. <https://doi.org/10.1384/jsa.26.106>.
- [86] W. C. Oliver and G. M. Pharr. An improved technique for determining hardness and elastic modulus using load and displacement sensing indentation experiments. *J. Mater. Res.* 7 (1992), 1564–1583. <https://doi.org/10.1557/JMR.1992.1564>.

- [87] D. S. Harding, W. C. Oliver, and G. M. Pharr. Cracking during nanoindentation and its use in the measurement of fracture toughness. *Mater. Res. Soc. Symp. - Proc.* Vol. 356. 1995, 663–668. <https://doi.org/10.1557/proc-356-663>.
- [88] M. T. Laugier. New formula for indentation toughness in ceramics. *J. Mater. Sci. Lett.* 6 (1987), 355–356. <https://doi.org/10.1007/BF01729352>.
- [89] N. Cuadrado, J. Seuba, D. Casellas, M. Anglada, and E. Jiménez-Piqué. Geometry of nanoindentation cube-corner cracks observed by FIB tomography: Implication for fracture resistance estimation. *J. Eur. Ceram. Soc.* 35 (2015), 2949–2955. <https://doi.org/10.1016/j.jeurceramsoc.2015.03.031>.
- [90] M. Bartosik, H. J. Böhm, C. Krywka, Z. L. Zhang, and P. H. Mayrhofer. Influence of phase transformation on the damage tolerance of Ti-Al-N coatings. *Vacuum* 155 (2018), 153–157. <https://doi.org/10.1016/j.vacuum.2018.06.001>.
- [91] N. Cuadrado, D. Casellas, M. Anglada, and E. Jiménez-Piqué. Evaluation of fracture toughness of small volumes by means of cube-corner nanoindentation. *Scr. Mater.* 66 (2012), 670–673. <https://doi.org/10.1016/j.scriptamat.2012.01.033>.
- [92] M. Zawischa, S. Makowski, N. Schwarzer, and V. Weihnacht. Scratch resistance of superhard carbon coatings — A new approach to failure and adhesion evaluation. *Surf. Coatings Technol.* 308 (2016), 341–348. <https://doi.org/10.1016/j.surfcoat.2016.07.109>.
- [93] S. J. Bull and E. G. Berasetegui. An overview of the potential of quantitative coating adhesion measurement by scratch testing. *Tribol. Int.* 39 (2006), 99–114. <https://doi.org/10.1016/j.triboint.2005.04.013>.
- [94] M. Fallqvist, R. M'Saoubi, J. M. Andersson, and M. Olsson. Mechanical and tribological properties of PVD-coated cemented carbide as evaluated by a new multipass scratch-testing method. *Adv. Tribol.* 2012 (2012). <https://doi.org/10.1155/2012/305209>.
- [95] A. J. Gant and M. G. Gee. A review of micro-scale abrasion testing. *J. Phys. D. Appl. Phys.* 44 (2011), 073001. <https://doi.org/10.1088/0022-3727/44/7/073001>.
- [96] J.-O. Andersson, T. Helander, L. Höglund, P. Shi, and B. Sundman. THERMO-CALC & DICTRA, Computational Tools For Materials Science. *Calphad* 26 (2002), 273–312. [https://doi.org/10.1016/S0364-5916\(02\)00037-8](https://doi.org/10.1016/S0364-5916(02)00037-8).
- [97] A. E. van Arkel. Kristalbouw en physische eigenschappen. *Physica (The Hague)* 4 (1924), 286–301.

- [98] M. S. Lucas et al. Magnetic and vibrational properties of high-entropy alloys. *J. Appl. Phys.* 109 (2011), 1–3. <https://doi.org/10.1063/1.3538936>.
- [99] F. Laves and H. J. Wallbaum. Die Kristallstruktur von Ni_3Ti und Si_2Ti (zwei neue Typen). *Z. Kristallographie* 101 (1939), 78–93. <https://doi.org/10.1524/zkri.1939.101.1.78>.
- [100] J. Wagner et al. The effect of deposition temperature on microstructure and properties of thermal CVD TiN coatings. *Int. J. Refract. Met. Hard Mater.* 26 (2008), 120–126. <https://doi.org/10.1016/j.ijrmhm.2007.01.010>.
- [101] H. E. Cheng and M. H. Hon. Growth mechanism of star-shaped TiN crystals. *J. Cryst. Growth* 142 (1994), 117–123.
- [102] H. E. Cheng and M. H. Hon. Texture formation in titanium nitride films prepared by chemical vapor deposition. *J. Appl. Phys.* 79 (1996), 8047–8053. <https://doi.org/10.1063/1.362358>.
- [103] A. G. Metcalfe. The Mutual Solid Solubility of Tungsten Carbide and Titanium Carbide. *J. Inst. Metals* 73 (1947), 591–607. <https://ci.nii.ac.jp/naid/10024350793/en/>.
- [104] P. Ettmayer and R. Suchentrunk. Über die thermische Stabilität der Eta-Carbide. *Monatshefte für Chemie* 101 (1970), 1098–1103. <https://doi.org/10.1007/BF00908553>.
- [105] A. Hull. The crystal structure of ferro-magnetic metals. *Phys. Rev* 14 (1919), 540–541.
- [106] R. V. Sara. Phase Equilibria in the System Tungsten—Carbon. *Journal of the American Ceramic Society* 48 (1965), 251–257. <https://doi.org/10.1111/j.1151-2916.1965.tb14731.x>.
- [107] J. R. Creighton. The surface chemistry and kinetics of tungsten chemical vapor deposition and selectivity loss. *Thin Solid Films* 241 (1994), 310–317. [https://doi.org/10.1016/0040-6090\(94\)90448-0](https://doi.org/10.1016/0040-6090(94)90448-0).
- [108] C. Bisch, M. Nadal, F. Teyssandier, M. Bancel, and B. Vallon. Chemical vapour deposition of titanium carbide on WC-Co cemented carbides. *Mater. Sci. Eng.* 202 (1995), 238–248. [https://doi.org/10.1016/0921-5093\(95\)09812-7](https://doi.org/10.1016/0921-5093(95)09812-7).
- [109] K. A. Pearlstine and C. M. Friend. Alteration in Surface Reaction Selectivity of Nitriles. 1. HCN on W(100) and W(100)-(5x1)-C. *J. Phys. Chem.* 90 (1986), 4341–4343. <https://doi.org/10.1021/j100409a024>.
- [110] K. A. Pearlstine and C. M. Friend. Alteration in Surface Reaction Selectivity on Nitriles. 2. CH_3CN on W(100) and W(100)-(5x1)-C. *J. Phys. Chem.* 90 (1986), 4344–4347. <https://doi.org/10.1021/j100409a025>.

- [111] C. M. Friend and J. G. Serafin. Bonding and reactivity of acetonitrile on W(100)-(5x1)-C. *J. Chem. Phys.* 88 (1988), 4037–4045. <https://doi.org/10.1063/1.453857>.
- [112] A. Westgren and G. Phragmén. Röntgenanalyse der Systeme Wolfram-Kohlenstoff und Molybdän-Kohlenstoff. *Z. Anorg. Allg. Chem.* 156 (1926), 27–36.
- [113] A. Larsson and S. Rупpi. Microstructure and properties of Ti(C,N) coatings produced by moderate temperature chemical vapour deposition. *Thin Solid Films* 402 (2002), 203–210. [https://doi.org/10.1016/S0040-6090\(01\)01712-6](https://doi.org/10.1016/S0040-6090(01)01712-6).
- [114] L. von Fieandt, T. Larsson, M. Boman, and E. Lindahl. Texture formation in chemical vapor deposition of Ti(C,N). *J. Cryst. Growth* 508 (2019), 90–95. <https://doi.org/10.1016/j.jcrysgro.2018.12.030>.
- [115] J. G. Hulkko et al. Kinetics of the low-pressure chemical vapor deposited tungsten nitride process using tungsten hexafluoride and ammonia precursors. *J. Vac. Sci. Technol. A* 39 (2021), 063403. <https://doi.org/10.1116/6.0001093>.
- [116] Y. Yang, S. Jayaraman, D. Y. Kim, G. S. Girolami, and J. R. Abelson. Crystalline texture in hafnium diboride thin films grown by chemical vapor deposition. *J. Cryst. Growth* 294 (2006), 389–395.
- [117] T. Takahashi and H. Kamiya. Chemical vapor deposition of titanium diboride. *J. Cryst. Growth* 26 (1974), 203–209. [https://doi.org/10.1016/0022-0248\(74\)90247-4](https://doi.org/10.1016/0022-0248(74)90247-4).
- [118] D. Javdošňák et al. Tribological properties and oxidation resistance of tungsten and tungsten nitride films at temperatures up to 500 °C. *Tribol. Int.* 132 (2019), 211–220. <https://doi.org/10.1016/j.triboint.2018.12.019>.
- [119] M. Wen et al. Growth, stress and hardness of reactively sputtered tungsten nitride thin films. *Surf. Coatings Technol.* 205 (2010), 1953–1961.
- [120] J. Hommet, C. Fuchs, E. Fogarassy, F. Le Normand, and T. Szörényi. XPS study of pulsed laser deposited CN_x films. *Phys. Rev. B - Condens. Matter Mater. Phys.* 64 (2001), 235416. <https://doi.org/10.1103/PhysRevB.64.235416>.
- [121] F. Frank, M. Tkadletz, C. Czettl, and N. Schalk. Microstructure and mechanical properties of ZrN, Zr(C,N) and ZrC coatings grown by chemical vapor deposition. *Coatings* 11 (2021), 1–13. <https://doi.org/10.3390/coatings11050491>.

- [122] M. Bartosik, C. Rumeau, R. Hahn, Z. L. Zhang, and P. H. Mayrhofer. Fracture toughness and structural evolution in the TiAlN system upon annealing. *Sci. Rep.* 7 (2017), 1–9. <https://doi.org/10.1038/s41598-017-16751-1>.
- [123] C. Kainz et al. Influence of bias voltage on microstructure, mechanical properties and thermal stability of arc evaporated $\text{Cr}_{0.74}\text{Ta}_{0.26}\text{N}$ coatings. *Surf. Coatings Technol.* 417 (2021), 127212. <https://doi.org/10.1016/j.surfcoat.2021.127212>.

Acta Universitatis Upsaliensis

*Digital Comprehensive Summaries of Uppsala Dissertations
from the Faculty of Science and Technology 2208*

Editor: The Dean of the Faculty of Science and Technology

A doctoral dissertation from the Faculty of Science and Technology, Uppsala University, is usually a summary of a number of papers. A few copies of the complete dissertation are kept at major Swedish research libraries, while the summary alone is distributed internationally through the series Digital Comprehensive Summaries of Uppsala Dissertations from the Faculty of Science and Technology. (Prior to January, 2005, the series was published under the title "Comprehensive Summaries of Uppsala Dissertations from the Faculty of Science and Technology".)



ACTA
UNIVERSITATIS
UPSALIENSIS
UPPSALA
2022

Distribution: publications.uu.se
urn:nbn:se:uu:diva-487198